Changing the cross-sectional geometry of a bow tunnel thruster

Effects on the performance of the thruster at slow forward motion using Computational Fluid Dynamics

Tobias Schaap

Master Thesis

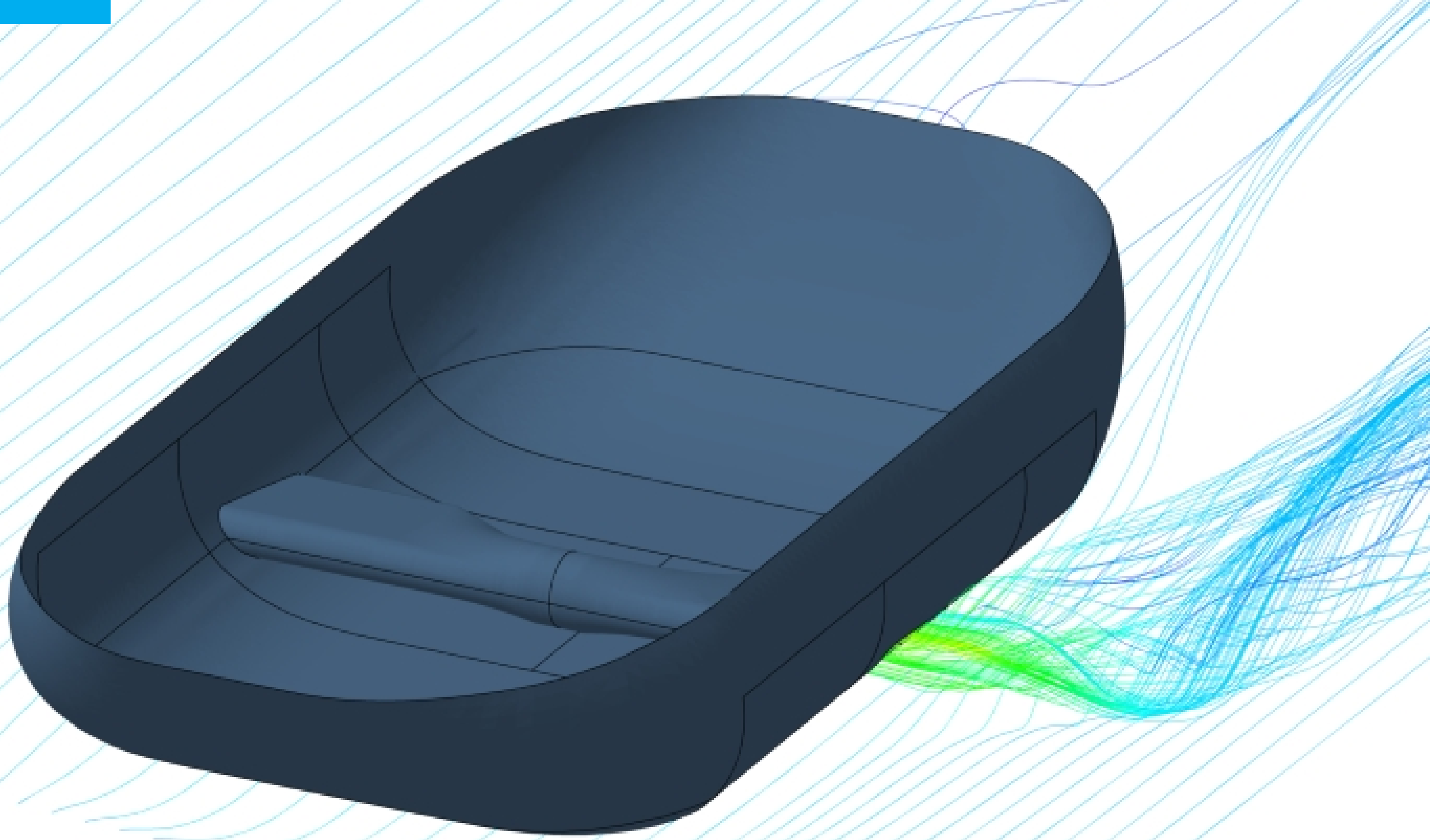

TU Delft Delft University of Technology

Challenge the future

Changing the cross-sectional geometry of a bow tunnel thruster

Effects on the performance of the thruster at slow forward motion using Computational Fluid Dynamics

Master Thesis

by

Tobias Schaap

in partial fulfillment of the requirements for the degree of

Master of Science
in Marine Technology - Track Science - Specialization Ship Hydromechanics (MT-SC-SH)

at the Delft University of Technology, Faculty of Mechanical, Maritime and Materials Engineering
to be defended publicly on Wednesday December 16, 2015 at 1:00 PM.

Student number:	4089561	
Supervisor:	Prof. dr. ir. T. J. C. van Terwisga	TU Delft
Thesis committee:	Prof. dr. ir. R. H. M. Huijsmans	TU Delft
	Dr. ir. M. J. B. M. Pourquie	TU Delft
	Ing. A. de Jager	IHC Holland B.V.
	Ir. A. B. Kruijswijk	IHC Holland B.V.

Abstract

In this master thesis the flow behavior and the performance of a bow tunnel thruster at slow forward vessel motion is studied using Computational Fluid Dynamics (CFD). The study analyzes the flow and the turning ability for a cylindrical cross-section and the effect of changing the cross-section of the bow tunnel thruster.

At Royal IHC it is noticed that trailing suction hopper dredgers experience a significant decrease in turning ability, using the bow tunnel thrusters, when trailing at a speed through the water of 5 [kts] in comparison to zero forward speed. Dredgers are often operating at those speeds, use the bow tunnel thruster to keep course and therefore often experience this effect in practice.

To study the flow behavior the commercial CFD solver Numeca FineMarine is used. Computations are made on model scale using a simplified wedge model of a container ship (Nienhuis wedge) for validation purpose and of a trailing suction hopper dredger (Hopper wedge). For the Nienhuis wedge multiple numerical studies are performed that focus on the used set-up, non-linear iterations and convergence, time step, actuator disk modeling and first layer thickness. A grid study together with a verification and validation study close the analysis of the Nienhuis wedge. The settings from the Nienhuis wedge are used for the computations with the Hopper wedge. For the Hopper wedge a systematic tunnel cross-section variation is derived and three different shapes are computed at different ship speeds: a circular cross-section (S1010A), flattened cross-section (S0610A) and a streamlined cross-section (S0602A).

The flow of the tunnel jet and the flow around the ship are comparable to the flow of a jet in a cross-flow. The flow is unsteady and fluctuates. Once the tunnel jet flow leaves the tunnel the flow interacts with the surrounding flow and is bend into the direction of that surrounding flow. A large wake region is visible behind the jet. The velocity ratio m between the ship speed and the tunnel jet speed is an important factor and characterizes the behavior of the flow. At m=0.2 [-] a strong jet shows only little interaction with the ship flow, while a weak jet at m=0.4 [-] is largely influenced by the ship flow.

For the Nienhuis wedge a grid study shows large numerical uncertainties. The verification and validation study shows that the computations are qualitative valid and quantitative invalid. Quantitative comparison between two different model tests shows discrepancy in the obtained side force on the wedge. However the quantitative results of this study do agree with a full scale CFD study. In both this CFD study and the full scale CFD study the hub and strut of the thruster are not modeled. It is expected that this has an effect on the side force and is a possible reason for the difference between CFD and model tests.

A change in cross-section reduces the wake region behind the jet for the streamlined cross-section (S0602A) in comparison to the other cross-section. The absolute side force of the streamlined cross-section (S0602A) is significantly increased (more than 30 [%] at m=0.4 [-]), while the resistance is slightly increased (4 [%]) in comparison to the circular cross-section (S1010A) and the flattened cross-section (S0610A). The aim is an increase in absolute side force as it increases the turning ability of the ship, an increase in resistance however is negative on the fuel-consumption of the vessel.

In general the cross-sectional variation shows promising results, however the numerical uncertainties of the computations are too high. It is advised to check the CFD model scale results with CFD full scale computations and to validate both with measurements. For a future CFD study it is advised to model the hub and strut of the bow thruster, because they can have an influence on the side force on the wedge.

Preface

This document is the result of the last part of my study in Maritime Technology at the Delft University of Technology. I got the chance to write my master thesis at Royal IHC in Kinderdijk. Together with IHC I developed the plan to use computational fluid dynamics to study bow tunnel thrusters of a dredger at slow forward motion.

I would like to thank Royal IHC for the opportunity, their believe in me and the pleasant working environment. Not everyone can say that he wrote his master thesis surrounded by an UNESCO world heritage such as the windmills in Kinderdijk. First of all I would like to thank Alex Kruiswijk. Alex toughed me the in and outs of Numeca FineMarine and was during the complete time my first point of contact. I'm very thankful for the many nice discussions, feedback and time with him. I would also like to thank Arie de Jager who supported me on all hydrodynamic aspects of my study and gave me many valuable insights from the practice. Next to that I would like to thank my direct colleagues at IHC: Rick, Bram, Ron, Remy, Erik and Leonard. You all contributed to a nice working environment and provided me with a lot of good discussions and coffee.

At the university I was supported by my professor Tom van Terwisga. Tom was involved from the beginning and gave me many advises, both about the thesis and for my future career. I would also like to thank Rene Huijsmans and Mathieu Pourquie for their contribution to my thesis and for the interesting discussions during the progress meetings.

I would like to thank Royal IHC and Topsector Water who granted me a scholarship for my master at the Delft University of Technology. I'm very grateful for their thrust in me and the financial support.

During my study I got the chance to meet a lot of important and inspiring people for me. I think each and everyone of them contributed to the great time I had during my study in Delft. I would like to thank especially Reinier, Max and Martijn who became very close friends, read my report over and over and are always there for me. Also thanks to Floor, John, Johannes and Daniela who read my thesis many times and provided me with valuable feedback.

Last but not least I would like to thank Verena. You give me the strength and power to be who I am. Thank you for all your patience, your feedback and your love.

Contents

Nomenclature

Latin Letters

A	Area of a cross-section	[m^2]
B	Beam of the wedge	[m]
C	Courant number $C = \frac{\Delta t u}{\Delta x}$	[-]
C_B	Block coefficient of the straight section of the wedge	[-]
C_F	Force coefficient normalized with Thrust $C_F = \frac{F_y(u_s,T)-F_y(u_s,0)}{T}$	[-]
$C_{F-Nienhuis}$	Force coefficient defined by Nienhuis [1] $C_{F-Nienhuis} = \frac{F_T(u_s,T)-F_T(u_s,0)-T}{T}$	[-]
Co	Cell Courant number $Co = \frac{\Delta t u_i}{\Delta x_i}$	[-]
C_p	Normalized pressure $C_p = \frac{2p}{\rho_w u_s^2}$	[-]
C_X	Force coefficient normalized with Bernoulli $C_X = \frac{2F_y}{\rho_w v_j^2 A}$	[-]
D	Diameter / Tunnel diameter of a circular cross-section	[m]
D_H	Hydraulic diameter $D_H = \frac{4A}{P}$	[m]
D_{ref}	Tunnel diameter of the circular cross-section	[m]
D_L	Diameter of the left semicircle	[m]
D_R	Diameter of the right semicircle	[m]
F	Force	[N]
Fn	Froude number $Fn = \frac{u}{\sqrt{gL}}$	[-]
F_S	Safety factor	[-]
F_T	Total force on the wedge in the y-direction during model tests	[N]
g	Gravity intensity	[m/s^2]
h	Typical cell size	[m]
J	Advance number of the propeller $J = \frac{v_a}{nD}$	[-]
K	Turbulent kinetic energy	[m^2/s^2]
K_Q	Propeller torque coefficient $K_Q = \frac{Q}{\rho n^2 D^5}$	[-]
K_T	Propeller thrust coefficient $K_T = \frac{T}{\rho n^2 D^4}$	[-]
L	Length scale/ Length overall of the wedge	[m]
$L_{overall}$	Length of the straight section of the wedge	[m]
L_{ref}	Reference length	[m]
L_{LR}	Distance between left and right semicircle	[m]
n	Number of refinement	[-]
n	Rate of revolution of the propeller	[1/s]
$\vec{n}$	Unit vector	[-]
N	Number of steps considered	[-]
N_{cells}	Number of grid cells	[-]
n_g	Number of grids	[-]
n_{nl}	Number of non-linear iterations	[-]
m	Velocity ratio $m = u_s/v_j$	[-]
p	Pressure scale/ Hydrodynamic pressure	[Pa]
p	Order of accuracy	[-]
P	Perimeter	[m]
Q	Propeller torque	[Nm]
r	Position on the radial axis	[m]
r	Grid refinement ratio	[-]
R	Radius of the actuator disk	[m]
R	Residual	

Re	Reynolds number $Re = \frac{uL}{\nu}$	[-]
r_{AA}	Ratio between left semicircle and reference diameter $r_{AA} = \frac{D_L}{D_{ref}}$	[-]
r_{BB}	Ratio between right semicircle and left semicircle $r_{AA} = \frac{D_R}{D_L}$	[-]
S	Surface of interest	
t	Time	[s]
t_{step}	Time step	[-]
T	Thrust	[N]
T_w	Draft of the wedge	[m]
u	Velocity scale / velocity in the x-direction	[m/s]
U	95 [%] uncertainty	
u_{ref}	Reference velocity	[m/s]
u_s	Wedge velocity	[m/s]
v	Velocity in the y-direction	[m/s]
$\vec{v}$	Velocity vector	[m/s]
V	Volume	[m^3]
v_a	Advance velocity	[m/s]
v_{rel}	Normalized velocity in the xy-plane $v_{rel} = \frac{\sqrt{u^2+v^2}}{u_s}$	[-]
v_j	Tunnel jet velocity	[m/s]
v_T	Tunnel jet velocity ratio $v_T = \frac{v_j(u_s)}{v_j(0)}$	[-]
w	velocity in the z-direction	[m/s]
x	Position on the x-axis	[m]
y	Position on the y-axis	[m]
$y+$	Dimensionless wall distance	[-]
y_{wall}	Width of the first cell	[m]
z	Position on the z-axis	[m]
z_{ref}	Tunnel center location above keel	[m]
z_s	Distance to the symmetry plane above keel	[m]

Greek Letters

α	Coefficient of a power series expansion	
Δ	Change of a quantity	
Δt	Time step	[s]
Δx	Mean cell size $\Delta x = \left(\frac{V}{N_{cells}}\right)^{\frac{1}{3}}$	[m]
ϵ	Error	
μ	Mean	
μ	Dynamic viscosity	[N s/m^3]
ν	Kinematic viscosity	[m^2]
ρ	Density	[kg/m^3]
ω	Specific turbulent dissipation rate	[1/s]
ϕ	Value of a quantity	
σ	Standard deviation	
τ	Surface stress	

Subscripts

a	Air
$axial$	Axial contribution
D	Experiment
gi	Guess value at cell i
i	Cell/Grid
$initial$	Initial cell
$round$	Round-off error/ value
$iteration$	Iteration error/ value
o	Estimate of the truth
S	Simulation
SI	Input error/value of a simulation
SM	Modeling error/value of a simulation
SN	Numerical error/value of a simulation
T	Truth
$tangential$	Tangential contribution
$total$	Total
w	Water
x	X-direction
y	Y-direction
z	Z-direction

1
Introduction

A vessel keeps its speed using propellers and its heading using rudders. Trailing suction hopper dredgers, Figure 1.1, operate often in shallow water, where they have an increased course-keeping capabilities compared to open water. However, during berthing, the ability to maneuver becomes more important. Here, the bow thruster finds it use, providing extra thrust used for manoeuvring. When a vessel however has forward speed and the bow tunnel thruster is used the effect of the thruster is decreased. Dredging vessels often use a bow tunnel thruster at slow forward speed, during dredging in shallow water and encounter the negative effect regularly.

Figure 1.1: The trailing hopper suction dredger Vox Maxima. Picture adapted from: [2].

The aim of this study is to investigate if a change in cross-sectional geometry of the bow tunnel has a positive effect on the performance of the bow tunnel thruster at low forward speed.

1.1. Background

The vessel is moving at relative low forward speeds along a straight line during dredging. In general hopper dredgers have one suction tube on one side of the vessel which is close to or even on the seabed. The suction tube is the main contributor to the resistance of the dredger while dredging. The suction tube and the propellers of the dredger are not situated at the same distance from midship, which results in moments mostly yaw and surge that turn the ship. The course is constantly corrected by using the rudder(s) of the ship to avoid turning. If only the rudder(s) are used for the correction of the heading the vessel will drift through the water. The crew tries to avoid drifting sideways by using the bow tunnel thrusters in the front of the ship, compare Figure 1.2.

A dredger normally dredges at 2 [kts] forward speed. In rivers and other coastal areas the current can reach speeds of up to 5 [kts], which means that the dredger experiences velocities through the water of 4 to 7 [kts] during dredging. Sea trails where the effect of the bow thruster is tested have shown that for ship speeds through the water of 5 [kts] the ship does not turn when the bow thruster operates. These

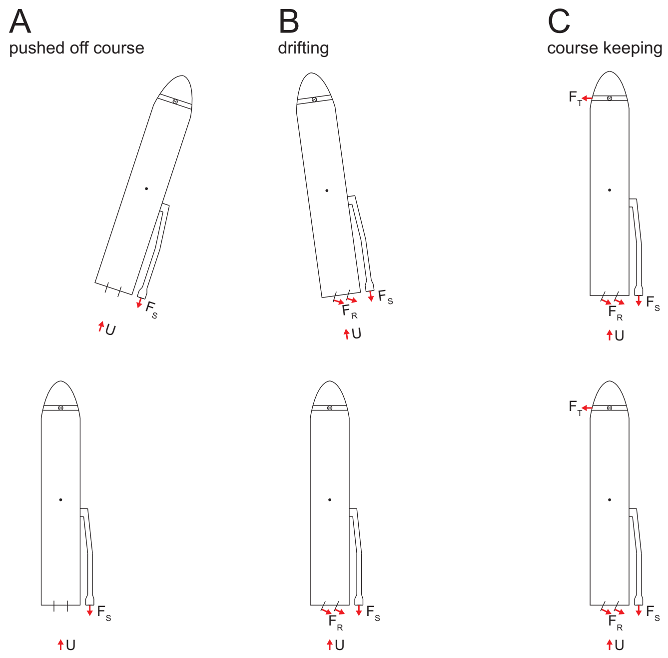

Figure 1.2: Forces acting on a hopper dredger while dredging. Case A: only the suction tube is used, which results in turning. Case B: the rudders are used to keep course, which results in drifting. Case C: also the bow thruster tunnels are used, which results in course keeping.

results were obtained for all trailing suction hopper dredgers of Royal IHC. Based on this the research question for this study is developed.

1.2. Research question and hypothesis

The main research question of this thesis is:

> *Can the design of the bow tunnel thruster of a trailing suction hopper dredger be changed in order to improve the ability to turn the ship at slow forward motion?*

Two questions were analyzed during a literature study [3] to answer the research question:

- What are the characteristics of the flow in and around of a bow thruster tunnel at slow forward speed?
- Which factors influence the performance of a bow thruster?

Based on the literature study [3] it is chosen to focus on one influencing factor: cross-section of the tunnel. In a paper by Karlikov & Sholomovich [4] a large increase of side force was reported for a streamlined cross-section in comparison to a circular cross-section. The knowledge of the effect of the cross-section of the tunnel on the performance of bow tunnel thruster is limited and a streamlined cross-section can be implemented in a simple and cost-efficient way in current trailing suction hopper dredger designs. From this the hypothesis is formulated:

> *A streamlined bow tunnel thruster cross-section increases the transverse force by 20 [%] compared to a circular cross-section with the same cross-sectional area at 5 knots forward speed for a trailing suction hopper dredger, based on CFD.*

This hypothesis is based on the following:

- The CFD code of Numeca FineMarine can be used for this type of computations
- Verification and validation studies are performed and give a positive outcome
- The results, of the CFD analysis are in accordance with literature in a qualitative and quantitative matter

- The amount of transversal force increase is based on a paper of Karlikov & Sholomovich [4].
- A systematic variation of the cross-section is used to find a better solution
- A simplified hull form of the ships hull geometry can be used to analyze the aforementioned effects
- A forward speed of 5 [kts] is representative for the phenomena

The overall objective of this thesis is to check the hypothesis and answer the research question.

1.3. Scope of this document

The purpose of this document is to present the background, analysis and results of the aforementioned study which was performed by the author during a nine-month master thesis project at Royal IHC in Kinderdijk the Netherlands for a degree in Maritime Technology at the Delft University of Technology. The master thesis consists of two main phases: definition study phase and master thesis phase. During the definition study phase a definition study [3] is written, which aims to give an answer on the research question, based on literature, a plan of approach and a road-map for the master thesis phase. The results of the master thesis phase are presented in this document.

The presented calculations are made for model scale. The wedge geometries are based on a container ship cross-section (Nienhuis wedge) and a trailing suction hopper wedge cross-section (Hopper wedge) at the bow thruster tunnel frame. These wedges are a simplification of the complete ship geometry and have constant cross-sections, a tunnel thruster and an artifical bow and stern. All results are compared against each other and for the Nienhuis wedge a validation case is selected.

The theoretical background presented in this document has the purpose to describe the main principles and theories applied in CFD. For additional theoretical background the reader is referred to one of the many textbooks on this topic; e.g two very good ones are [5] and [6].

During this study only computations with the commercial computational fluid dynamics (CFD) software Numeca FineMarine are performed. This document discusses recommended settings for the computation and may not be applicable for other structures. Furthermore, conclusions of the systematic variation of tunnel cross-sections are purely based on the presented computations.

1.4. Relevance of the work

A decrease in bow thruster performance and slow forward speeds has been studied by many authors. Different studies analyzed the effect of different influencing factors. Most of these studies are based on model testing. In public literature not many computational fluid dynamic (CFD) results exist on the matter, besides Nienhuis [1] and non-public CFD reports such as [7]. Next to that most of the studies are performed between 1950 and 1990, with different hull forms. Since then the hull shapes have evolved. This underlines the need for more research in this area. Recently a joint industry project lead by MARIN started on this topic, which shows a need for this specific research in the industry.

The hypothesis of this study is based on a paper by Karlikov and Sholomovich [4] who reported a significant increase in bow thruster tunnel performance by changing the cross-section of the bow thruster tunnel. The study is based on model test results of one container vessel model. The goal of this thesis is to contribute to the knowledge of the effect of a streamlined tunnel cross-section on the performance of a bow tunnel thruster.

1.5. Structure of this document

The structure of this document is as follows: First in Chapter 2 the theoretical background of computational fluid dynamics, turbulence modeling and error classification is given. In Chapter 3 computational fluid dynamics studies are presented in order to find good computation settings. These studies are made with the Nienhuis wedge for one ship velocity and thrust combination. This is followed by a verification and validation study and a variation of the thrust and ship velocities. A hopper wedge is designed in Chapter 4 and is first compared with the results of the Nienhuis wedge. After the comparison a systematic cross-section variation of the bow thruster tunnel is presented. In Chapter 5 the conclusion and recommendations of the study can be found. The thesis contains multiple appendices which give the reader additional information on selected topics.

2

Theoretical background

In this chapter the theoretical background of computational fluid dynamics (CFD), including turbulence modeling and error classification is discussed. A literature study on the performance of bow thruster in slow forward speed is presented in the Definition Study [3]. This chapter is limited to the main concepts of the used commercial CFD package Numeca FineMarine, however most of these concepts are universally applied in CFD software.

2.1. Concept of computational fluid dynamics

In this section the concept of computational fluid dynamics (CFD) is described in multiple phases. In this study Reynolds averaged Navier stokes (RANS) is used, which is a common used type of CFD. A schematic overview of these phases is shown in Figure 2.1. CFD is used to get an approximation of the real physics involved in a problem. While the governing equations of CFD were already derived by Claude-Louis Navier and George Gabriel Stokes in the 1840s it took until the 1960s until the Navier-Stokes equation were solved numerically with the help of computers [8]. Since then computers have evolved and yield to more reliable CFD computations. However the computations can only give an approximation of the solution of the Navier-Stokes equations and until an exact solution is found CFD is the best possibility to approximate a solution of the Navier-Stokes equations.

The concept of CFD is presented based on the books of Ferziger and Peric [5], Versteeg and Malalasekera [6] and on a presentation by Numeca [9].

The first phase is to analyze the problem, making some assumptions to find a suitable physical model. One decision is for example whether the fluid is compressible or in-compressible. In this study the following assumptions are made and therefore the corresponding physical models are used [10]:

- Incompressiblity (density is constant)
- isotherm (temperature is constant)
- viscous flow (viscosity is taken into account)
- unsteady flow (time dependent)
- Reynolds-averaged Navier Stokes equations (RANS) (time averaged equations of motion)
- turbulent flow (turbulence is modeled)
- subsonic flow (velocities under consideration are far below the speed of sound)

These physical models are translated into mathematical models, by applying the fundamental laws of mechanics to a fluid. The result is two conservation laws. The conservation of mass is defined as:

$$\frac{\partial \rho}{\partial t} + \nabla \cdot (\rho \vec{v}) = 0 \tag{2.1}$$

The second one is the conservation of momentum, defined as:

$$\rho \frac{\partial \vec{v}}{\partial t} + \rho \left(\vec{v} \cdot \nabla \right) \vec{v} = -\nabla p + \rho \vec{g} + \nabla \cdot \tau_{ij} \tag{2.2}$$

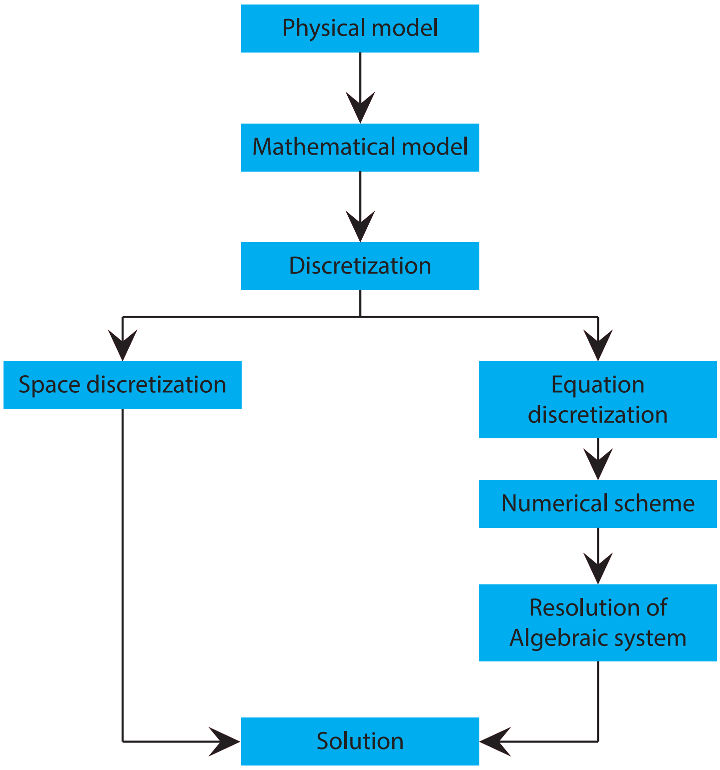

Figure 2.1: Components of a CFD model. Based on [9].

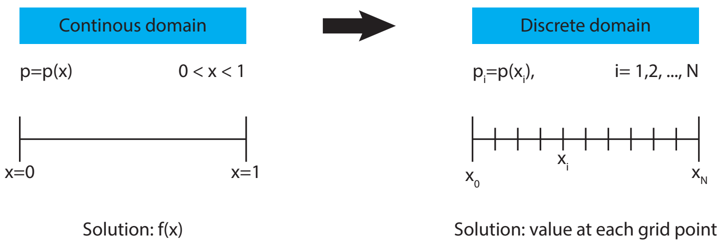

Figure 2.2: Simple 1D example to illustrate the conversion from continuous to a discrete problem. Based on [9].

As the conservation laws cannot be solved directly, the solution is approximated by a discretization, transforming the problem from the continuous domain to a discrete domain. Figure 2.2 shows a small 1D example of that process. While in the continuous domain the value of p is known for all locations of x, in the discrete domain the value is approximated at each grid point x_i. There is no information available what the approximated value of p is between two grid points. The discretization is done separately for the space discretization and the equations, compare Figure 2.1.

During the space discretization the space is transformed into a discrete distribution of points. This distribution is called mesh or grid and is obtained by using advanced meshing tools, algorithm that create structured or unstructured grids. On the one hand a finer grid gives more insight in the flow, but it takes more cells to create it and the computational costs are related to the amount of cells used. On the other hand a coarse grid may skip important flow information, simply as no grid point is defined at the point of interest. The standard approach is to use grid refinement at the regions of interest and much coarser cells far away from the structure. It is important to define suitable boundary conditions on the side of the domain, so a numerical solution can be found. Wrong boundary conditions normally give a solution, but have no physical meaning.

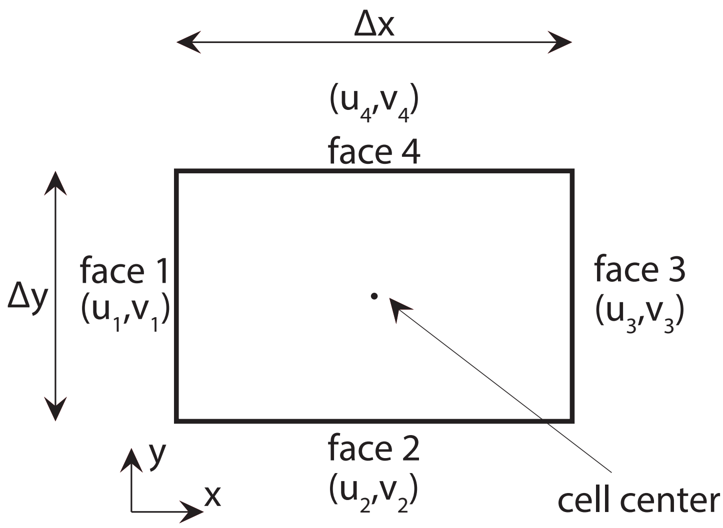

Figure 2.3: Sign convention for a 2D regular cell. The norms are defined pointing outward. Based on [9].

The equation discretization converts the Navier-Stokes equations into discrete equations that can be applied at a grid node. Imagine a 2D regular cell as defined in Figure 2.3 and take the continuity equation for a steady in-compressible flow:

$$\int_S \vec{v} \cdot \vec{n} \; dS = 0 \tag{2.3}$$

The continuity equation means that the net volume flow into the control volume is zero. Using the sign definitions shown in Figure 2.3 and using the finite volume approach the continuity equation becomes:

$$-u_1 \Delta y - v_2 \Delta x + u_3 \Delta y + v_4 \Delta x = 0 \tag{2.4}$$

With the values for the velocities at the cell faces and the geometry of the cell the continuity equation can be solved straightforward. All mathematical equations are converted to discretized equation in a similar way. The three most used methods are finite volume, finite difference and finite element.

Many of the discretized equations are (non)linear differential equations. To calculate derivatives and integrals non-linear numerical schemes are developed that approximate them. First an example is given for a linear differential algebraic equation:

$$\frac{du}{dx} + u = 0 \qquad 0 \le x \le 1 \qquad u(0) = 1 \tag{2.5}$$

The discretized equation becomes:

$$u_i + \left(\frac{du}{dx}\right)_i = 0 \tag{2.6}$$

For the approximation of the derivative a first order Taylor expansion (first order Euler forward) is chosen:

$$\left(\frac{du}{dx}\right)_i = \frac{u_i - u_{i-1}}{\Delta x} + O\left(\Delta x\right)^2 \tag{2.7}$$

Where $O\left(\Delta x\right)^2$ is the truncation error that is proportional to Δx^2; all terms higher than the first order are neglected. Therefore this approximation is 1st order accurate. The order of the numerical scheme is therefore a measure for its accuracy. After rearranging the example becomes:

$$-u_{i-1} + (1 + \Delta x)\, u_i = 0 \tag{2.8}$$

The choice of the numerical scheme is affecting three important factors: numerical stability, accuracy and convergence. In general a higher-order method is more stable and has better convergence, while increasing the computational cost. Therefore in most commercial codes, including Numeca FineMarine, 2nd-order numerical schemes are used as a compromise [5].

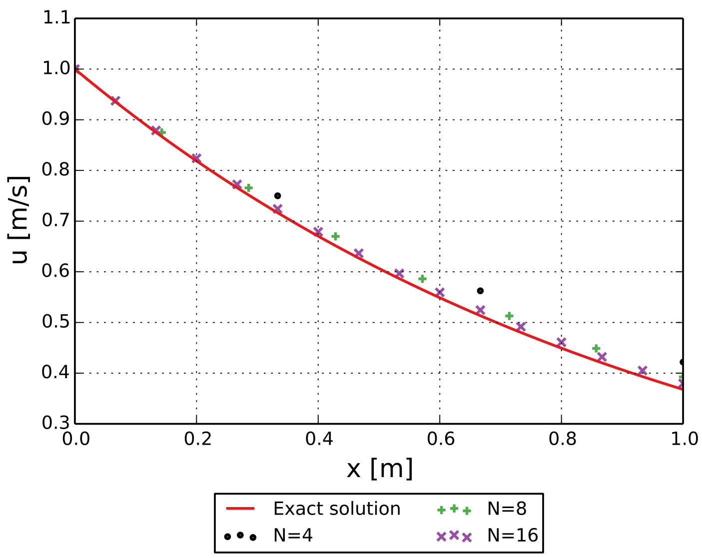

Figure 2.4: The example calculated for 4,8 and 16 grid points together with the exact solution $u(x) = e^{-x}$.

The solution of Equation 2.8 can now be approximated for a different amount of grid points. In Figure 2.4 the linear system is solved for 4, 8 and 16 grid points together with the exact solution. It can be seen, that an increasing number of grid points result in a smaller difference to the exact solution. In this example with a first order scheme the discretization error is proportional to Δx, for a second order method proportional to Δx^2. Which means that if Δx is reduced by factor 2, the discretization error is reduced by factor 4. When a grid refinement gives a difference within a defined tolerance, grid convergence is reached.

As most of the equations are non-linear equations an additional level of complexity is added in order to solve them. A common approach is to use the guess value method, which uses a guess value of a quantity based on previous information. This method is explained in the following non-linear differential equation method [9]:

$$\frac{du}{dx} + u^2 = 0 \qquad 0 \leq x \leq 1 \qquad u(0) = 1 \tag{2.9}$$

Discretized the equation becomes:

$$\frac{u_i - u_{i-1}}{\Delta x} + u_i^2 = 0 \tag{2.10}$$

As this equation cannot be solved linearly a guess value u_{gi} is introduced:

$$\Delta u_i = u_i - u_{gi} \tag{2.11}$$

Taking the square, neglecting Δu_i^2 and rearranging results in:

$$u_i^2 \approx u_{gi}^2 + 2u_{gi}\left(u_i - u_{gi}\right) \tag{2.12}$$

The discretized equations can then be substituted with:

$$\frac{u_i - u_{i-1}}{\Delta x} + 2u_{gi}ui - u_{gi}^2 = 0 \tag{2.13}$$

The value of u_{gi} is now guessed and iterations are made until the difference between the guess value of u_{gi} and the velocity u_i are converged. As a measure of convergence a residual is defined, which is a measure of the difference between the guess value and the 'real' value and is defined either by using the L2 or the Linf norm. Using the L2 norm the residual is defined as:

$$R_{L2} = \sqrt{\frac{\sum_{i=1}^{N}\left(u_i - u_{gi}\right)^2}{N}} \tag{2.14}$$

Using the Linf norm the residual becomes

$$R_{Linf} = max\left(\left|u_i - u_{gi}\right|\right) \tag{2.15}$$

The residuals are calculated for all important quantities of the computation. If the residual decreases to an acceptable level, the computation is converged. Figure 2.5 shows the algorithm Numeca FineMarine uses to compute a solution. After a solution is found, the solution can be made visible with the help of the generated grid and the solution of each grid point, as shown in Figure 2.1.

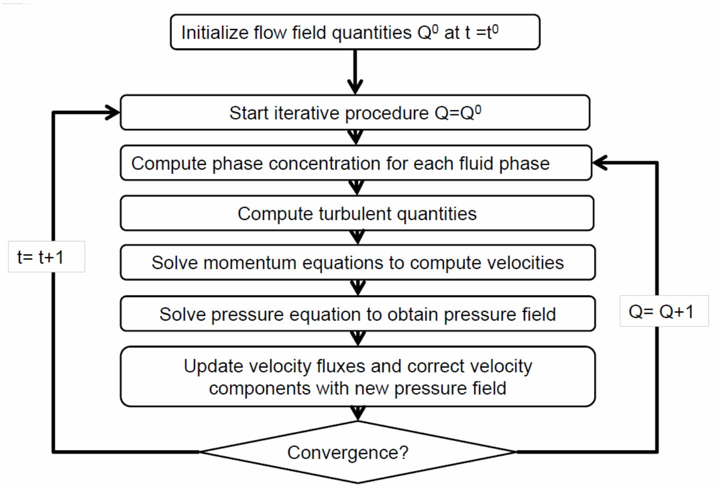

Figure 2.5: A schematic overview of the algorithm used by Numeca. Adapted from [9].

2.2. Turbulence modeling

Turbulence is chaotic and random in motion and changes continuously in time [6]. This behavior causes fluctuations on a wide range of time and length scales. A big issue of CFD is how to deal with turbulence. In fluid dynamics above a certain Reynolds number Re a flow becomes turbulent, below that point the flow is laminar. The Reynold number is defined as:

$$Re = \frac{UL}{\nu} \tag{2.16}$$

Where U and L are characteristic velocity and length scales and ν is the kinematic viscosity. The difference in length scale between the smallest (L_{min}) and largest (L_{max}) eddy is based on experiments related to the Reynolds number by [11]:

$$\frac{L_{max}}{L_{min}} = Re^{\frac{3}{4}} \tag{2.17}$$

For Re=1.6E9 [-], a typical Reynold number for full scale ships the relation between the smallest and largest eddy is 8E6 [-]. This means if the largest eddy length scale is about 100 [m] the smallest eddy scale is 0.0125 [mm]. To cover all this length scales very small cell sizes need to be used. In practice three approaches to deal with turbulence are available:

- Direct numerical simulation (DNS)
- Large eddy simulation (LES)
- Renolds-Averaged Navier Stokes (RANS)

As DES and LES are too expensive for commercial and practical engineering cases, RANS is the most used method. At the moment LES and DES are primarly used in fundamental conceptual research, but it is expected that they become more important as the computerpower will further evolve. In the following a description on the concept of RANS is given together with the different types of turbulence models for RANS. The discussion is based on Versteeg and Malalasekera [6], the ISIS-CFD manual [10] and Collie et al. [11].

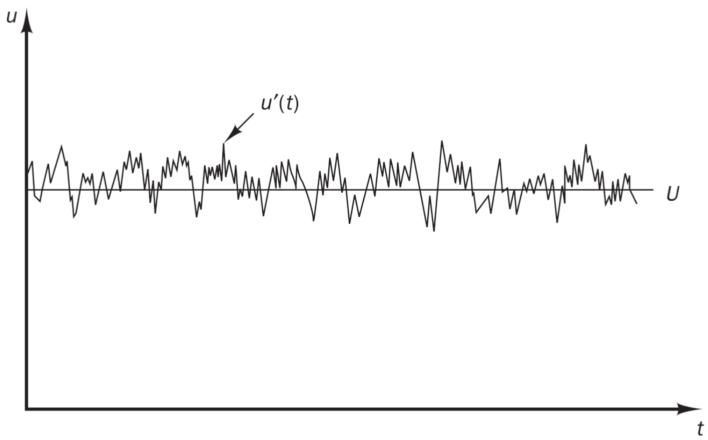

Figure 2.6: Typical measurement of the point velocity in turbulent flow. Adapted from [6].

A typical point measurement in turbulent flow is shown in Figure 2.6. The velocity $u(t)$ is decomposed in a steady mean value U and a fluctuating component $u'(t)$. The so called Reynolds decomposition is therefore defined by mean values of the flow and statistical properties of the corresponding fluctuation:

$$u(t) = U + u'(t) \tag{2.18}$$

When introducing this decomposition to the Navier stokes equation one gets the Reynolds-averaged Navier Stokes equations [11]:

$$\frac{\partial u_i}{\partial x_i} = 0 \tag{2.19}$$

$$U_j \frac{\partial U_i}{\partial x_j} = -\frac{1}{\rho}\frac{\partial P}{\partial x_i} + \frac{\partial}{\partial x_j}\left(\nu \frac{\partial U_i}{\partial x_j} - \overline{u_i' u_j'}\right) \tag{2.20}$$

Where U and P are the mean values of the velocity and pressure respectively, u' the fluctuating component of the velocity, ρ the density and ν the kinematic viscosity of the fluid. The product of the fluctuating quantities $\overline{u_i' u_j'}$ is unknown and therefore a method to find this unknown correlation is needed. Two types of models exist: the 2nd-order closure models and the eddy viscosity models. Where the former solves modeled differential equation for the Reynold stresses and the latter approximate the Reynold stresses as a function of eddy viscosity v_t and the mean stress tensor S_{ij}.

The eddy viscosity models are most commonly approximated with the Boussinesq equation, which assumes that the the Reynold stresses are proportional to the mean stresses:

$$\tau_{ij} = \nu_t S_{ij} \quad \text{with} \quad S_{ij} = \frac{1}{2}\left(\frac{\partial U_i}{\partial x_j} + \frac{\partial U_j}{\partial x_i}\right) \tag{2.21}$$

It should be noticed that due to this definition the eddy viscosity varies throughout the flow domain. The different eddy viscosity models can be grouped into three types:

- Zero-equation models (algebraic)
- One-equation models
- Two-equation models

where for the zero-equation model an algebraic description of the eddy viscosity is used and the other two types use one or respectively two extra transport equation to determine the eddy viscosity.

In FineMarine multiple eddy viscosity models are available, for this study the common used shear-stress transport Menter k-ω (SST Menter k-ω) model is used. This is a mixed approach that makes use of the Wilcox k-ω model near solid walls and the standard k-ϵ model near boundary layer edges and in free-stream layers. The equations of the used SST Menter k-ω model are included in Appendix A.

2.3. Error classification

The theoretical background of CFD and turbulence modeling indicates that a simulation consist of many uncertainties and errors. In this study the definition of Roache [12] for error and uncertainty is used. An error is the difference between the true/exact value and a given solution and has a sign. Which means a true/exact value needs to be known in order to determine the error. Uncertainty on the other hand is an error band for the numerical result, where the true/exact solution is expected to be within this error band. The error band is defined in this study with a 95 [%] confidence interval. An uncertainty has therefore no sign.

In general the difference between a simulation result ϕ_S and the truth ϕ_T is decomposed in three types of errors: modeling error ϵ_{SM}, input error ϵ_{SI} and numerical error ϵ_{SN} [13]:

$$\epsilon_S = \phi_S - \phi_T = \epsilon_{SM} + \epsilon_{SI} + \epsilon_{SN} \tag{2.22}$$

For experimental data, on the other hand, the difference between the experimental result ϕ_D and the truth ϕ_T is defined as the experimental error ϵ_D [13]:

$$\epsilon_D = \phi_D - \phi_T \tag{2.23}$$

The resulting error ϵ is then defined as the difference between the simulation and experimental result as:

$$\epsilon = \phi_S - \phi_D \tag{2.24}$$

With this definition the corresponding validation uncertainty u_{val} ,assuming that the uncertainties are independent, is defined as [13]:

$$u_{val}^2 = u_{SN}^2 + u_{SI}^2 + u_D^2 \tag{2.25}$$

The error ϵ together with the validation uncertainty form an interval in which by definition the model error ϵ_{SM} falls [13]:

$$\epsilon_{SM} \in [\epsilon - u_{val}, \epsilon + u_{val}] \tag{2.26}$$

Based on the values for the error ϵ and the validation uncertainty u_{val} two cases can occur [14]:

- If $|\epsilon| > u_{val}$ the comparison error is probably dominated by the modeling error. Which gives an indication that the model needs to be improved.
- If $|\epsilon| < u_{val}$ the comparison error is within the noise level imposed by the three uncertainties. For a small value of ϵ this means that the solution is validated with u_{val} accuracy. Otherwise it means that the results of the experiment or numerical simulation need to be improved.

In the following subsections the numerical, input and experimental errors are explained in more detail. Next to that it is explained how these errors are taken into account during this study.

2.3.1. Numerical error

The numerical error of a simulation is commonly divided in three types of errors: round-off error, iteration error and discretization error. The numerical error is therefore defined as:

$$\epsilon_{SN} = \epsilon_{round} + \epsilon_{iteration} + \epsilon_{\phi} \tag{2.27}$$

In the following a small explanation on how to determine these numerical errors is given.

Round-off error

The round-off error is the error that is introduced by the rounding of values by the computer. The round-off error is direct consequence of the finite precision of a computer. As the precision of a computer is very high, the round-off error is negligible compared to the other errors. In this study a double precision with 15 digit is used. The round-off error is therefore neglected in this study.

Iteration error

The iteration error results from the non-linear iteration used to numerically solve the mathematical equations. In this study a convergence criteria of 2 orders is used. To calculate this convergence criteria the residual is defined using the infinite norm as [15]:

$$R = max(|R_i|) \tag{2.28}$$

Where R_i is the residual in cell i. The development of the decrease in residual (gain) is defined as the ratio between the initial residual R_i and the final residual R_f as:

$$Gain = \frac{R_i}{R_f} \tag{2.29}$$

The order of convergence is then defined as:

$$Order = log(Gain) \tag{2.30}$$

Or in other words the convergence criteria of 2 orders ensures that the gain in residual is at least 100 [-].

The iteration error is assumed to be minimized significantly compared to the discretization error and therefore the iteration error is neglected. However to ensure that the iteration error is fully neglectable it should be decreased to the finite precision of the computer. This is not practical in many engineering situations and not done in this study. This can lead to underestimation or incorrectly ignoring of the iteration error [16].

Discretization error

To access the discretization error with grid refinement studies a power series expansion is commonly used. The discretization error ϵ_ϕ of a variable ϕ is represented using a power series expansion as [16, Eq. 1]:

$$\epsilon_\phi \simeq \delta_{RE} = \phi_i - \phi_o = \alpha h_i^p \tag{2.31}$$

where ϕ_i is the flow quantity of grid i, ϕ_o is the estimate of the exact solution, α is an unknown constant, h_i stands for the typical cell size of grid i and p is the observed order of accuracy. The typical cell size h_i is defined as [16, Eq. 4]

$$h_i = \left(\frac{1}{N_i}\right)^{\frac{1}{n}} \tag{2.32}$$

Where N_i is the number of cells and n is the geometric dimension of the computation domain i.e. $n = 3$ for 3D.

The usage of a power series needs to fulfill two assumptions: the data are obtained in a sufficient refined grid to guarantee that the first term is dominant (solution in the asymptotic range) and the grid refinement ratio is constant for the complete computation. According to Eça and Hoekstra [17] the two assumptions are rarely met for practical CFD problems. Due to unstructured grids it is nearly impossible to maintain a constant grid refinement ratio, causing a lack of geometric similarity of grids is the main contributor to noisy data.

For practical problems three additional error estimators can be derived, assuming that the code is second-order accurate [17, Eq. 5,6,7]:

$$\epsilon_\phi \simeq \delta_1 = \phi_i - \phi_o = \alpha h_i \tag{2.33}$$

$$\epsilon_\phi \simeq \delta_2 = \phi_i - \phi_o = \alpha h_i^2 \tag{2.34}$$

$$\epsilon_\phi \simeq \delta_{12} = \phi_i - \phi_o = \alpha_1 h_i + \alpha_2 h_i^2 \tag{2.35}$$

The additional estimators of Eça and Hoekstra [17] are only used if Equation 2.31 is impossible to solve or if the results are not reliable. In the following the method is described shortly. In Appendix B the method is described in full detail. It should be noticed that the method proposed by Eça and Hoekstra [17] is an extension of the well-known grid convergence index (GCI) by Roache [12].

The proposed method needs at least 4 number of grids ($n_g \geq 4$), and includes a weighted approach. The error estimates in Equation 2.31, 2.33, 2.34, 2.35 are compared using least squares in order to determine the best ϕ_o. As a weighted approach is used every equation is calculated twice, once with every grid contributing the same and once weighted, were the finer mesh values have more weight on the outcome compared to a coarser mesh. The least square regression yields to estimations of the discretization error ϵ_ϕ, the standard deviation of the best fit σ and in some cases the order of grid convergence p. To estimate the uncertainty U_ϕ with a 95 [%] confidence interval a data range parameter is defined to distinguish between "good" and "bad" error estimations [17, Eq. 19]:

$$\Delta_\phi = \frac{(\phi_i)_{max} - (\phi_i)_{min}}{n_g - 1} \tag{2.36}$$

If the solution is monotonically convergent ($0.5 \leq p < 2.1$) and $\sigma < \Delta_\phi$, the error estimation is considered reliable and a safety factor of $F_S = 1.25$ [-] is chosen. If the solution doesn't fulfill the requirement a safety factor of $F_s = 3.0$ [-] is chosen (Compare [12] and [17]). The uncertainty U_ϕ is then defined as [17, Eq. 20, 21]:

$$U_\phi(\phi_i) = \begin{cases} F_S \epsilon_\phi(\phi_i) + \sigma + |\phi_i - \phi_{fit}| & \text{for } \sigma < \Delta_\phi \\ 3\frac{\sigma}{\Delta_\phi}\left(\epsilon_\phi(\phi_i) + \sigma + |\phi_i - \phi_{fit}|\right) & \text{for } \sigma \geq \Delta_\phi \end{cases} \tag{2.37}$$

2.3.2. Input error

The input error is a measure for the error introduced by the chosen settings and inputs. For example a constant value for the fluid properties is used during the CFD calculations. These values have by definition also a certain uncertainty and result in an error. For a general discussion and the determining of input errors the guidelines of ASME [13] are recommended. It is known that they are some input errors in the simulation by definition. These errors are caused by a lack of information in the Nienhuis reference case. The missing input values have been chosen with care. As the values used during the test are not known it is hard to quantify the error. In this study the input error is neglected and therefore u_{SI} is taken as zero.

2.3.3. Experimental error

For the validation study some model scale experiments are used. The uncertainties of the experiments is not reported. It is however known that all measurements have a certain error and therefore uncertainties in the results. In general two types of error exist: systematic and random errors. A systematic error is normally introduced by the measuring set-up. For example a load cell is not well calibrated. Random error are unknown and unpredictable an can change between different test runs. The random error can be deceased by running the same test run multiple times. As the uncertainties from model tests are not known it is assumed that all measured values have an uncertainty of 1.5 [%]. This is a typical order of magnitude for model tests, compare [14].

3

Computational fluid dynamics study of the Nienhuis wedge

Computational fluid dynamics computations for the Nienhuis wedge are performed to validate the computations with model test results of Nienhuis [1]. First the Nienhuis wedge is described in full detail together with the modeling, meshing and computational set-up of the computations. A base case is chosen to analyze the problem in-depth and to verify the basic settings for a speed and thrust variation. For all computations used in this study the following applies:

- model scale
- unstructured grid
- unsteady computation
- SST Menter k-ω turbulence model

3.1. Axis definition

The general axis definition used in this study is as follows. The positive x-direction points towards the stern with it's origin at the forward most point of the bow, the positive y-direction is defined from midship towards portside. The positive z-direction is pointing upwards with it's origin at the keel of the ship. Next to the general definition a local, bow tunnel based, coordinate system is used. The origin for that local coordinate system is at the most forward point of the tunnel in x-direction, at midship in the y-direction and the centerline of the tunnel in z-direction. The origin is therefore at (1.475,0,0.152) [m] for the Nienhuis wedge and at (1.475,0,0.1096) [m] for the Hopper wedge. Figure 3.1 shows the axis definition. The velocities are denoted u for the x-direction, v for the y-direction and w for the z-direction.

3.2. Modeling, meshing and set-up of the computations

In this section the Nienhuis wedge is developed and is fully described. After that the meshing and the numerical model of the Nienhuis wedge are discussed.

3.2.1. Modeling of the geometry

The geometry of the Nienhuis wedge can be seen in Figure 3.2a and the thruster geometry in Figure 3.2b. In the model tests the thruster is placed inside the tunnel. The tunnel has a circular cross-section and has a diameter D_{ref} of 0.15 [m]. Nienhuis measures the force on the model in all three directions and the thrust and torque of the thruster. Nienhuis derived the wedge geometry from the frame of a container ship. He took the frame at the position of the bow thruster tunnel and extended it to 10 tunnel diameters in length, 5 D_{ref} forward and 5 D_{ref} aft of that frame. The thruster is placed in the middle of the tunnel. The main particulars of the original geometry can be found in Table 3.1.

The frame of the used CFD model was created based on data points that were extracted from the original drawings of Nienhuis using a point extraction algorithm [18]. The resulting frame can be seen in Figure 3.3.

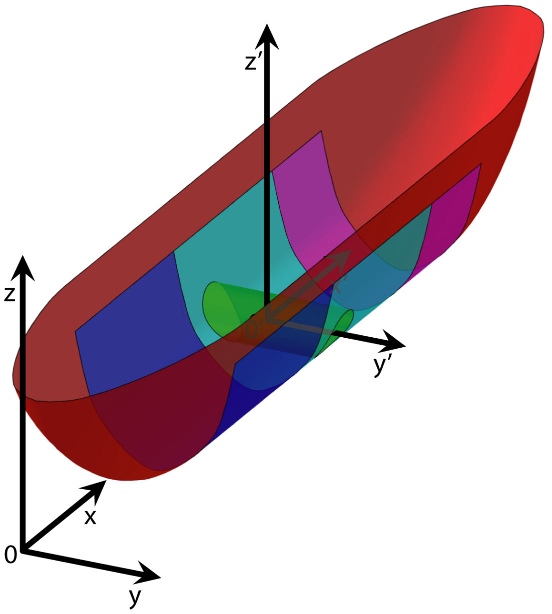

Figure 3.1: Axis definition.

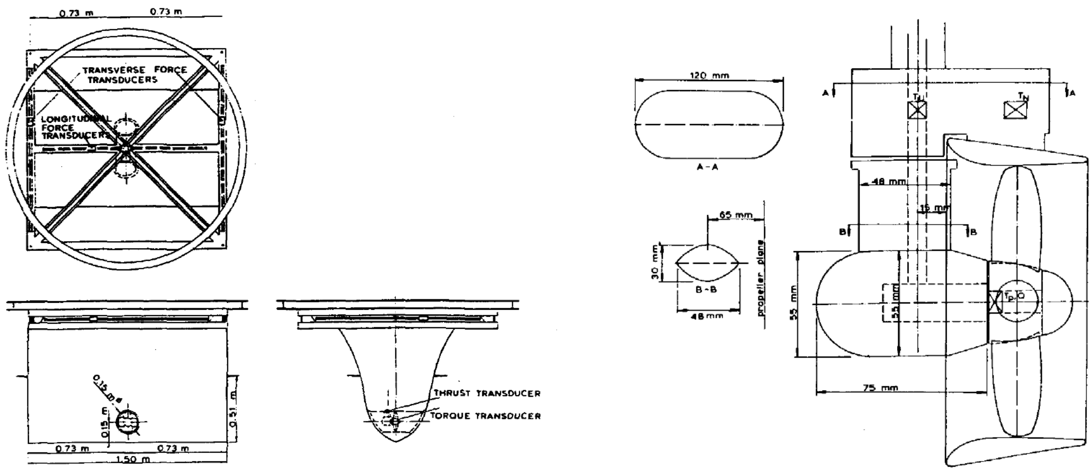

(a) Wedge geometry

(b) Thruster geometry

Figure 3.2: Technical drawings of the original wedge and thruster model used by Nienhuis. Adapted from [1].

Table 3.1: Main particulars of the Nienhuis wedge as reported by Nienhuis [1] and as used in this study.

Particular	Symbol	Unit	Model [1, Tab. A.5]	CFD model
Length straight section	$L_{original}$	[m]	1.5	1.5
Length overall	L	[m]	1.5	3.1
Beam	B	[m]	0.546	0.546
Draft	T	[m]	0.508	0.508
Block coefficient straight section	C_B	[-]	0.715	0.715
Tunnel diameter	D_{ref}	[m]	0.15	0.15
Tunnel center z location	z_{ref}	[m]	0.152	0.152

The geometric difference between the original drawings of Nienhuis and the CFD model is less than 0.01 [%] and therefore insignificant. Calculations with a 3D representation of the Nienhuis wedge as shown in Figure 3.4a resulted in numerical instabilities due to the flat "bow" and "stern". To allow more stable numerical simulations an artificial "bow" is made with a length of 0.8 [m]. It is created based on linear scaling of the frame. The artificial "bow" is added to the front and back of the wedge and extending it's length overall to 3.1 [m]. A 3D rendering of the CFD model as used in the validation study is shown in Figure 3.4b.

3.2.2. Meshing

For the meshing Numeca Hexpress is used. The 3D model was constructed in Rhinoceros and has been exported as para-solid. The para-solid is used as starting point for the mesh procedure. For all meshes a python script has been written, to control the behavior of the mesh, to change only a single parameter of the mesh settings and to reproduce meshes if needed. Hexpress produces an unstructured grid, by dividing an initial grid into multiple smaller cells. This refinement can be controlled and is applied to all surfaces on the body and to refinement boxes. In Appendix C the mesh settings of all used meshes are summarized and an example Python file for the creation of the meshed using Hexpress is given.

Based on a small preliminary study it was chosen to use a large domain, approximate three times larger than the recommended domain size for vessels by Numeca. Smaller domains seem to have problems of convergence for very low Froude number. At a domain size a factor three higher than usual the convergence became significant better. The tunnel thruster is simulated by an actuator disk. The actuator disk delivers a constant thrust and is explained in the Definition Study [3] in more detail.

In the beginning four set-up's are considered:

- Set-up 1 is the wedge modeled with a free-surface, to represent the waterline (z=0.508 [m])
- Set-up 2 is the same domain as set-up 1, but without a free-surface
- Set-up 3 uses the double body approach. A symmetry plane is used at the vertical position of the deck (z=0.804 [m])
- Set-up 4 uses the double body approach with a symmetry plane at the location of the waterline (z=0.508 [m])

For all four set-up's the same refinements are used to allow comparability. The intention of the analysis of four different set-up's is to analyze the effect of a free-surface and find the best set-up at acceptable computation effort.

The domain is 15 L in length direction (x-axis), 9 L in the width direction (y-axis) and 9 L in the height (z-axis) (for set-up 1 and 2) and 6L in height (for set-up 3 and 4). The bow of the model is placed at coordinate (0,0,0), the model is at model scale and the length dimensions are in [m]. The wedge is moving in the negative x-direction when moving forward. A positive thrust is applied in the positive y-direction. In Figure 3.5 the domain of set-up 2 is shown. In Figure 3.6 a comparison of the four set-up's in the yz-plane is shown, only the height of the domain is different. Table 3.2 presents the dimensions of the domains for the four set-up's.

Table 3.2: Domain used for the Nienhuis wedge, the values refer to the geometric origin where the forward most point of the geometry is located. The location of the lower and upper boundaries are presented in terms of the length of the wedge L and the location of the symmetry plane z_s (for set-up 3 and 4).

		lower boundary		upper boundary	
	set-up	[-]	[m]	[-]	[m]
x-direction	1,2,3,4	-3 L	-9.30	12 L	37.20
y-direction	1,2,3,4	-4.5 L	-13.95	4.5 L	13.95
z-direction	1,2	-4.5 L	-13.95	4.5 L	13.95
z-direction	3	z_s-6 L	-17.758	z_s	0.842
z-direction	4	z_s-6 L	-18.092	z_s	0.508

The geometry of the wedge is split in six different surfaces. The surfaces are refined to better capture the flow behavior. The terminology used for the six surfaces is defined in Figure 3.7. Next to the surfaces,

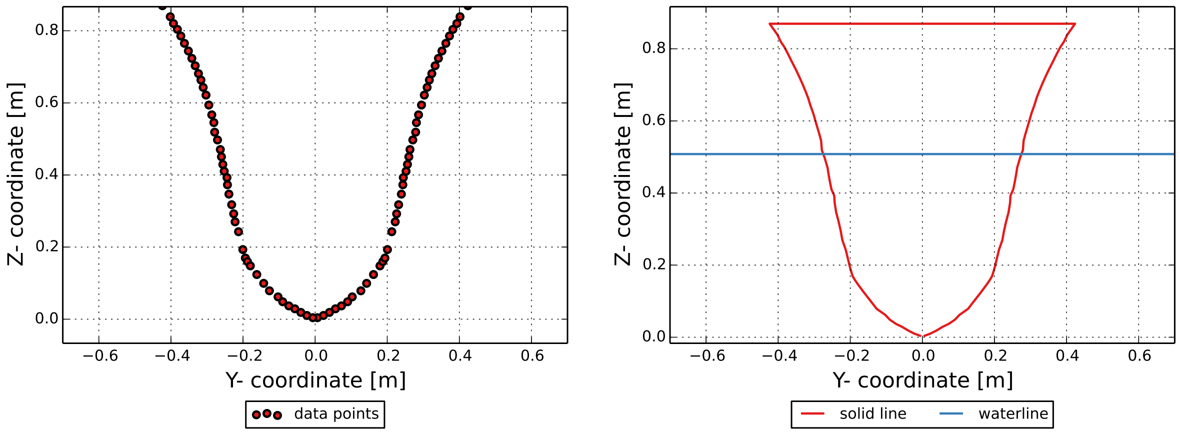

(a) Data points

(b) Solid line

Figure 3.3: Frame of the CFD model of the Nienhuis wedge. The data points and the resulting frame using solid lines.

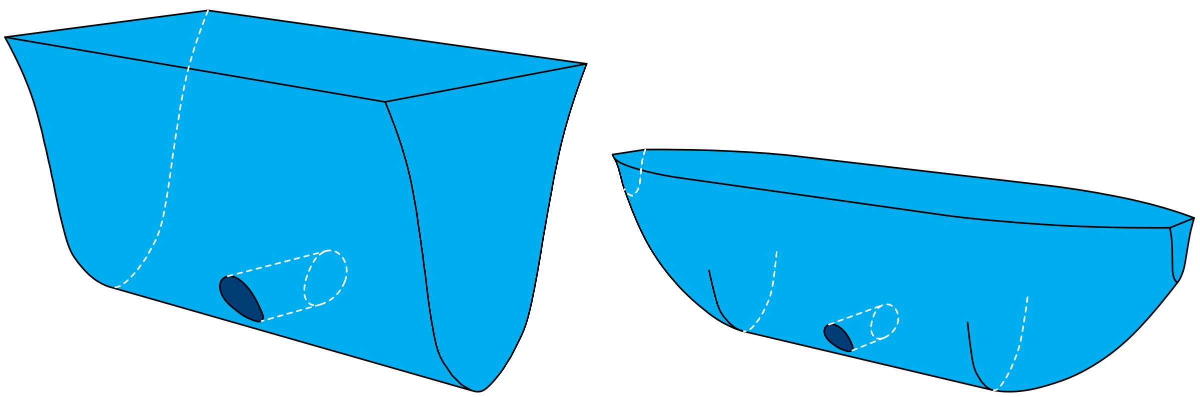

(a) original

(b) modified

Figure 3.4: 3D rendering of the CFD model of the Nienhuis wedge of the original and the modified model.

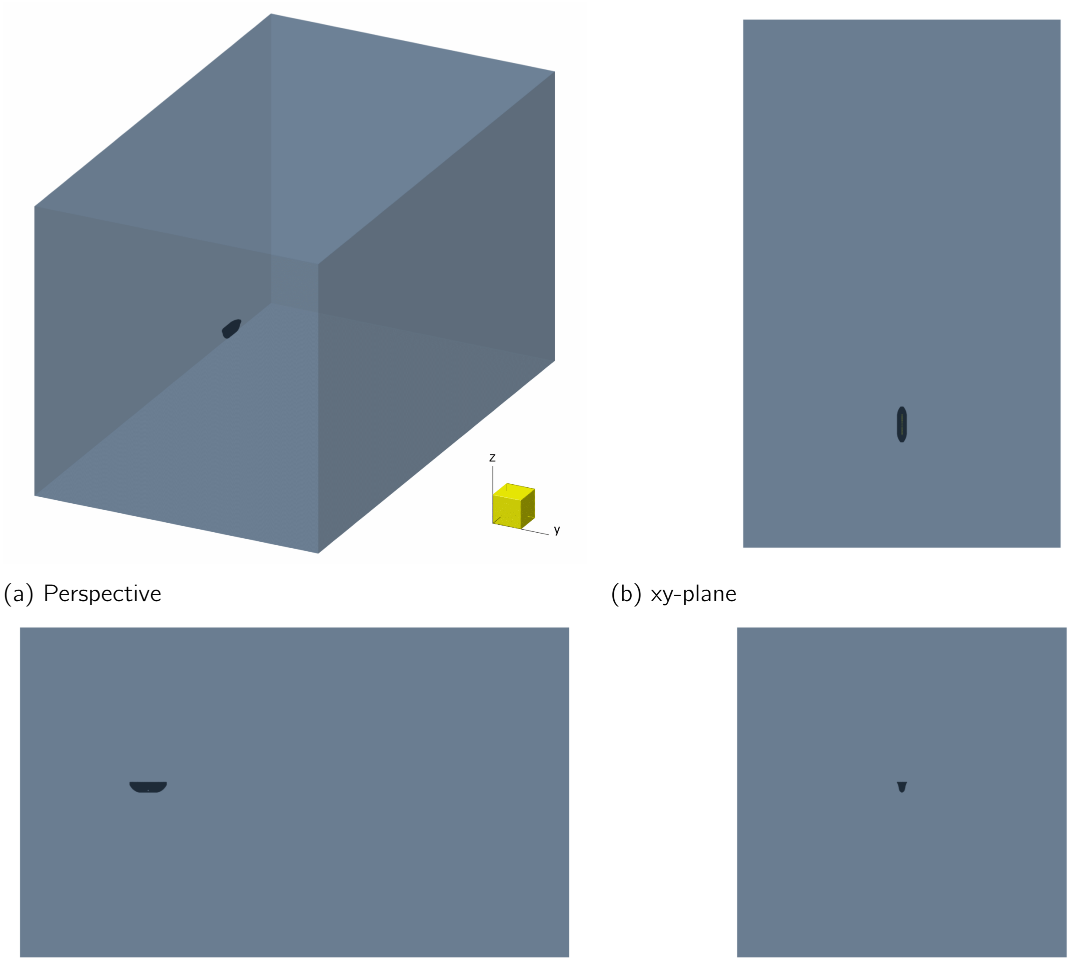

(a) Perspective

(b) xy-plane

(c) xz-plane

(d) yz-plane

Figure 3.5: Overview on the computational domain for the Nienhuis Wedge showing set-up 2.

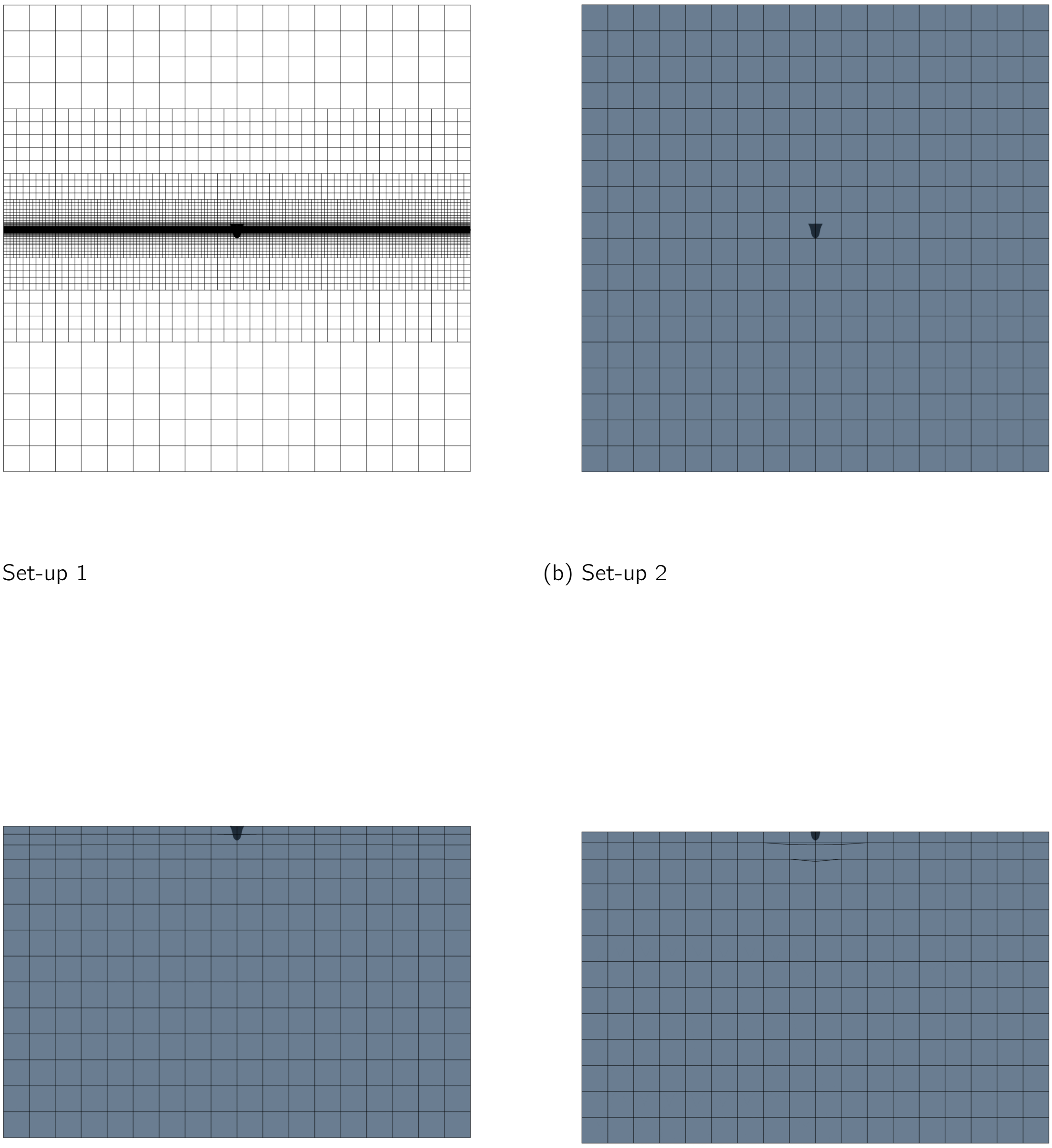

(a) Set-up 1

(b) Set-up 2

(c) Set-up 3

(d) Set-up 4

Figure 3.6: Overview of the yz-plane of the computational domain for the Nienhuis Wedge for the set-up's 1,2,3 and 4.

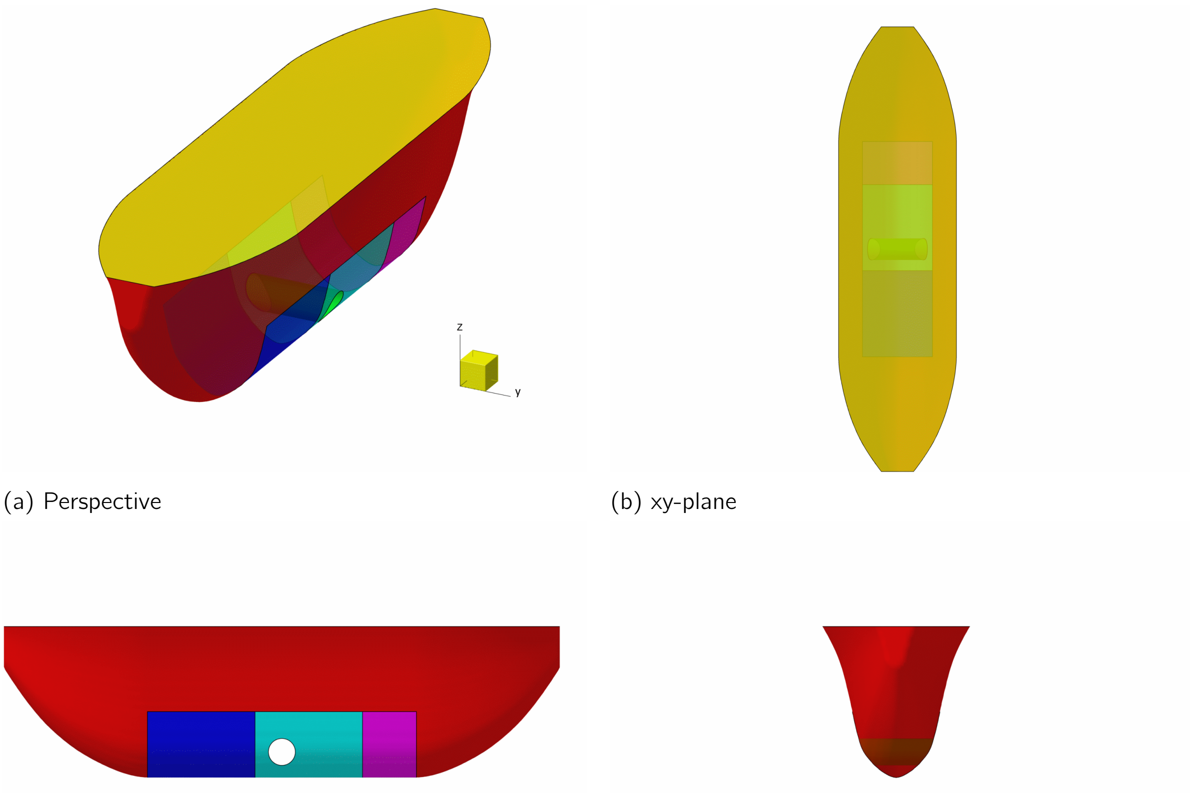

(a) Perspective

(b) xy-plane

(c) xz-plane

(d) yz-plane

Figure 3.7: Overview on the definition of the different solids for the Nienhuis Wedge: Yellow= Deck (only applicable for set-up 1 and 2) , red= Hull, blue= front_midship, tourquoise= TT_side, green= TT_tunnel, magenta= aft_midship

refinement boxes are defined, their coordinates are shown in Table 3.3 and a curve refinement along the tunnel-hull intersection is applied. All refinements are summarized in Table 3.4.

Table 3.3: Definition of the refinement boxes used for the Nienhuis wedge.

	lower boundary			upper boundary		
Name	x [m]	y [m]	z [m]	x [m]	y [m]	z [m]
Box 1	1.4	-1.5	0	2.0	1.5	0.377
Box 2	1.475	-0.05	0.077	1.625	0.05	0.227
Box 3	1.475	-0.25	0.077	1.625	-0.05	0.227
Box 4	1.475	0.05	0.077	1.625	0.25	0.227
Box 5	1.475	-0.6	0.077	1.625	-0.25	0.227
Box 6	1.475	0.25	0.077	1.625	0.60	0.227

The refinement method used in Hexpress successively subdivides cells and therefore the initial mesh cell is divided by a factor of 2^n, where n is the number of refinements. Therefore a refinement number of five represents a subdivision of one initial cell into $2^5 = 32$ cells in each geometric direction. As all target cell sizes are set to 0,0,0 it is ensured that the algorithm refines exactly the number of times specified.

Table 3.4: Number of refinements used and their corresponding adaptation criteria. The adaptation criteria and refinement method are described in [19]

		Adaptation criteria		
Name	Number of refinements	Distance	Curvature	Target cell size
Global	12	na	na	na
TT_tunnel	7	0	1	0 0 0
TT_side	7	0	0	0 0 0
front_midhsip	6	0	0	0 0 0
aft_midship	6	0	0	0 0 0
hull	5	0	0	0 0 0
deck	3	0	0	0 0 0
free surface (only set-up 1)	12	0	0	0.775 0.775 0.0031
TT edges	8	0	1	0 0 0
TT edges	8	0	1	0 0 0
Box 1	6	0	0	0 0 0
Box 2	7	0	0	0 0 0
Box 3	8	0	0	0 0 0
Box 4	8	0	0	0 0 0
Box 5	7	0	0	0 0 0
Box 6	7	0	0	0 0 0

The last step of the mesh generation is that viscous layers are inserted close to the solids. The number of viscous layers is dependent on the expansion ratio, the cell sizes close to the surface and the width of the first cell close to a surface y_{wall} which is in Numeca FineMarine defined as [19]:

$$y_{wall} = 6\left(\frac{u_{ref}}{\nu}\right)^{-\frac{7}{8}}\left(\frac{L_{ref}}{2}\right)^{\frac{1}{8}} y+ \tag{3.1}$$

Where u_{ref} and L_{ref} are the reference velocity and length, ν is the kinematic viscosity and $y+$ the dimensionless wall distance. The values used for the calculation of the first cell size is shown in Table 3.5, for the kinematic viscosity the water properties shown in Table 3.6 are used.

Table 3.5: Reference velocity and length for the calculation of the first cell close to a surface y_{wall}

Solid names	L_{ref} [m]	u_{ref} [m/s]	$y+$ wall function [-]	$y+$ no slip [-]
TT_tunnel	0.361	3.0	30	1
All other	3.1	0.478	30	1

3.2.3. Computation settings

All computations are solved using an unsteady RANS solver (Numeca FineMarine), a multifluid approach is used with the properties specified in Table 3.6. For computations without a free surface (set-up 2,3 and 4) the initial free surface height is defined at 30 [m] above the keel, which is far outside of the domain (compare [20]).

Table 3.6: Water and air properties, adapted from [15, 5-2]. The properties are not based on Nienhuis, as the properties of the model tests are unknown.

Property	Symbol	Unit	Value
Density of water	ρ_w	[kg/m^3]	998.4
Dynamic viscosity of water	μ_w	[N s/m^2]	1.04e-03
Density of air	ρ_a	[kg/m^3]	1.2
Dynamic viscosity of air	μ_a	[N s/m^2]	1.85e-05
Gravity intensity	g	[m/s^2]	-9.81

The solving algorithm of Numeca FineMarine is based on a reference length and reference velocity. As reference length the length of the wedge (3.1 [m]) is used and the reference velocity is set to the ship velocity u_s under consideration. The SST Menter k-ω turbulence model is used in all cases. The boundary conditions are defined as follows:

- **Solids of the wedge** *Wall function* for $y+$ of 30 [-], *no-slip* for $y+$ of 1[-]
- **Deck** *Slip*. The deck is only defined for set-up 1 and 2
- **Domain sides** *Far field* (all velocity components are zero)
- **Bottom of the domain** *Updated hydro-static pressure*
- **Top of the domain** *Updated hydro-static pressure*, for set-up 1 and 2, *mirror* for set-up 3 and 4

The motion in the length direction of the ship is imposed. A half sinusoidal ramp is used for a certain time to reach the reference velocity. The motion is defined in the negative x-direction. The five remaining degrees of freedom are fixed.

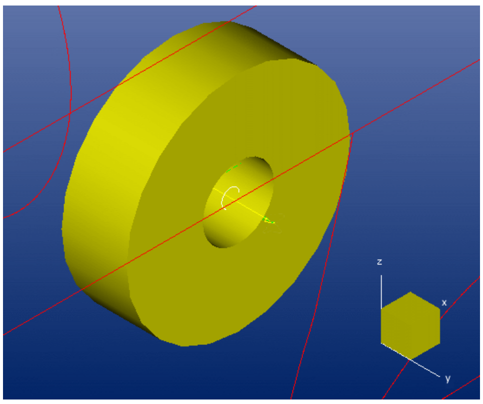

Figure 3.8: The geometry of the actuator disk. The dimensions are shown in Table 3.7

The propeller is modelled as an actuator disk. Figure 3.8 shows a rendering of the actuator disk used for the computations. In Table 3.7 the dimensions are shown, which are based on the dimension of the propeller used by Nienhuis [1]. The settings are: uniform force distribution without tangential forces and no body force update.

Table 3.7: Dimensions of the actuator disk. The dimensions are based on the model Nienhuis used [1].

Property	Unit	Value
Inner radius	[m]	0.0225
Outer radius	[m]	0.07112
Thickness	[m]	0.0415
Center coordinates	[m]	1.55 0.0 0.152
Shaft direction	[m]	0.0 1.0 0.0

3.3. Base case studies

First a representative base case is established to analyze the behavior in a qualitative and quantitative way and to find good computation settings. As base case a thrust T of 10 [N] and a ship speed u_s of 0.318 [m/s], which corresponds to a Froude number Fn of 0.058 [-] is chosen.

For this base case different studies are performed. At the beginning of each study a small summation of the important settings are given. During the set-up study the best set-up is found which neglects the free-surface. After that a discussion on the effect of non-linear iterations and convergence criteria is presented. The effect of the time step and the cell Courant number is covered in a study after that. In an actuator disk study the best representation of the propeller for this case is obtained. Finally with an analysis of the first layer thickness a basic computation configuration is found.

3.3.1. Set-up study

As the main focus of this study is to vary the cross-section of the tunnel thruster it is interesting to neglect the free-surface, as it requires a lot more cells. However to do this a suitable set-up needs to be selected to get comparable results. The general settings for this set-up study are:

- free-surface modeling varied
- grid refinement ratio r=2
- $y+$=30 [-], wall function
- actuator disk: uniform distribution, no tangential forces
- 1500 [-] time steps with time-step of 0.097 [s]
- 4 non-linear iterations, 2 orders convergence criterion
- ship speed u_s=0.318 [m/s], thrust T=10 [N]

For the set-up study the set-up's 1,2,3 and 4 are calculated with 1500 [-] time steps, with the recommended time-step of 0.097 [s]. This recommendation is defined by Numeca as 1 [%] of the ratio of the reference length L_{ref} and the reference speed u_{ref}:

$$t = 0.01\frac{L_{ref}}{u_{ref}} \tag{3.2}$$

The 1500 [-] time steps can be split in three sections. During the first 500 [-] time steps the wedge is accelerated to the constant defined speed of 0.318 [m/s] in the negative x-direction. The following 500 [-] time steps are used to stabilize the solution. The last 500 [-] steps will be used in the analysis and are therefore considered as measuring section. A schematic view of this configuration is shown in Figure 3.9. The measuring section is in this study 48.5 [s] and the wedge travels nearly 5 L during that time.

All computations uses four non-linear iterations per time step, causing that the convergence criterion is not reached. Special attention to the time step, cell Courant number and convergence criterion is given in-depth in Section 3.3.3. The results of the four set-up's are comparable.

Qualitative

The qualitative comparison is based on the results of the last time step. It is known due to the unsteady behavior of the flow that a lot of quantities vary significantly in time. It is assumed that the global behavior

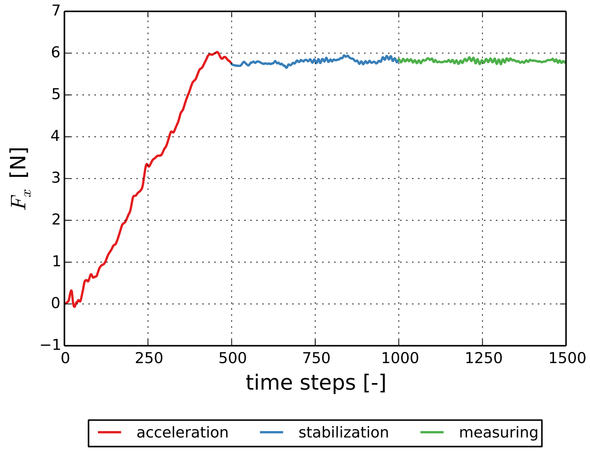

Figure 3.9: Overview of the different phases of the computation. Illustrated using the time trace of the resistance in the ship direction F_x for set-up 1.

can be studied based on the last time step.

The first visualization of the flow is made by creating a cutting plane at the vertical center location of the tunnel at z=0.152 [m]. All quantities are displayed on this cutting plane. The selected view is in the xy-plane with the positive x-direction to the right, the positive y-direction to the bottom, the movement of the wedge is towards the left and the thrust is applied pointing downwards. The contour plot shows the magnitude of the vector components in the xy-plane and is calculated using the Pythagoras theorem as:

$$v_{rel} = \frac{\sqrt{u^2 + v^2}}{u_s} \tag{3.3}$$

Where u and v are the local velocity component in the x- and y-direction respectively, which is normalized with the ship velocity u_s. On top of the contour plot of the relative velocity v_{ref} the vector components of each grid are plotted to visualize the direction of the velocity.

The relative velocity is plotted for the four set-up's in Figure 3.10. The flow is accelerated by the actuator disk. The water in the front of the tunnel is sucked into it. Resulting in a small area of very low velocities at the back of the tunnel inlet. In the tunnel the flow is accelerated and distributed by the actuator disk. After the actuator disk the velocities at the center are very low, as the actuator disk is modeled as annulus. On the sides the velocity is increased to values of up to v_{ref}=3 [-]. Towards the outlet the flow keeps this shape, while moving a bit to the front. When the flow leaves the tunnel it is bend by the surrounding cross-flow. The surrounding flow is decelerated as it encounters the jet-flow of the tunnel. Behind the jet a region with lower velocity is noticed. Next to that there is a region with zero velocity in the wake of the jet. The noticed flow behavior is mentioned by multiple authors in literature [1], [7], [21], [22], [23], [24].

All four set-up's show this general behavior. The biggest differences are noticed near the wedge behind the jet outlet. In general it can be stated that the agreement of the four set-up's is good for the general flow behavior.

For the second comparison the hydrodynamic pressure is plotted as contour on the surfaces close to the bow thruster tunnel. The view is in the xz-plane showing either the inlet side (viewing from the negative y-direction) or the outlet side (viewing from the positive y-direction). The wedge is moving in the left direction. The hydrodynamic pressure is plotted in the range -1000 and 300 [Pa] with isobar's of every 50 [Pa].

At the inlet side (Figure 3.11) a small region of low pressure is shown before the tunnel. This region reaches approximately 1/2 D towards the left. Behind the tunnel a large region with high pressure is noticed. However the magnitude of these pressures is small. All four set-up's show these two pressure regions. The low pressure region is similar for all set-up's. For the high pressure region differences are noticed. For set-up 1 (with free-surface) the high pressure region extends upwards of the surfaces under consideration.

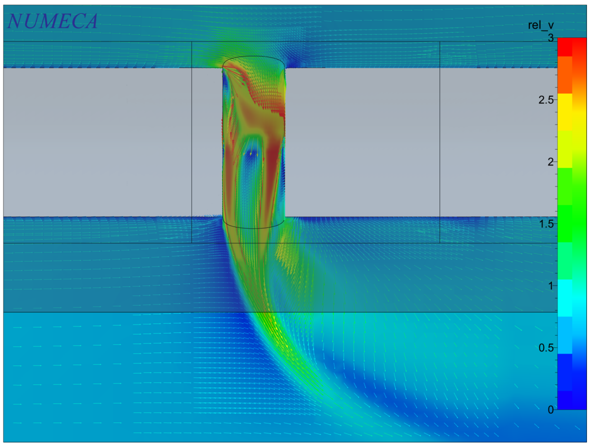

(a) Set-up 1

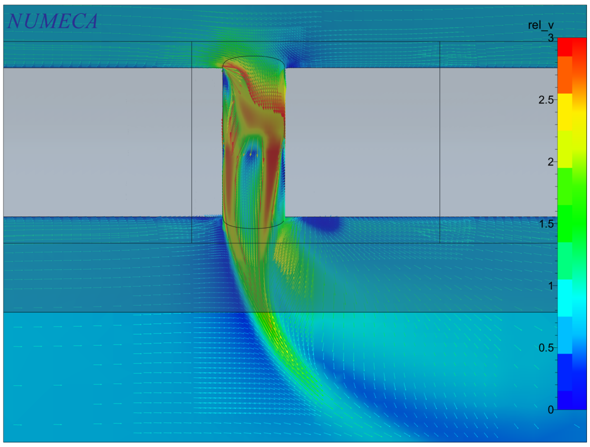

(b) Set-up 2

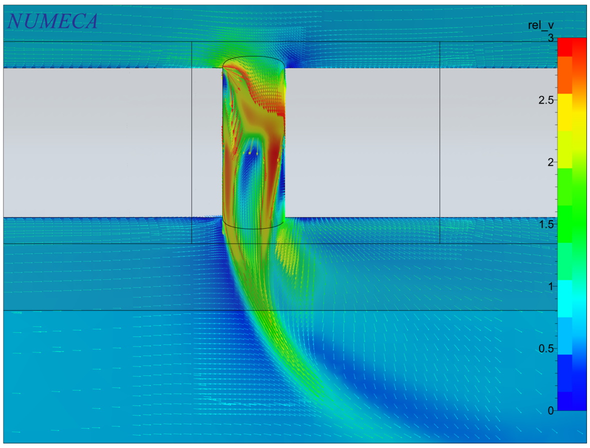

(c) Set-up 3

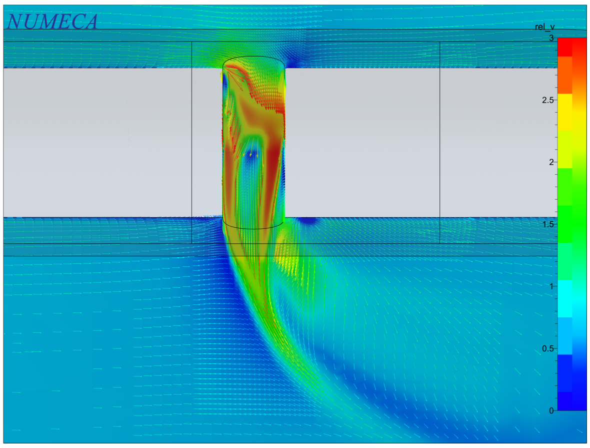

(d) Set-up 4

Figure 3.10: Relative velocity v_{rel} in the xy-plane at z=0.152 [m]. Topside of the wedge is inlet side and bottom the outlet side.

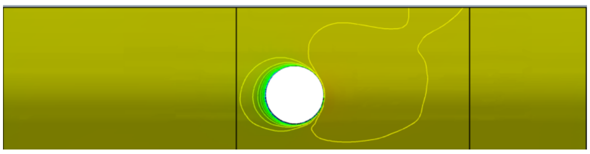

(a) Set-up 1

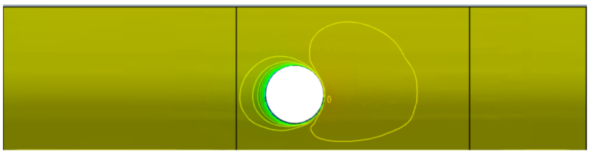

(b) Set-up 2

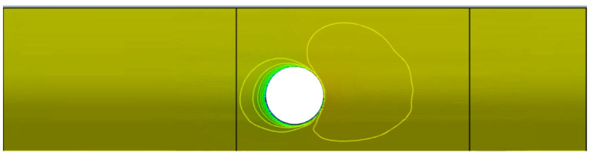

(c) Set-up 3

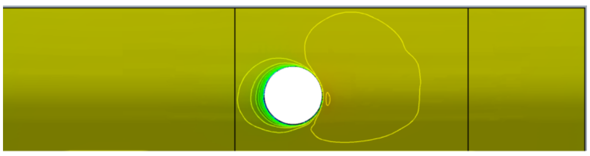

(d) Set-up 4

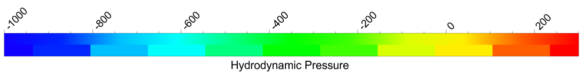

(e) Pressure scale

Figure 3.11: Hydrodynamic pressure of the inlet side plotted on the solids: front_midship, TT_side and aft_midship. Pressures are plotted on the range -1000 to 300 [Pa] with isobar's every 50 [Pa].

The outlet side shown in Figure 3.12 shows different pressure regions. Before the tunnel a high pressure region exist with a low magnitude. A low pressure region exists on the backside and on top of the tunnel. Behind the tunnel regions of constant pressure exists as well, but have a minor influence due to their magnitude. The positions of the pressure regions agree with literature (Compare [3], [4], [1], [21] and [25]). The plots show that the highest pressure occurs close to the tunnel-hull intersection. This is logical as a sharp transition exists between the tunnel and the hull. During meshing this effect is taking into account by refining this section of the wedge the most.

The qualitative comparison has shown that the general flow and the pressure area are as expected and agree with literature. Based on the qualitative comparison alone it is not possible to select the best alternative for set-up 1 to neglect the free surface. However it should be remembered that the qualitative comparison is based on a snapshot in time.

Quantitative

In the quantitative comparison the obtained values are compared. For the global forces the complete time trace is known. The last 500 [-] time steps are used to create a mean value. For other quantaties such as pressure and velocity the values of the last time steps are used. All quantitative analysis make use of the standard error propagation, described in Appendix D.

First the resistance of the wedge is analyzed by studying the force in the x-direction. In Figure 3.13a the time trace of the last 500 [-] time steps is shown. The double body approach with a mirror plane at the waterline (set-up 4) shows the best agreement with the free surface case (set-up 1). Set-up 2 and set-up 3 overestimate the resistance significantly compared to set-up 1. Set-up 2 has a deck with no slip condition which is submerged underwater, leading to resistance along the complete body. For set-up 1 and 4 only the underwater ship contributes to the resistance. As the mirror plane for set-up 3 is placed higher as compared to the set-up 1 and 4, a higher fraction is submerged and therefore contributes to the resistance. As the deck is part of the mirror plane the resistance for set-up 3 is less than for set-up 2.

All four set-up's show an oscillation, to analyze the behavior of these oscillation a fast Fourier transform is performed. The resulting frequency spectrum for frequencies of 0 to 0.5 [1/s] in Figure 3.13b shows a dominant peak at around 0.09 to 0.1 [1/s] for set-up 1, 3 and 4. This frequency corresponds with a period of 11 to 10 [s], which can be recognized in the time trace. Set-up 2 has completely other peaks as set-up 1,3 and 4, which suggest that set-up 2 is not a suitable alternative to a free surface calculation. The oscillation of set-up 2 corresponds with a period of 4.5 [s], which can again be seen in the time trace in Figure 3.13a. The sources of these peaks can not be distinguished.

When looking at the time trace of the force in y-direction in Figure 3.14a one sees a higher oscillation in amplitude and different results. Set-up 3 seems to have problems to converge. This results in a diverse frequency spectrum (Figure 3.14b). The amplitudes of the frequency spectrum are indeed higher than for the force in x-direction. Again set-up 2 shows different peaks compared to set-up 1,3 and 4. The data of the time trace is shown in Table 3.8.

Table 3.8: Results of the set-up study. The calculated mean μ and standard deviation σ are based on the last 500 [-] time steps

	F_x		F_y	
Set-up	μ [N]	σ [N]	μ [N]	σ [N]
1	5.81	0.03	-0.33	0.19
2	10.38	0.02	-0.57	0.18
3	7.47	0.07	0.14	0.36
4	6.06	0.05	-0.79	0.26

To study the behavior of the velocities near the outlet side of the tunnel, eight different positions are analyzed in Figure 3.15. Half a diameter before the tunnel outlet (x/D=-0.5 [-]) the v velocity in the direction of the tunnel is nearly 0 [-], while the u velocity is u/u_s=1 [-]. The graph of u is increasing from rest near the wedge to 1 [-], due to the viscous layer. At the center of the tunnel (x/D=0.5 [-]) and further aft an interaction between the local jet speed v and ship speed u is visible. The ship speed decreases due

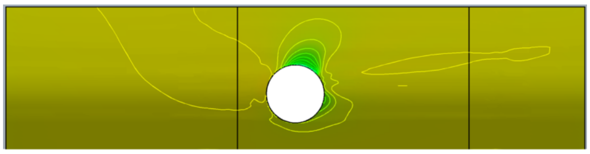

(a) Set-up 1

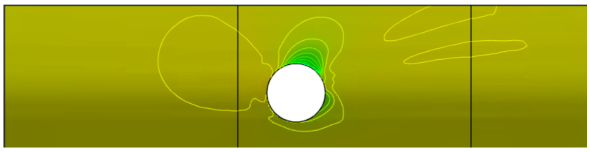

(b) Set-up 2

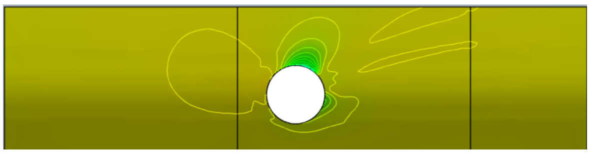

(c) Set-up 3

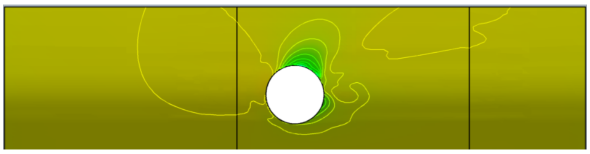

(d) Set-up 4

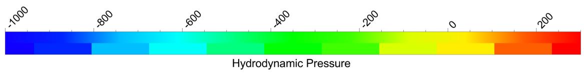

(e) Pressure scale

Figure 3.12: Hydrodynamic pressure of the outlet side plotted on the solids: front_midship, TT_side and aft_midship. Pressures are plotted on the range -1000 to 300 [Pa] with isobar's every 50 [Pa].

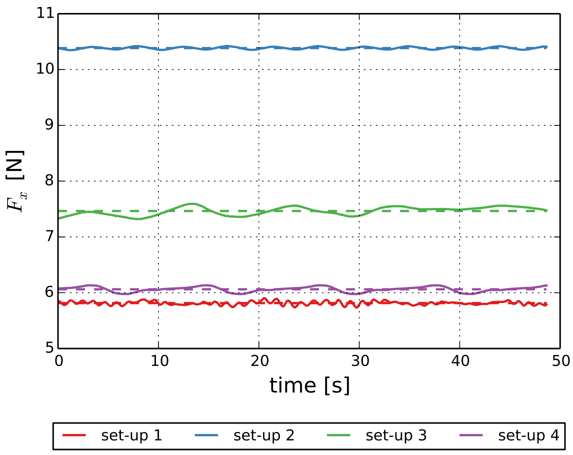

(a) Time trace x-direction

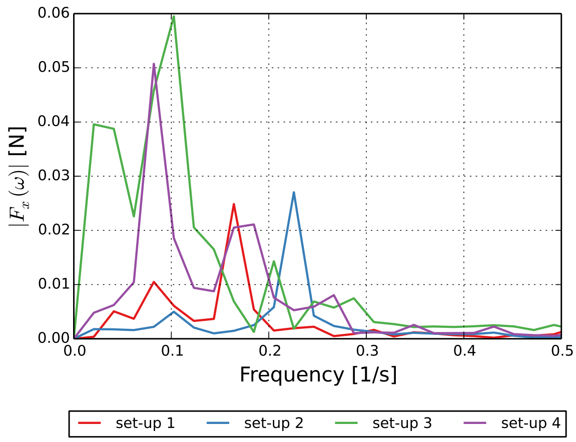

(b) Frequency spectrum x-direction

Figure 3.13: Set-up study: Time trace and frequency spectrum of the force in x-direction of the last 500 [-] time steps. The dashed line in the time trace indicates the mean value.

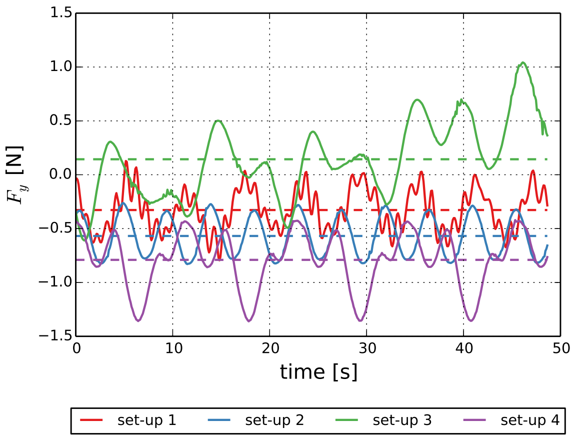

(a) Time trace y-direction

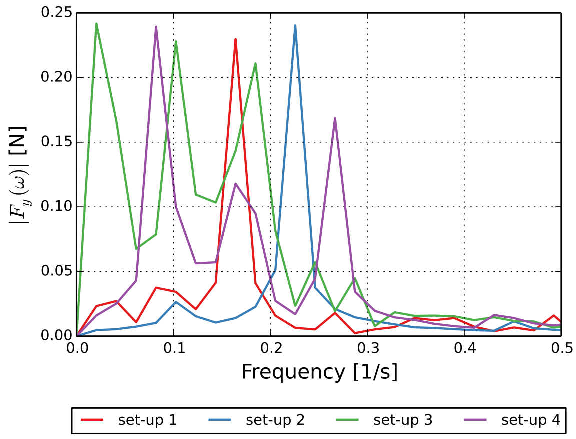

(b) Frequency spectrum y-direction

Figure 3.14: Set-up study: Time trace and frequency spectrum of the force in y-direction of the last 500 [-] time steps. The dashed line in the time trace indicates the mean value.

to the flow from the tunnel and even gets negative (x/D = 1.0 and 1.5 [-]), while the normalized jet speed v/u_s reaches values up to 2.5 [-] near the tunnel.

The pressure profile along the side of the wedge is shown in Figure 3.16. The pressure on the side of the wedge is taken at the centerline of the cross-section (z=0.152 [m]) and has been normalized with the ship velocity u_s and the density of water ρ_w using Bernoulli as:

$$C_P = \frac{2p}{\rho_w u_\infty^2} \tag{3.4}$$

The trend in Figure 3.16 is consistent for all four set-up's, agrees with the qualitative comparison and is as expected. The same trend has been reported in [1], [4] and [21].

Based on the presented study it is shown that all set-up's produce qualitative reliable results. The results of the set-up study in itself are quantitative reliable, however only set-up 4 corresponds with set-up 1 in an acceptable way, for the measured forces. All four set-up's are qualitative valid, as the flow pattern is as expected and documented in many cases. Quantitative validity couldn't be checked, however pressure and velocity distributions seem to be logical and show the same trends as literature.

Table 3.9: Computational time of the set-up study (1500 time steps), performed using a computer with 8 cores (@3.06 Ghz) and 48 GB RAM

		computation time	
Set-up	Number of cells	total [min]	per time step [s]
1	3944321	2232	89.3
2	594416	103	4.1
3	585549	199	8.0
4	564196	189	7.6

Based on the set-up study and after considering the computational gain shown in Table 3.9 set-up 4 is selected, as it has shown good agreement with the free surface calculations and decreases the computation time by a factor of 11 [-]. From now computations are performed using set-up 4.

3.3.2. Study on the effect of non-linear iterations and convergence criterion

During the set-up study it was noticed that the settings for the non-linear iterations and convergence criterion, which are recommended by Numeca for ship resistance computations [15], caused the solver to stop the non-linear iterations based on the number of iterations, not based on the convergence criterion. This basically means we know for sure that at each time step four non-linear iterations were performed, but we have different order of convergence. In this study it is checked how to deal with this in the best way. For the study the following settings apply:

- non-linear iterations are varied, convergence criterion of 2 orders is kept constant
- grid refinement ratio r=2
- free-surface: double body with mirror plane at waterline
- y+=30 [-], wall function
- actuator disk: uniform distribution, no tangential forces
- 1000 [-] time steps with time step of 0.097 [s]
- ship speed u_s=0.318 [m/s], thrust T=10 [N]

As an increase in non-linear iterations will cause an increase in computation time the following configuration is chosen: First 1000 [-] time steps (500 [-] acceleration and 500 [-] stabilization), with four non-linear iterations are simulated. For the n_{nl}=256 [-] case, the simulation is restarted and computed for 500 [-] additional time steps which are measured with 256 non-linear iterations. For the n_{nl}=4 [-] case, the simulation is restarted after the first 1000 [-] time steps and additional 4000 [-] time steps with four non-linear iterations are simulated. The 4000 [-] time steps are divided in blocks of 500 [-] time steps which are analyzed independent of each other.

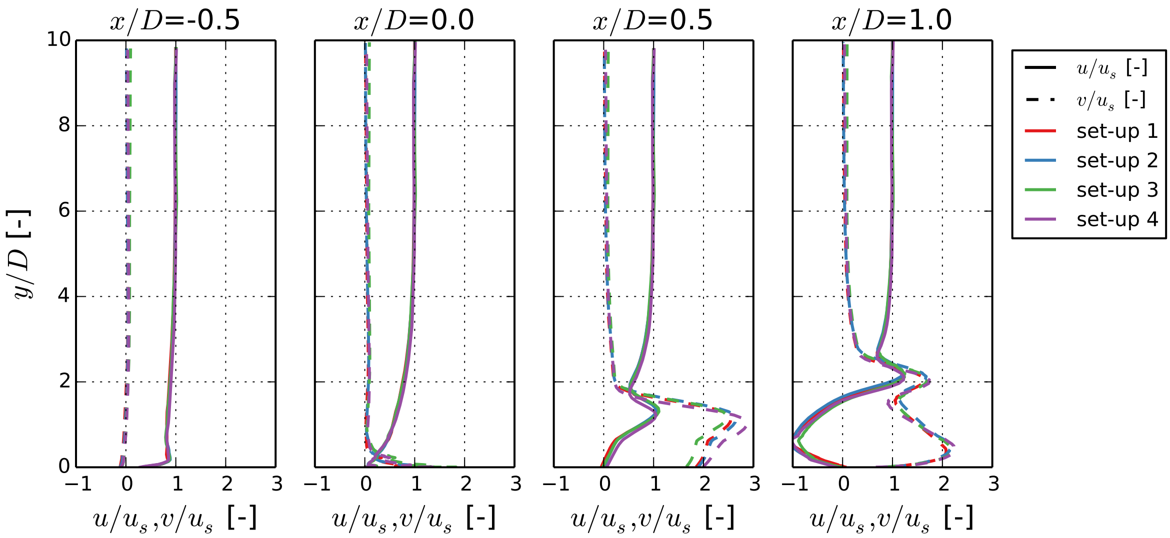

(a) x/D=-0.5 to 1.0 [-]

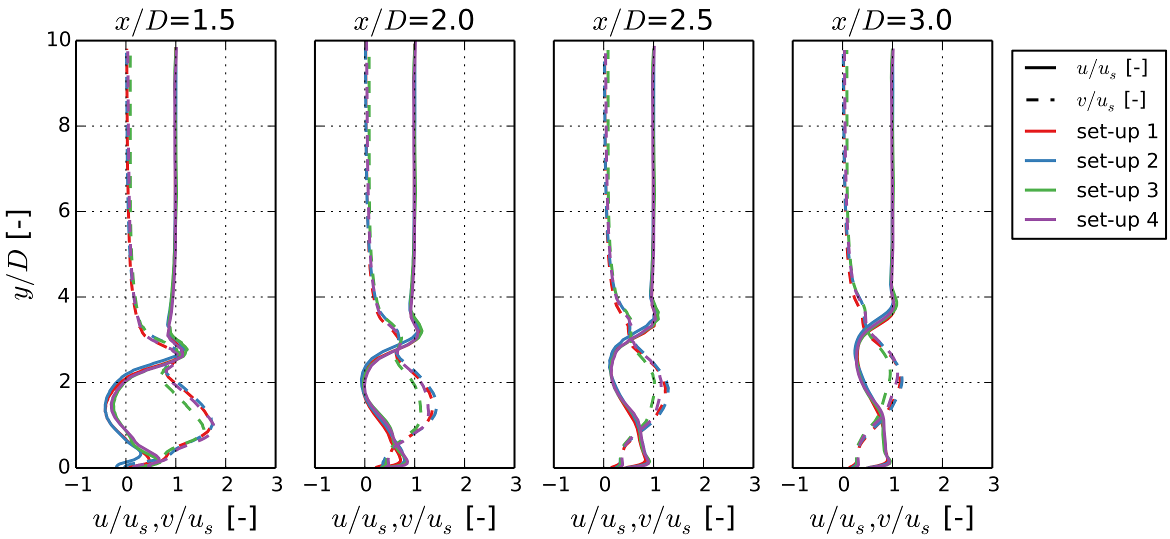

(b) x/D=1.5 to 3.0 [-]

Figure 3.15: Velocity profile in the xy-plane at the center height of the tunnel thruster (z=0.152 [m]) on the outlet side. x/D=0 [-] is situated at the forward most point of the tunnel. u velocities refer to the velocity in the longitudinal direction of the wedge (x-direction) and v velocities to the transverse velocities in the y-direction.

.

Qualitative

The resulting flow is shown in Figure 3.17. Both show a similar behavior and the only difference is again close to the wedge behind the jet for the n_{nl}=4 [-] case. Based on the flow profile no conclusion can be drawn.

For the hydrodynamic pressure at the inlet side, see Figure 3.18, no difference can be noticed. Both situations are close to being identical. The influence of the convergence criterion can not be seen at the inlet side.

On the outlet side on the other hand small differences exist. However these are most likely due to that a snapshot is taken. The qualitative comparison between the two cases n_{nl}=256 [-] and n_{nl}=4 [-] shows no difference to each other. For this case the non-uniform convergence of the n_{nl}=4 [-] seems to have no effect on the behavior of the flow and the pressure distribution.

Quantitative

In Figure 3.20a the time trace of the resistance is shown. It can be noticed that all time bins related to n_{nl}=4 [-] show the same behavior and are just shifted in time. The n_{nl}=256 [-] case shows a higher fluctuation, which results in a slightly different mean and a higher standard deviation (compare with Table 3.10).

This can also be seen in the frequency spectrum in Figure 3.20b. It can be seen that all n_{nl}=4 [-] cases show the same trend. The first peak at 0.9 [1/s] corresponds with around 110 [-] time steps in Figure 3.20a. Each of the n_{nl}=4 [-] cases show four periods. For the n_{nl}=256 [-] case the same peak is noticed. The first peak corresponds with a period of 500 [-] time steps.

The force in the y-direction shows the same behavior (Figure 3.21a). Here the fluctuation of the n_{nl}=256 [-] case causes a significant change in the mean value.

For the frequency domain of the force in y-direction in Figure 3.21b the exact same trends are visible as for the x-direction in Figure 3.20b.

Table 3.10: Results of the convergence study. The calculated mean μ and standard deviation σ are based on the last 500 [-] time steps

		F_x		F_y	
n_{nl} [-]	time steps [-]	μ [N]	σ [N]	μ [N]	σ [N]
256	1000-1500	6.046	0.066	-0.584	0.308
4	1000-1500	6.062	0.047	-0.790	0.259
4	1500-2000	6.059	0.046	-0.789	0.259
4	2000-2500	6.056	0.048	-0.818	0.272
4	2500-3000	6.062	0.048	-0.793	0.259
4	3000-3500	6.061	0.046	-0.788	0.261
4	3500-4000	6.059	0.046	-0.792	0.257
4	4000-4500	6.056	0.048	-0.820	0.272
4	4500-5000	6.068	0.050	-0.804	0.256

When analyzing the signal in the frequency domain, it becomes clear that all time bins of n_{nl}=4 [-] have the same peaks.

For this study also two other speed thrust configurations have been tested. When the ship has zero speed and the thrust is 10 [N] and when the thrust is 0 [N] and the ship velocity is 0.318 [m/s]. The same trends are noticed.

For the presented study it can be concluded, that an increase in time steps for the n_{nl}=4 [-] case results in no differences. The resulting mean and standard deviations are very close to each other. The case of n_{nl}=256 [-] shows more fluctuation and seems to have more problems to converge to one value. It is however known that the convergence criterion of 2 orders is reached at each time step for n_{nl}=256 [-]. Based on this study it is concluded to use 256 non-linear iterations, because the convergence is uniform for all time steps. This increases the comparability of the computations. To keep the computation time reasonable the first 1000 [-] time steps are computed with 4 non-linear iterations and then a restart of the

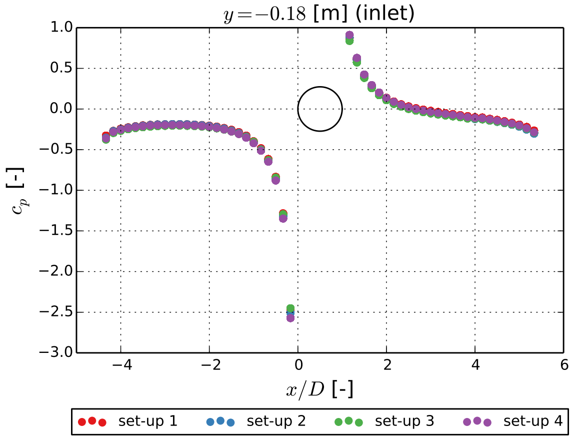

(a) Inlet

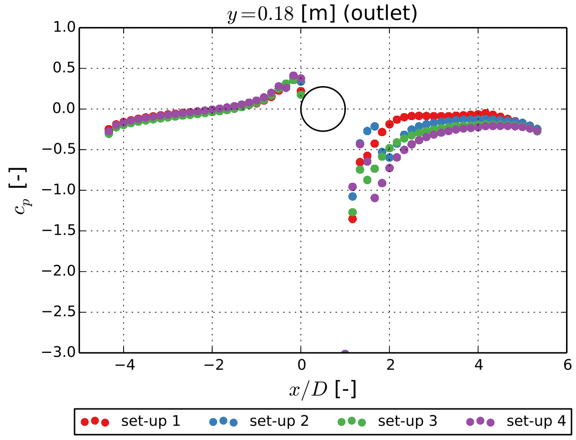

(b) Outlet

Figure 3.16: Pressure profile along the side of the wedge at the center height of the tunnel thruster (z=0.152 [m]). x/D=0 [-] is situated at the forward most point of the tunnel.

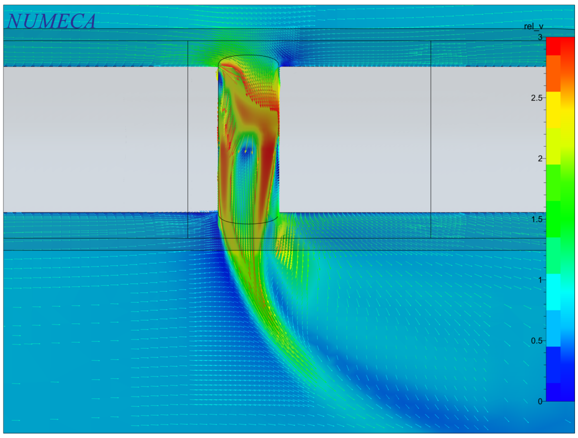

(a) n_{nl}=256 [-]

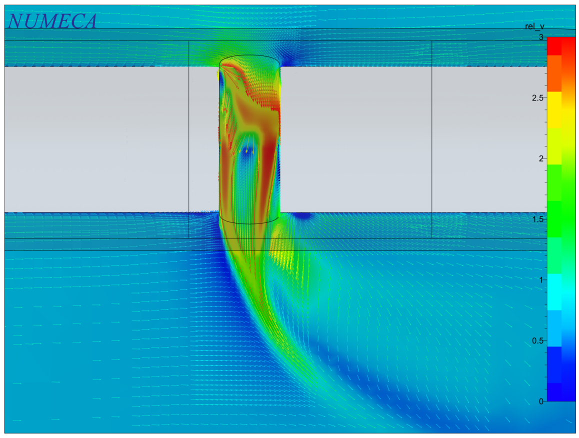

(b) n_{nl}=4 [-]

Figure 3.17: Relative velocity v_{rel} in the xy-plane at z=0.152 [m]. Topside of the wedge is inlet side and bottom the outlet side.

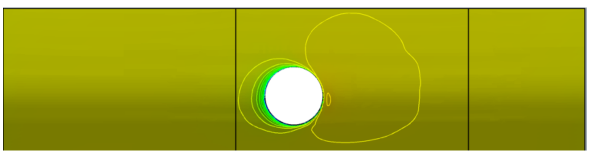

(a) n_{nl}=256 [-]

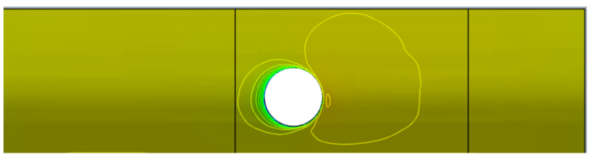

(b) n_{nl}=4 [-]

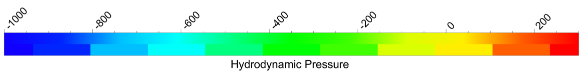

(c) Pressure scale

Figure 3.18: Hydrodynamic pressure of the inlet side plotted on the solids: front_midship, TT_side and aft_midship. Pressures are plotted on the range -1000 to 300 [Pa] with isobar's every 50 [Pa].

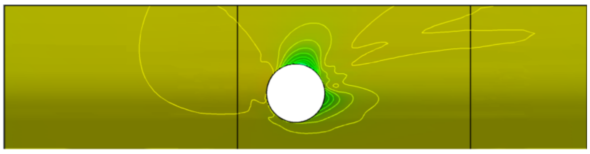

(a) n_{nl}=256 [-]

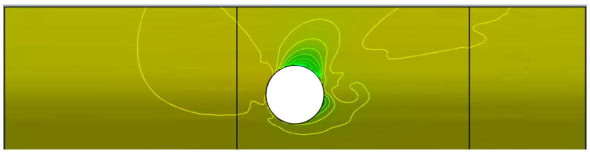

(b) n_{nl}=4 [-]

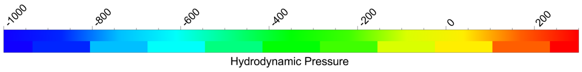

(c) Pressure scale

Figure 3.19: Hydrodynamic pressure of the outlet side plotted on the solids: front_midship, TT_side and aft_midship. Pressures are plotted on the range -1000 to 300 [Pa] with isobar's every 50 [Pa].

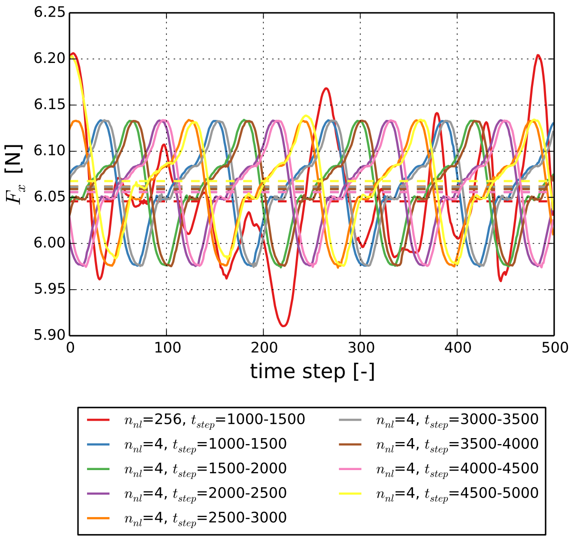

(a) Time trace x-direction

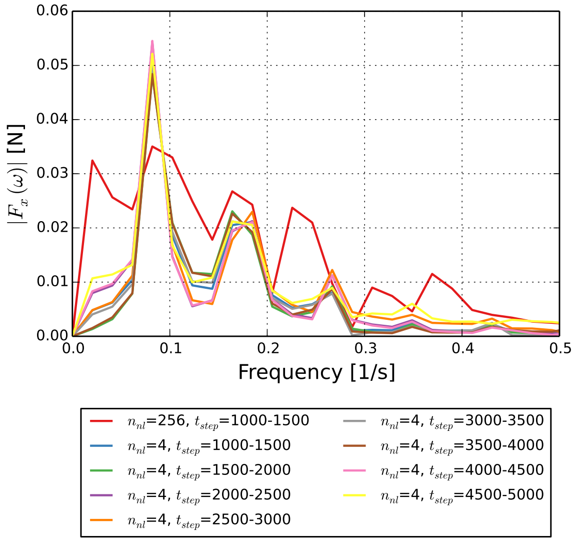

(b) Frequency spectrum x-direction

Figure 3.20: Convergence study: Time trace and frequency spectrum of the force in x-direction of the last 500 [-] time steps. The dashed line in the time trace indicates the mean value.

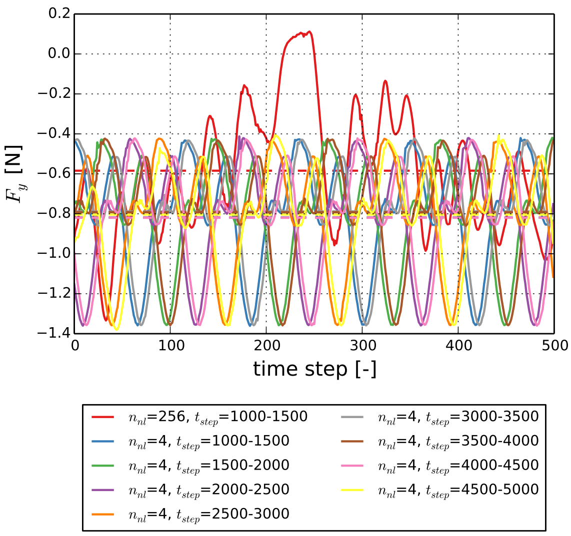

(a) Time trace y-direction

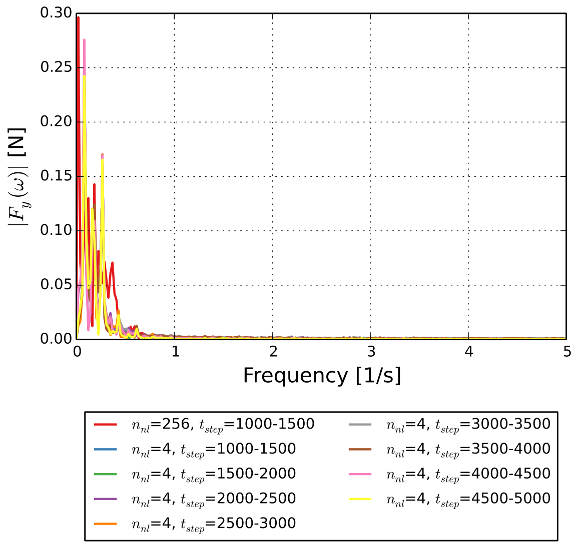

(b) Frequency spectrum y-direction

Figure 3.21: Convergence study: Time trace and frequency spectrum of the force in y-direction of the last 500 [-] time steps. The dashed line in the time trace indicates the mean value.

computation with 256 non-linear iterations is initiated for the measuring section of the computation. This approach is used for all further computations in this thesis.

3.3.3. Time step and cell Courant number study

Until now the recommended time step of Numeca is used. Which is a fraction of the reference length and velocity. This time step is therefore independent of the grid spacing, which implies that the cell Courant number will vary based on the grid. The cell Courant number Co is defined as:

$$Co = \frac{u_i \Delta t}{\Delta x_i} \tag{3.5}$$

Where u_i is the velocity at the cell, Δt is the time step in [s] and Δx_i is the cell size of cell i in [m]. An decrease in the grid size (increase in grid cells) will therefore cause a increase in the Courant number. The Courant number is a measure for the spatial and time discretization and values below 1 [-] are needed for explicit numerical schemes to be stable. For implicit schemes this does not apply. However it is recommended to keep the Courant number around 1 [-] or lower, as this means that a fluid particle can not move more than one grid cell during one time step [5]. The numerical scheme used in FineMarine are blended numerical schemes that are designed to not suffer from the Courant number limitation and are, according to Numeca, not sensitive to high Courant numbers [10]. It is however advised to keep the Courant number below 5 [-] for most engineering applications [15]. The general settings for this time step study are as follows:

- time steps are varied based on cell Courant number
- grid refinement ratio r=2
- free-surface: double body with mirror plane at waterline
- $y+$=30 [-], wall function
- actuator disk: uniform distribution, no tangential forces
- 4 non-linear iterations for 1000 [-] time steps, restart with 256 non-linear iterations
- ship speed u_s=0.318 [m/s], thrust T=10 [N]

During the computation Numeca calculates the Courant number of every cell, with the local cell size and local velocities using Equation 3.5. As the local velocities and local cell sizes are not known before hand a method is developed to get a Courant number C that results in acceptable cell Courant numbers Co after the computations. The time step is calculated as:

$$\Delta t = C\frac{\Delta x}{u} \quad where\ \Delta x = \left(\frac{V}{N_{cells}}\right)^{\frac{1}{3}} \tag{3.6}$$

With C being the global mean Courant number, Δx the mean cell size in [m], u the reference velocity in [m/s], V the volume of the domain in [m^3] and N_{cells} the number of grid cells. In this comparison the volume of the domain V is 24130.71 [m^3], the number of grid cells N_{cells} is 564196 [-] and the reference velocity u is taken as 0.318 [m/s]. The resulting time step depends on the global mean Courant number C and is shown in Table 3.11.

Table 3.11: Time step comparison

Case	C [-]	time step [s]	time steps needed [-]	max(Co) [-]	Majority of cells below Co [-]
A	0.088	0.097	500	438	94 [%] < 43.7
B	0.001	0.0011	44091	5.18	94 [%] < 0.518
C	0.01	0.011	4409	81.4	95[%] < 8.14

In Table 3.11 the cell Courant number Co of the three cases are given. The shown values are given for the last time step. The routine within FineMarine searches for the highest cell Courant number which is referred to as max(Co) and then creates a histogram with 10 bins of equal size. The majority of cells fall in the last bin. FineMarine gives the percentage of all cells that have a value lower than a tenth of the max(Co). This value is considered to be a good indication of the cell Courant numbers, next to that all calculations have been checked visual for the cell Courant number to confirm the results.

It should be noticed that between Case A and B the time step has been decreased by a factor of 88 [-]. Which means that it takes more than 44000 time steps to have the same measuring time/distance as in Case A (500 time steps). In the following comparison for Case B only 8101 time steps are used and for the other two cases 100 and 886 [-]. The calculation of mean and standard deviation is done for the same physical time to compare the different cases.

Qualitative

The flow velocity snapshots are made at the last time step. One can see in Figure 3.22 that with a decrease in time step the tunnel jet flow gets less smooth and 'steps' are visible. With the decrease in time step Δt also the time scale is decreasing and the sampling frequency is increasing. Therefore effects occurring on smaller time scales can get resolved by the turbulence model. Next to that it should be remembered that time averaged equations are used in the solver, which results in smoothing for high time steps Δt. For Case B (Figure 3.22b) the region behind the jet is largely effected and a large region of zero velocity is seen. The decrease in time step therefore has a significant effect on the flow.

For the hydrodynamic pressure on the inlet side in Figure 3.23 no visible effect is noticed. Small differences can be seen at the region behind the tunnel. Case C (Figure 3.23c) has no local high pressure spot directly to the left of the tunnel, while the other two cases show such a spot.

At the outlet side more differences between the three cases are noticed. In Figure 3.24 it can be seen that the locations of the pressure regions behind the tunnel are situated at different locations. The low pressure region close to the tunnel is moving more upwards of the tunnel when considering the change from Case A to Case C to Case B.

In general it can be stated that the change in time step Δt has a significant effect on the flow, as the time scale of the resolved simulation changes. With a decrease in Δt more local flow details become visible, but the computation time increases significant.

Quantitative

For the quantitative comparison the signal after the restart is plotted for the last 9.75 [s] ($1L$). The corresponding time steps used in this analysis together with the result is displayed in Table 3.12.

The effect of the different time steps can clearly be seen in the time trace of the resistance in the x-direction in Figure 3.25a. While the curve of Case A is smooth the curves of Case B and C show much more fluctuation, due to the small time steps. The figure can be compared to results from model tests. The difference between the three cases would be that the sampling frequency of the load cell is changed. Simply more points per second are sampled/ computed and therefore smaller timescales are analyzed. It can be seen that the standard deviation of Case A is higher than for the other two cases. A look at the frequency spectrum between 0 and 5 [1/s] in Figure 3.25b shows that Case A and B have a low frequency peak at around 0.1 [1/s] for Case B and 0.2 [1/s] for Case A. The peak for Case B corresponds with the total length of the time trace and the peak of Case A with the half of the length of the time trace. In the time trace a corresponding sinusoidal frequency of about 4.8 [s] is noticed. Case C on the other hand has the first significant peak at around 4.6 [1/s] which corresponds to oscillations of 0.22 [s] in the time trace. It seems that for Case C a resonance frequency is reached. As the peak around 4.6 [1/s] is only visible for Case C, not for Case A and B.

The time trace of the force in y-direction in Figure 3.26a shows a similar behavior as for the x-direction. Large occilations are noticed. While Case A is strictly negative, Case B and C are mostly positive. The same peaks in the y-direction in Figure 3.26b are noticed in the frequency spectrum as for the x-direction.

It can be stated that the change in time step has an influence on the obtained results. The dominant peaks in the frequency domain change depending on the time step, which indicates that local effects are considered during the analysis. The first peak in the frequency domain are probably an indication on the fluctuation of the flow, which can clearly be seen in the time trace.

The quantitative and qualitative comparison have shown that the result is depending on the time scale. It is assumed that by keeping the Courant number C constant the cell Courant number Co is approximately the same. Next to that it is assumed that by maintaining the Courant number different calculations are comparable. It is therefore concluded to use the Courant number C of 0.01 [-] as this results in the

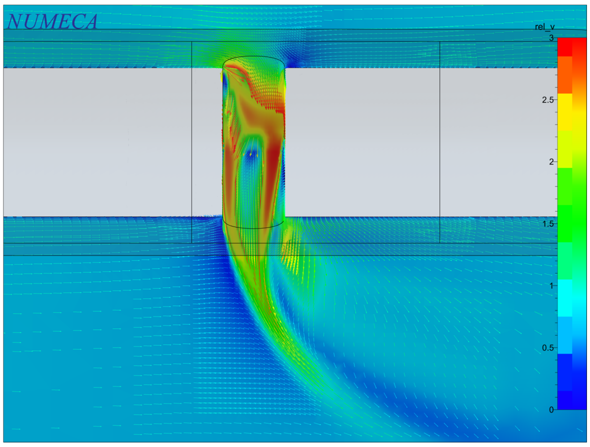

(a) Case A

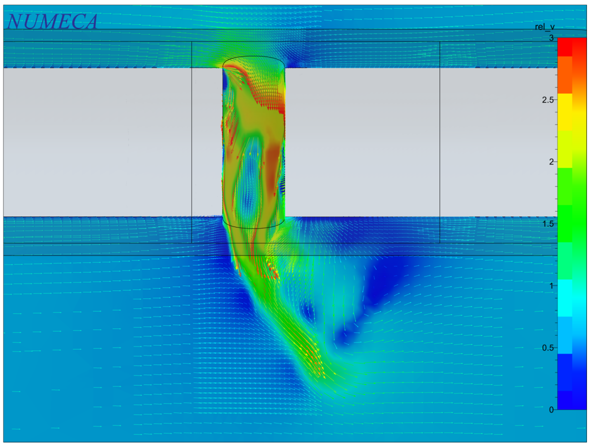

(b) Case B

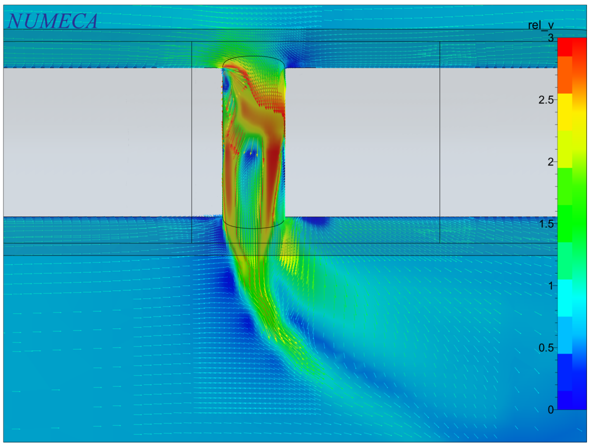

(c) Case C

Figure 3.22: Relative velocity v_{rel} in the xy-plane at z=0.152 [m]. Topside of the wedge is inlet side and bottom the outlet side.

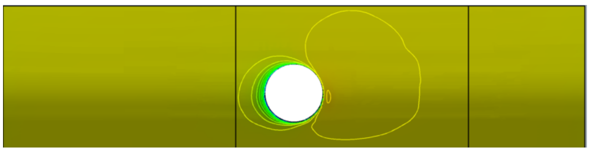

(a) Case A

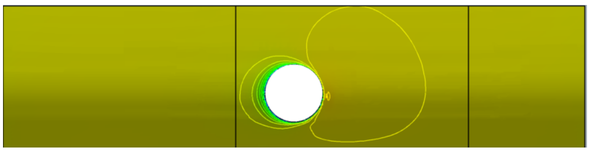

(b) Case B

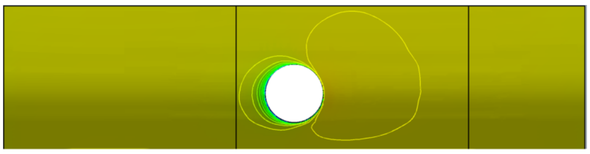

(c) Case C

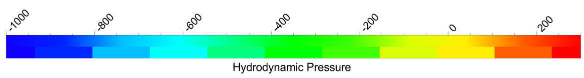

(d) Pressure scale

Figure 3.23: Hydrodynamic pressure of the inlet side plotted on the solids: front_midship, TT_side and aft_midship. Pressures are plotted on the range -1000 to 300 [Pa] with isobar's every 50 [Pa].

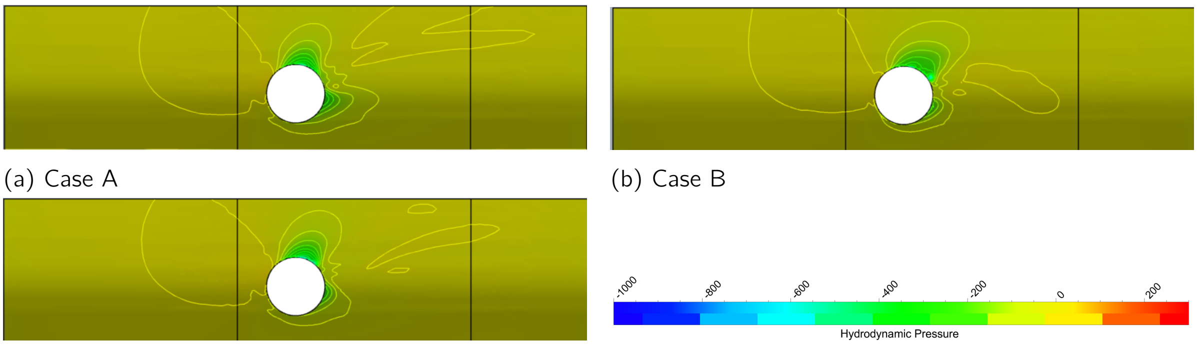

(a) Case A (b) Case B

(c) Case C (d) Pressure scale

Figure 3.24: Hydrodynamic pressure of the outlet side plotted on the solids: front_midship, TT_side and aft_midship. Pressures are plotted on the range -1000 to 300 [Pa] with isobar's every 50 [Pa].

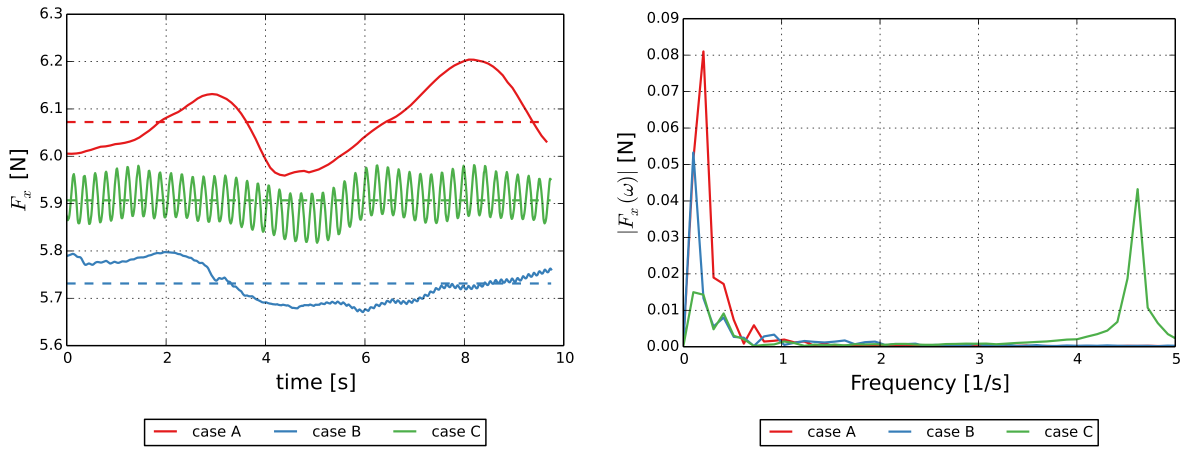

(a) Time trace x-direction (b) Frequency spectrum x-direction

Figure 3.25: Time step study: Time trace and frequency spectrum of the force in x-direction of the last 9.75 [s] ($1L$). The dashed line in the time trace indicates the mean value.

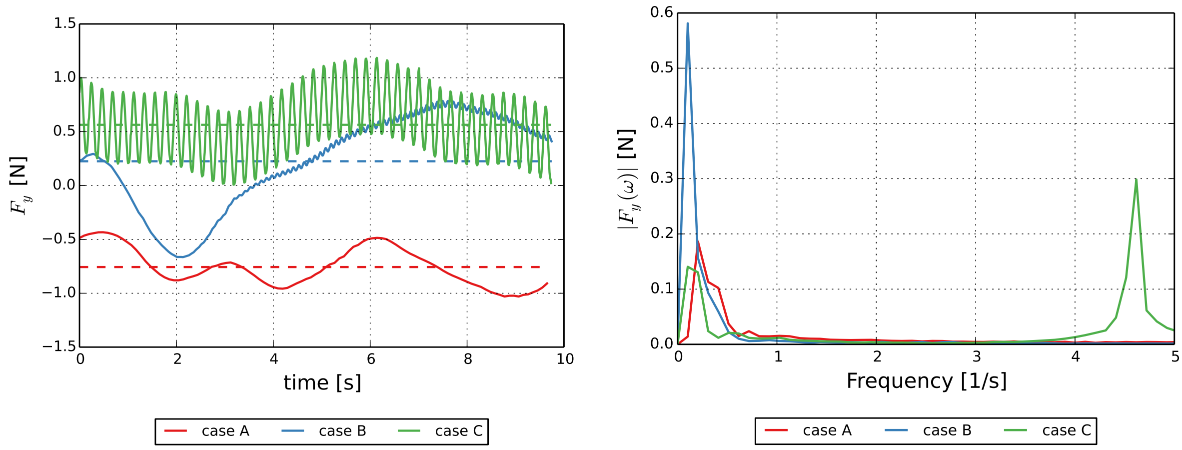

(a) Time trace y-direction (b) Frequency spectrum y-direction

Figure 3.26: Time step study: Time trace and frequency spectrum of the force in y-direction of the last 9.75 [s] ($1L$). The dashed line in the time trace indicates the mean value.

Table 3.12: Result of the time step study. The calculated mean μ and standard deviation σ are based on the time steps mentioned in the column time steps, starting at 1000 time steps[-]. The time is equal to 9.75 [s], which corresponds with $1L$.

		F_x		F_y	
Case	time steps [-]	μ [N]	σ [N]	μ [N]	σ [N]
A	100	6.07	0.071	-0.76	0.177
B	8101	5.73	0.040	0.23	0.434
C	886	5.91	0.039	0.56	0.281

presented case for acceptable cell Courant numbers, with reasonable computations time. It is suggested to keep the Courant number constant during a grid refinement study, as is done in [26].

3.3.4. Actuator disk study

In this small study the focus is on how to model the actuator disk properly to simulate a bow tunnel thruster. For this Numeca FineMarine has four options: uniform distribution, default distribution, own distribution and BEM coupling. It was decided to use the build-in distributions even though their are not designed for ducted propellers. The best approach would be to use the exact distribution of the propeller that Nienhuis tested during the model tests. A complete geometry of that propeller is not available. IHC has results of a stock propeller measured in a nozzle, it is used to compare the build-in distributions, but the distribution of the stock propeller with nozzle is not used in this study due to time constraints. As the aim of this research is to study the effect of the change of the tunnel cross-section, it is assumed that if for all cases the same actuator disk is used the results are comparable.

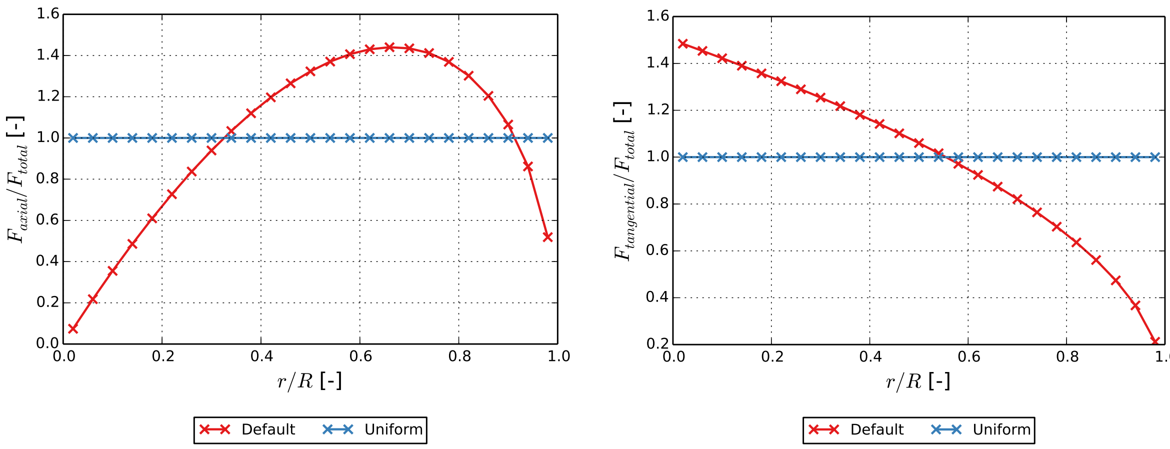

(a) Axial force distribution

(b) Tangential force distribution

Figure 3.27: Axial and tangential force distribution of the actuator disk along the radius of the disk used by Numeca FineMarine.

In Figure 3.27 the default and constant distributions are shown. For a ducted propeller it is known that the tip is more loaded compared to an unducted propeller [27] and even reaches its maximum at the tip. Numeca advises to not use the default distribution for a ducted propeller case and suggest to use the uniform distribution when simulating a water jet [15, 11-2].

For this study four actuator disk cases are simulated the names and variations are shown in Table 3.13. The settings for the computation are:

- actuator disk varied
- grid refinement ratio r=2
- free-surface: double body with mirror plane at waterline
- $y+$=30 [-], wall function

- time step based on Courant cell number Δt=0.011 [s]
- 4 non-linear iterations for 1000 [-] time steps, restart with 256 non-linear iterations 2000 [-] time steps
- ship speed u_s=0.318 [m/s], thrust T=10 [N]

Table 3.13: Names for the four actuator disk cases

Case	Distribution	Tangential forces
AD 1	uniform	none
AD 2	default	none
AD 3	uniform	0.139 [Nm]
AD 4	default	0.139 [Nm]

Qualitative

The effect of the tangential force is clearly visible in Figure 3.28. The flow converges after the actuator disk to a single core with high velocities, due to the induced rotation. This is visible in Figure 3.28c and 3.28d. For those two cases (AD 3 and AD 4) a large region with no velocity exists behind the jet. It seems that the tunnel jet flow bends later compared to the cases AD 1 and AD 2.

On the inlet side no visible effect of the actuator disk model on the hydrodynamic pressure is seen (Figure 3.29). For the outlet on the other hand there are effects visible (Figure 3.30). Both was noticed for the general flow pattern, the inlet side seems to be independent of the distribution of the actuator disk and tangential forces. This seems logical as the suction into the tunnel is largely dependent on the flow rate, which is assumed to be constant when keeping the thrust constant.

The qualitative comparison shows that tangential forces result in more rotation in the flow. When considering the flow through the tunnel for the wedge at zero speed an asymmetric jet is recognized for the cases were the tangential force is included. It should be considered that in reality always a tangential force is induced by a rotating propeller, therefore it is advised based on the qualitative comparison to include the tangential forces.

Quantitative

In Figure 3.31a the resistance in the x-direction is shown. First of all it can be seen that the two cases with tangential forces show more fluctuations. The default distribution is for both cases lower than the corresponding uniform distribution. This can also be seen when taking a look at the mean and standard deviation of the time trace in Table 3.14.

All four cases show oscillations that correspond to a frequency of roughly 4.2 [1/s] in the frequency spectrum in Figure 3.31b. Only case AD 3 shows not a peak around 4.2 [1/s] in the spectrum. The same peak was noticed in the time step study for Case C and the peak corresponds with period of about 0.24 [s]. Next to that for all four cases the first peak occurs at low frequencies which corresponds with a relative large period in the time trace. Which was noticed in the small studies before. Again these frequencies correspond with a period that is in the order of the measuring time.

Case AD 4 and AD 3 show multiple low frequency harmonics, while AD 1 and AD 2 show only one dominant low frequency peak. This is probably due to the added rotation in case AD 3 and AD 4, caused by the tangential forces. Next to that it can be seen that case AD 1 has relative low values throughout the complete spectrum, which is the explanation why the standard deviation for case AD 1 is the lowest.

It seems with the introduction of a tangential force in the actuator disk that more peaks are visible and with that the flow gets more complex.

For the force in y-direction in Figure 3.32a it is noticed that case AD 4 fluctuates significantly and reaches values between 1 and -3 [N]. The two cases with no tangential force fluctuate around 0 [N].

The values in Figure 3.32b in the frequency domain of the force in the y-direction are a factor five higher than the values in the x-direction. Which shows that the fluctuation in forces in the y-direction is significant higher than in the x-direction. The same trends compared to the x-direction are noticed.

Based on the presented theory and a small study it is concluded to use the uniform distribution with tangential forces enabled. First of all in reality propeller induce an axial and a tangential force, therefore

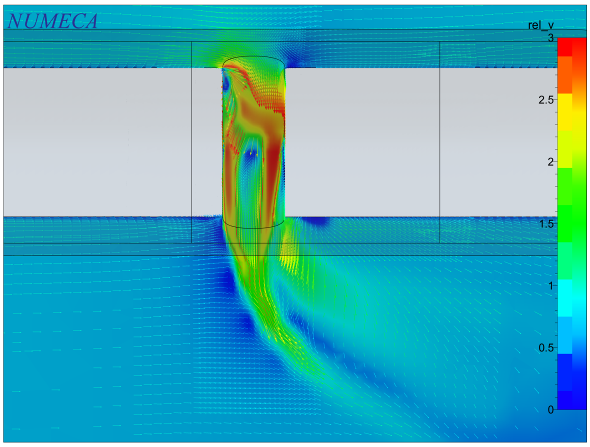

(a) Case AD 1

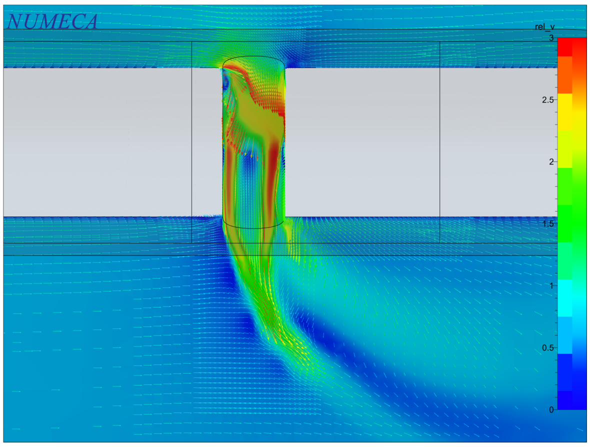

(b) Case AD 2

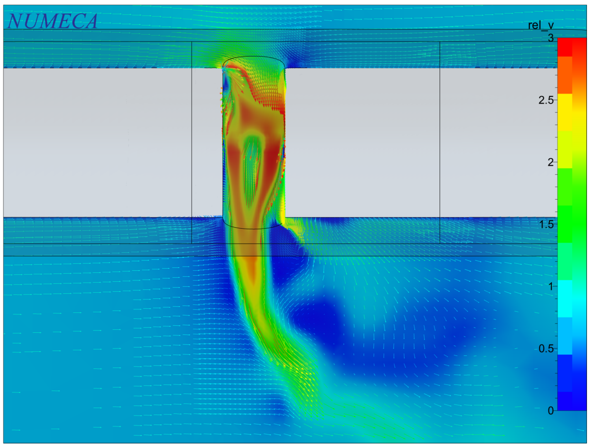

(c) Case AD 3

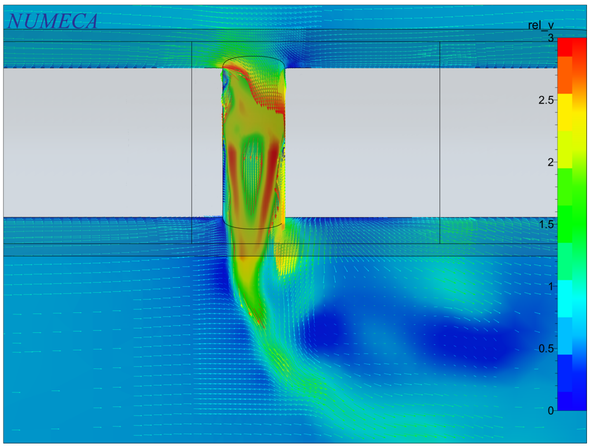

(d) Case AD 4

Figure 3.28: Relative velocity v_{rel} in the xy-plane at z=0.152 [m]. Topside of the wedge is inlet side and bottom the outlet side.

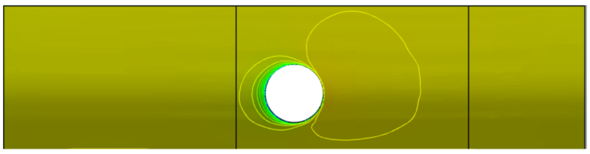

(a) Case AD 1

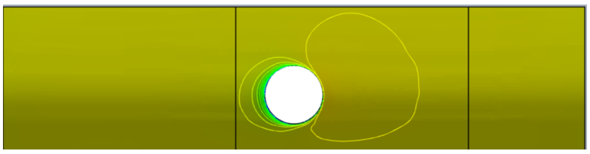

(b) Case AD 2

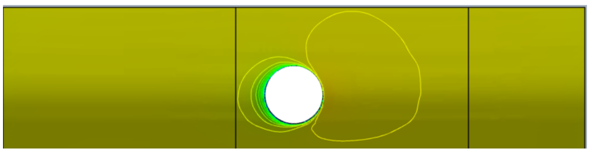

(c) Case AD 3

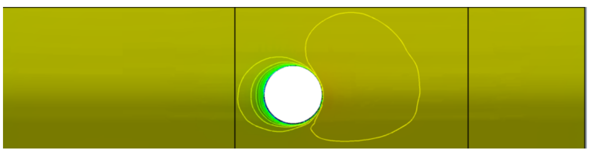

(d) Case AD 4

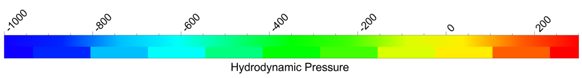

(e) Pressure scale

Figure 3.29: Hydrodynamic pressure of the inlet side plotted on the solids: front_midship, TT_side and aft_midship. Pressures are plotted on the range -1000 to 300 [Pa] with isobar's every 50 [Pa].

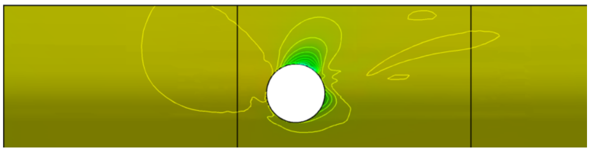

(a) Case AD 1

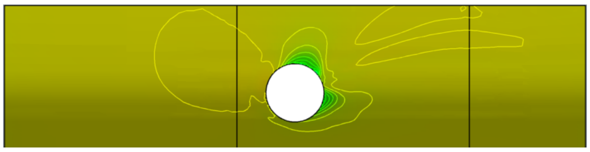

(b) Case AD 2

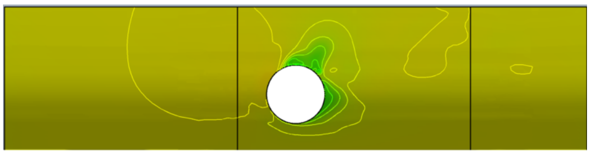

(c) Case AD 3

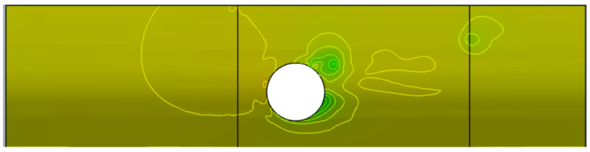

(d) Case AD 4

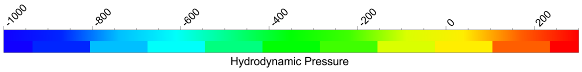

(e) Pressure scale

Figure 3.30: Hydrodynamic pressure of the outlet side plotted on the solids: front_midship, TT_side and aft_midship. Pressures are plotted on the range -1000 to 300 [Pa] with isobar's every 50 [Pa].

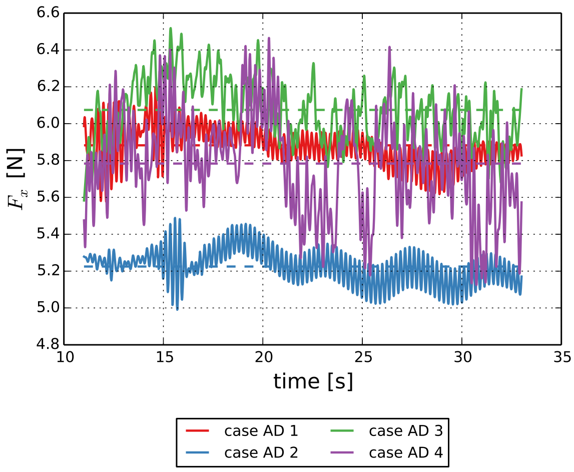

(a) Time trace x-direction

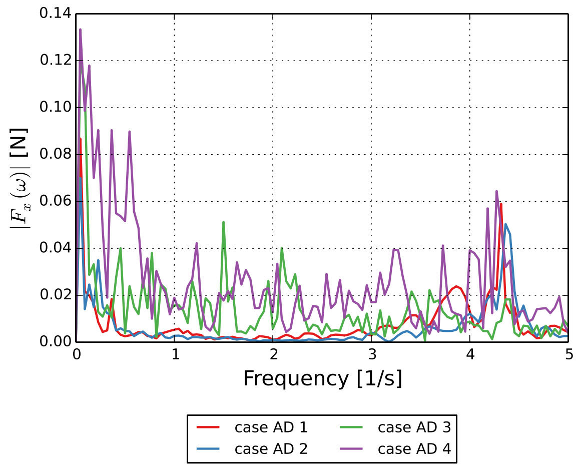

(b) Frequency spectrum x-direction

Figure 3.31: Actuator disk study: Time trace and frequency spectrum of the force in x-direction of the last 2000 [-] time steps after restart. The dashed line in the time trace indicates the mean value.

Table 3.14: Result of the actuator disk study. The calculated mean μ and standard deviation σ are based on 2000 [-] time steps.

	F_x		F_y	
Case	μ [N]	σ [N]	μ [N]	σ [N]
AD 1	5.88	0.10	-0.03	0.31
AD 2	5.23	0.09	-0.46	0.36
AD 3	6.08	0.16	-1.01	0.61
AD 4	5.78	0.26	-1.15	0.93

it's logical to include a tangential force. The downside was already noticed, the forces seem to fluctuate more as the flow gets more complex. The default distribution is not used, because the tip area is not loaded enough (compare Figure 3.27), the uniform distribution covers the tip loading better, but is to simple. It is advised to use an actual distribution of a ducted propeller. The effect of the distribution is assumed to be not dominant in the systematic variation of cross-sections, as the computation set-up will not be varied for different cross-sections.

3.3.5. First layer thickness study

Until now the viscous layers are calculated using a value of $y+$ of 30 [-]. The cells close to the wedge are then relative large and therefore a wall function is used to calculate the viscous stresses close to the wall. This is the common approach. It is however noticed that the viscous stresses and therefore the viscous forces in the tunnel are a major contributor to the overall forces especially in the y-direction. As an alternative the same grid has been created with viscous layers using a $y+$ of 1 [-] together with a no slip boundary condition. The resulting first cell width close to the wedge is decreased significantly and with this the number of grid cells is increased. The theory states that for a $y+$ of 1 [-] the wall functions can be omitted and the boundary layer can be solved within the created cells. The effect on the grid can be seen in Figure 3.33. The viscous layer inside the tunnel is calculated using the tunnel length as reference length and 3.0 [m/s] as reference velocity.

The settings for the computations are:

- $y+$=30 [-], wall function and $y+$=1 [-], no slip are compared
- grid refinement ratio r=2
- free-surface: double body with mirror plane at waterline
- actuator disk: constant distribution with tangential forces
- time step based on Courant cell number t=0.011 [s] and t=0.0088 [s]
- 4 non-linear iterations for 1000 [-] time steps, restart with 256 non-linear iterations
- ship speed u_s=0.318 [m/s], thrust T=10 [N], torque Q=0.139 [Nm]

For this comparison the Courant number is kept constant which resulted in two time steps Δt of 0.011 [s] for $y+$=30 and 0.0088 [s] for $y+$=1. An overview is given in Table 3.15. To get a better comparison between different computation the different phases of the computation are changed. An illustration versus the number of time steps can be seen in Figure 3.34. In Table 3.16 the settings of all phases are shown. Two computations are made. The first has the same settings for all grids. After the first computation (1000 [-] time steps) is finished a second computation is restarted after the first computation, with higher number of non-linear iterations n_{nl}. The number of time steps and the time step Δt is dependent on the grid, as the Courant number is kept constant. In all cases it is assured that the measuring section has a length of 1.5 L and is therefore equal to the time that the wedge needs to travel 1.5 L.

Table 3.15: The mesh, number of cells and time step for the two cases of the first layer thickness study.

Case	Mesh	Number of Cells [-]	time step [s]
$y+$=30 [-]	set-up 4	564196	0.011
$y+$=1 [-]	mesh a	1099699	0.0088

Table 3.16: The mesh, number of cells and time step for the two cases of the first layer thickness study.

Phase	Computation	n_{nl} [-]	time steps [-]	time step [s]
acceleration n_{nl}=4	1	4	500	0.1
stabilization n_{nl}=4	1	4	500	0.1
stabilization n_{nl}=256	2	256	200	grid dependent
measuring n_{nl}=256	2	256	until 1.5 L	grid dependent

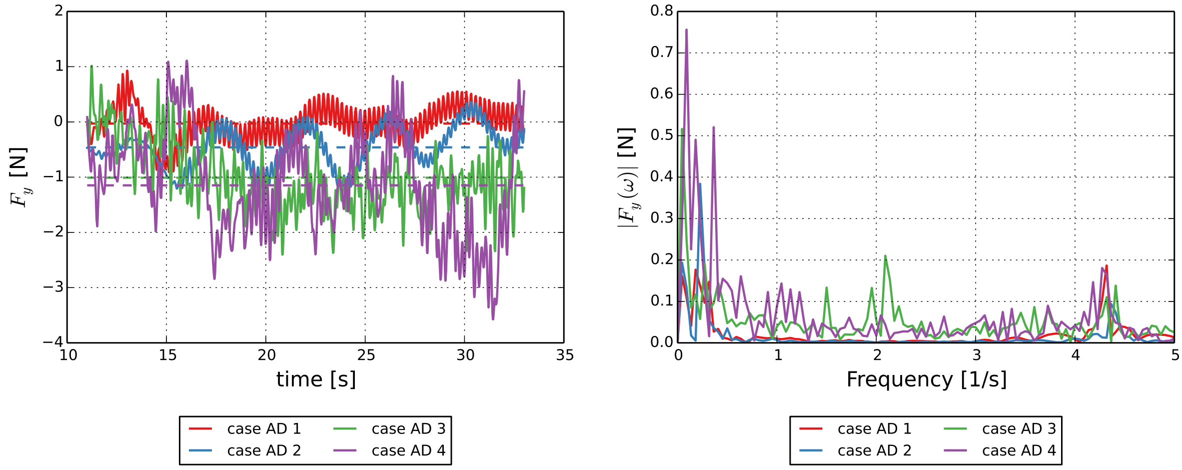

(a) Time trace y-direction (b) Frequency spectrum y-direction

Figure 3.32: Actuator disk study: Time trace and frequency spectrum of the force in y-direction of the last 2000 [-] time steps after restart. The dashed line in the time trace indicates the mean value.

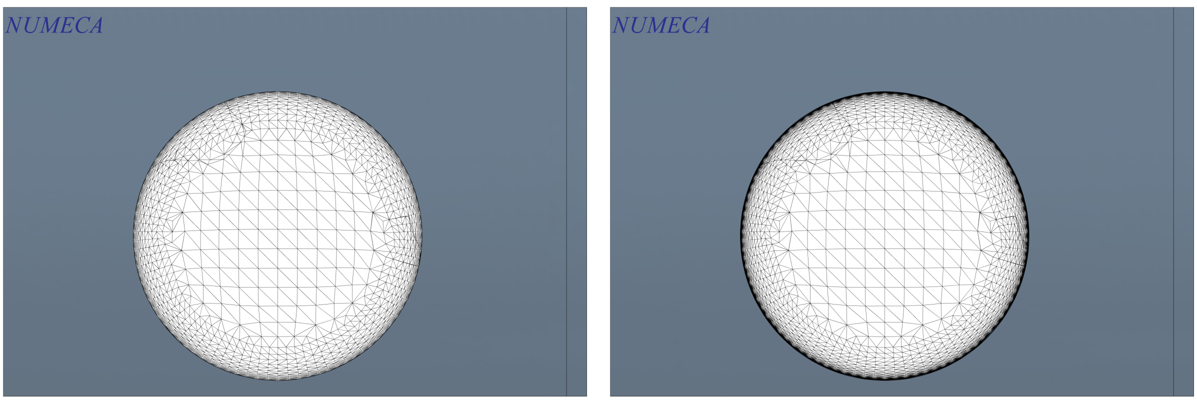

(a) y+=30 [-], mesh: set-up 4 (b) y+=1 [-], mesh: mesh A

Figure 3.33: Comparison of the grid inside the tunnel xz-plane cut at y=0 [m]

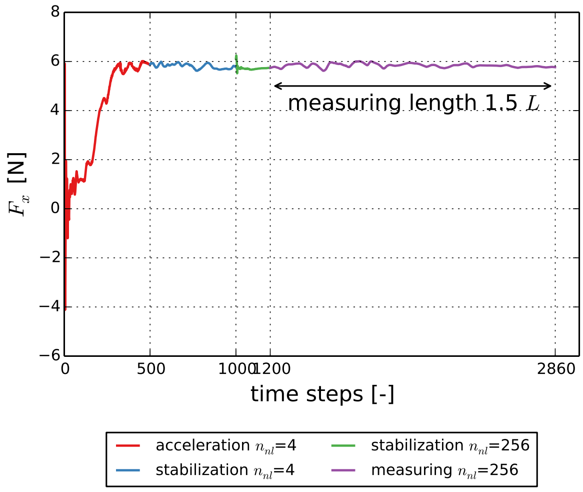

Figure 3.34: Overview of the different phases of the computation. The number of time steps used for the measuring phase are equal to the time that is needed for the wedge to travel 1.5 L. The illustration is based on the resistance in the ship direction F_x of case $y+$=1 [-].

Qualitative

In the direct comparison of the flow field of the two first layer thickness cases in Figure 3.35 it can be noticed that the flow for $y+$ =1 [-] is smoother compared to the $y+$ = 30 [-] case. This effect is independent on the used time step, as the same Courant number is used. It indicates that the flow along the tunnel wall is largely influenced by the viscous stresses. The no slip condition together with the small cells close to the tunnel wall seem to result in a 'stronger', more dense jet. The jet structures is maintained longer and can be recognized further away from the wedge. Next to that the flow at the inlet side is identical in both cases. The wake region behind the jet is more or less attached to the jet for $y+$ =1 [-], for the other case, however, the wake region is better visible at some distance away from the wedge.

In Figure 3.36 the hydrodynamic pressure at the inlet side, show nearly the same pattern. No big differences are noticed.

In Figure 3.37 on the outlet side a clear effect is visible. As mentioned before that is due to the change in flow inside the tunnel by the difference in solving the viscous layers.

The qualitative comparison shows that a clear effect on the flow is visible when changing the first layer thickness. This suggest to use more computation effort and use $y+$ =1 [-] with a no-slip condition. It should be remembered that for the $y+$ =30 [-] case wall functions are used, that are developed for the viscous layer around a ship. The flow in the tunnel differs largely from that flow.

Quantitative

The time trace of the resistance shown in Figure 3.38a shows that the $y+$ =1 [-] case has less fluctuation. In general the trace looks smoother. This is confirmed by the frequency spectrum in Figure 3.38b. The $y+$ =1 [-] case has some low frequency peaks and no peaks besides that. The $y+$ =30 [-] case on the other hand has multiple peaks in the shown frequency range of 0 to 5 [1/s]. This behavior corresponds with the observed velocity flow (Compare Figure 3.35).

Figure 3.39a indicates that the $y+$ =1 [-] case is fluctuating around 1 [N] for 0 to 4 [s] and after that it is fluctuating around 0.2 [N]. This indicates that the result is very sensitive to the selected time averaging method. The $y+$ =30 [-] case has a complete other order of magnitude and is oscillating significantly.

The frequency spectrum (Figure 3.39b) shows the same trend with respect to different dominant frequency peaks. The mean and standard deviation of the time traces are reported in Table 3.17.

The study on the first layer thickness shows that the result differ significantly between the two cases. It is concluded that a $y+$ =30 [-] with wall function is a simplification that results in different results. It is recommended to use $y+$ =1 [-] with no-slip conditions and except the increase in computation time.

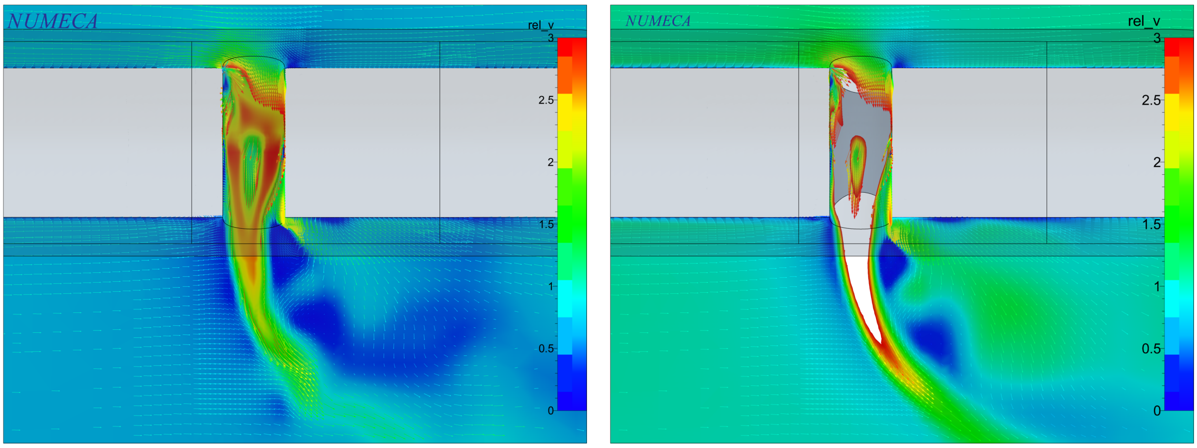

(a) $y+$=30 [-] (b) $y+$=1 [-]

Figure 3.35: Relative velocity v_{rel} in the xy-plane at z=0.152 [m]. Topside of the wedge is inlet side and bottom the outlet side.

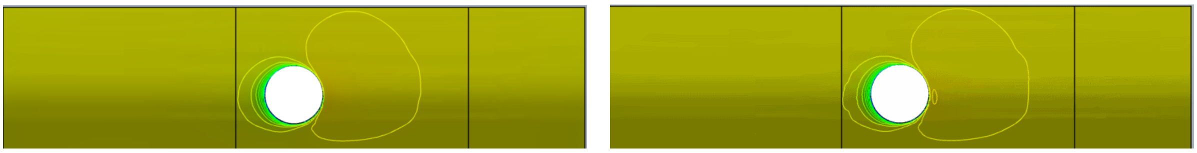

(a) $y+$=30 [-] (b) $y+$=1 [-]

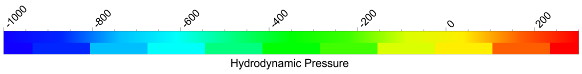

(c) Pressure scale

Figure 3.36: Hydrodynamic pressure of the inlet side plotted on the solids: front_midship, TT_side and aft_midship. Pressures are plotted on the range -1000 to 300 [Pa] with isobar's every 50 [Pa].

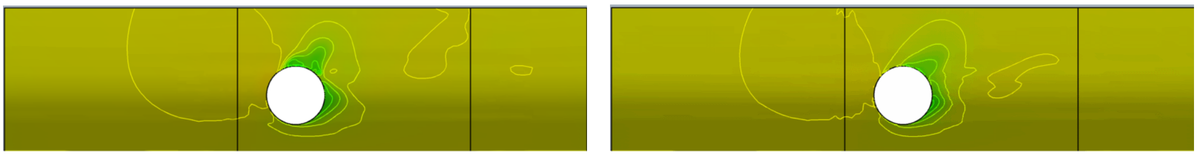

(a) $y+$=30 [-] (b) $y+$=1 [-]

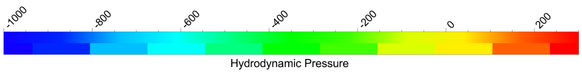

(c) Pressure scale

Figure 3.37: Hydrodynamic pressure of the outlet side plotted on the solids: front_midship, TT_side and aft_midship. Pressures are plotted on the range -1000 to 300 [Pa] with isobar's every 50 [Pa].

Table 3.17: Data of the first layer thickness study. The calculated mean μ and standard deviation σ are based on the mentioned time steps.

		F_x		F_y	
Case	time steps [-]	μ [N]	σ [N]	μ [N]	σ [N]
$y+$ =30 [-]	1100	6.01	0.125	-1.26	0.40
$y+$ =1 [-]	1375	5.84	0.073	0.52	0.41

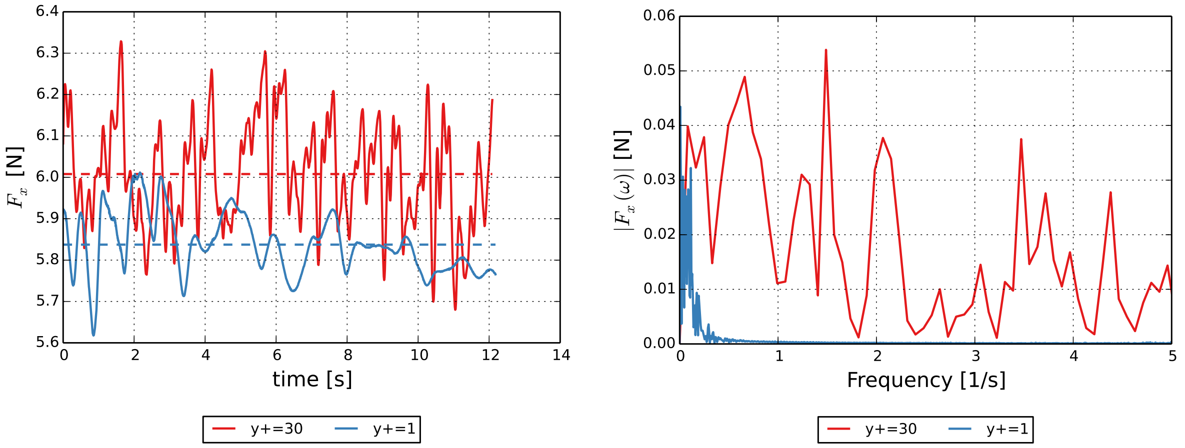

(a) Time trace x-direction

(b) Frequency spectrum x-direction

Figure 3.38: First layer thickness study: Time trace and frequency spectrum of the force in x-direction of the measuring section. The dashed line in the time trace indicates the mean value.

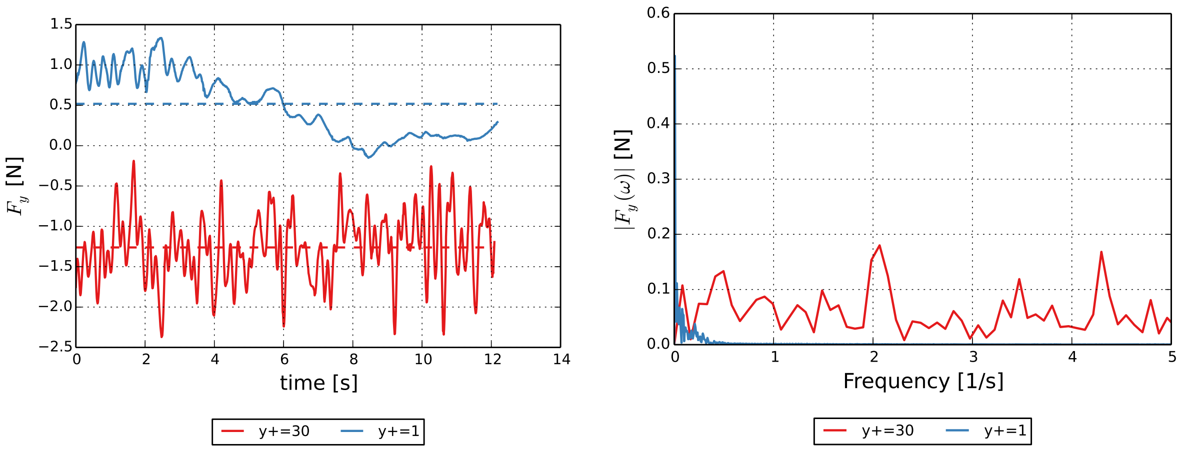

(a) Time trace y-direction

(b) Frequency spectrum y-direction

Figure 3.39: First layer thickness study: Time trace and frequency spectrum of the force in y-direction of the measuring section. The dashed line in the time trace indicates the mean value.

3.4. Verification & Validation

In this section a verification and validation study is performed for the Nienhuis wedge. First a grid study is made for two cases: the base and a zero speed case. For the base case the wedge is moving with the velocity u_s of 0.318 [m/s] and a thrust T of 10 [N] is applied, for the zero speed case (u_s=0 [m/s]) the wedge is at rest at a thrust of 10 [N] is applied. After the grid study the thrust and wedge velocity are varied. At the end of this section different verification and validation studies are presented.

3.4.1. Grid study

A grid study is performed to quantify the discretization uncertainty. The method of Eça and Hoekstra [17] is used, which is explained in Chapter 2 and in Appendix B. The following settings are used, based on the results form the base case studies:

- grid refinement ratio r is varied
- y+=1 [-], no slip
- free-surface: double body with mirror plane at waterline
- actuator disk: constant distribution with tangential forces
- time step based on Courant cell number t depends on grid
- 4 non-linear iterations for 1000 [-] time steps, restart with 256 non-linear iterations until vessel has moved 1.5L
- ship speed u_s=0.0 and 0.318 [m/s], thrust T=10 [N], torque Q=0.139 [Nm]

It is chosen to vary the initial cell size systematically and therefore controlling a systematic grid refinement. The number of initial cells are calculated as:

$$x_{initial} = 15r \ , \ y_{initial} = z_{inital} = 9r \tag{3.7}$$

Where the factor r is an integer value that is varied to obtain different grids. In Table 3.18 an overview of the different initial grids is shown. Figure 3.40 shows the different grids used in the grid study. The different refinement boxes shown in Table 3.3 are visible.

Mesh a to f are used for the base case and mesh a to d for the zero speed case. In the following the main results are discussed in a qualitative and a quantitative way.

Table 3.18: Number of initial cells used and definition of the grids for the grid study

		Number of initial cells			Size of initial cells				
Mesh	r	$x_{initial}$	$y_{initial}$	$z_{initial}$	Δx	Δy	Δz	Number of Cells	time step [s]
mesh a	2	30	18	18	1/2 L	1/2 L	1/2 L	1099699	0.0088
mesh b	1	15	9	9	1 L	1 L	1 L	444769	0.0119
mesh c	3	45	27	27	1/3 L	1/3 L	1/3 L	1967995	0.0073
mesh d	4	60	36	36	1/4 L	1/4 L	1/4 L	3242320	0.0061
mesh e	5	75	45	45	1/5 L	1/5 L	1/5 L	4902549	0.0053
mesh f	6	90	54	54	1/6 L	1/6 L	1/6 L	6998258	0.0048

Qualitative

First the velocities of the flow for the base case are analyzed. The Courant number has been kept constant for the different grids, which results in smaller time steps. In Figure 3.41 the effect of smaller time steps is visible. With an increase in cells the flow is better captured in the refinement boxes and more local effects are visible. The inflow side on top of the pictures are similar for all six grids (compare Figure 3.41, however in the tunnel with an increase in grid cells the flow gets more chaotic. As the tunnel jet flow is different for all six cases differences in the obtained forces are expected.

The zero speed case is only computed for mesh a to d. The velocity flow in Figure 3.42 shows that higher velocities exist in the jet at the left side in comparison to the right side. This is caused by the rotation of the tangential force that is included in the actuator disk. Furthermore it can be seen that the

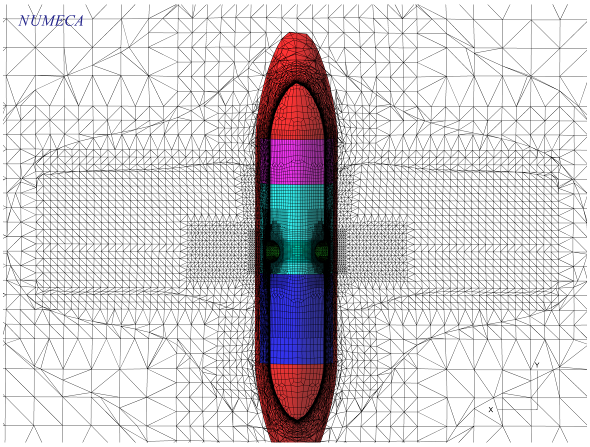

(a) mesh b

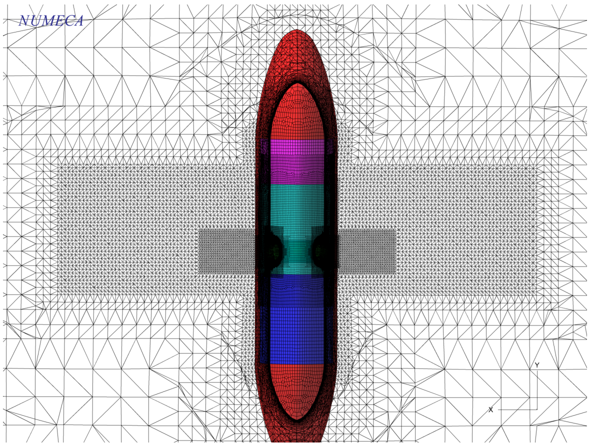

(b) mesh a

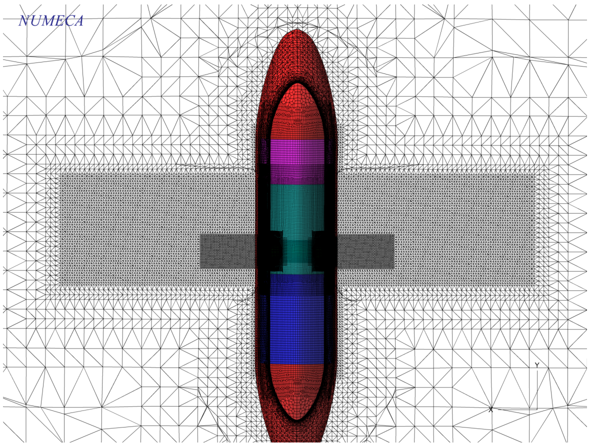

(c) mesh c

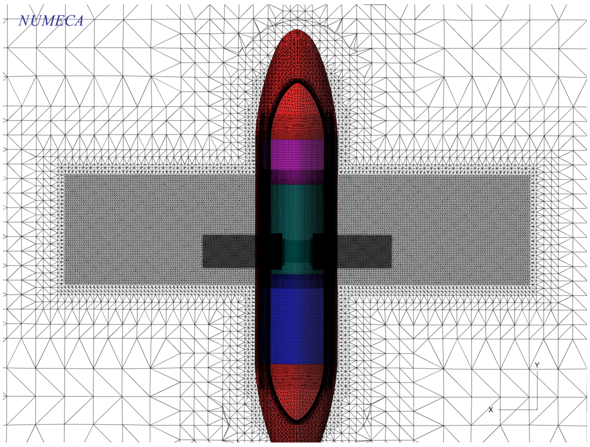

(d) mesh d

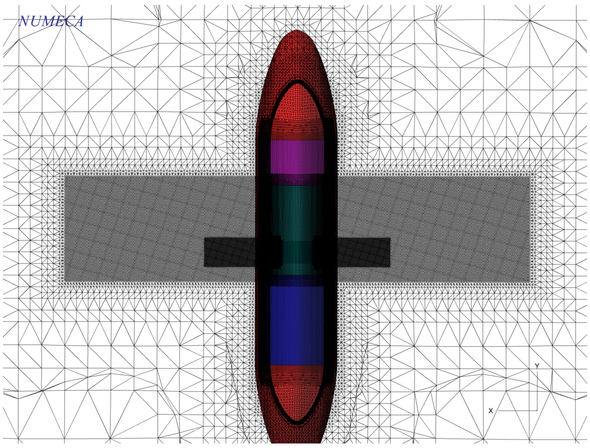

(e) mesh e

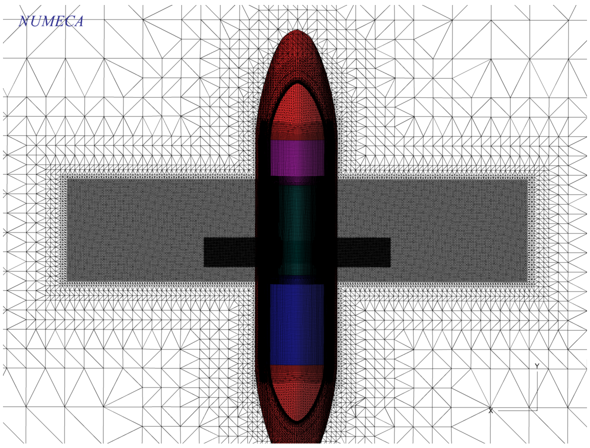

(f) mesh f

Figure 3.40: Comparison of the six different meshes used for the grid study of the Nienhuis wedge. Mesh at z=0.159 [m] in the xy-plane.

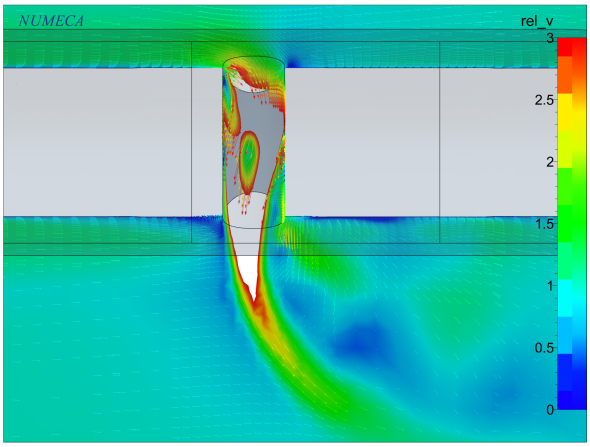

(a) mesh b

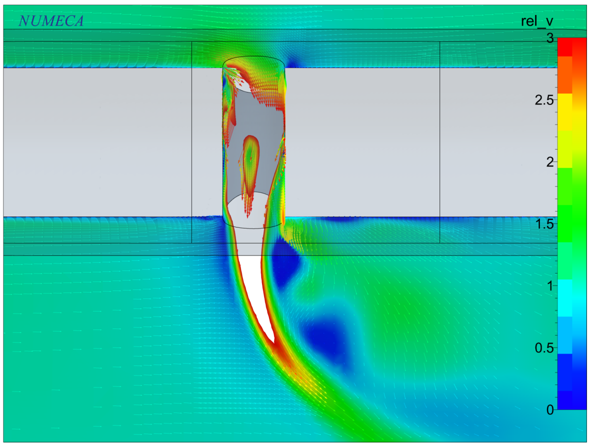

(b) mesh a

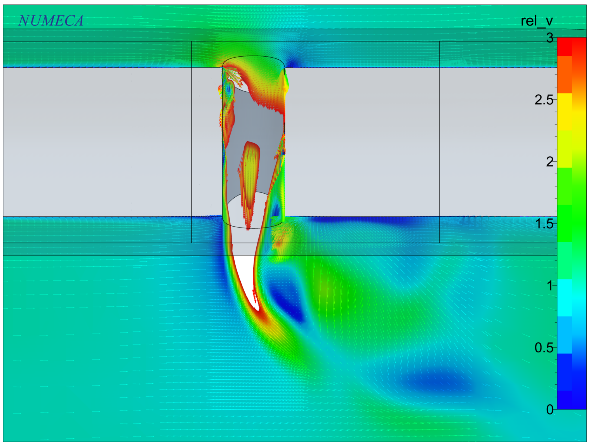

(c) mesh c

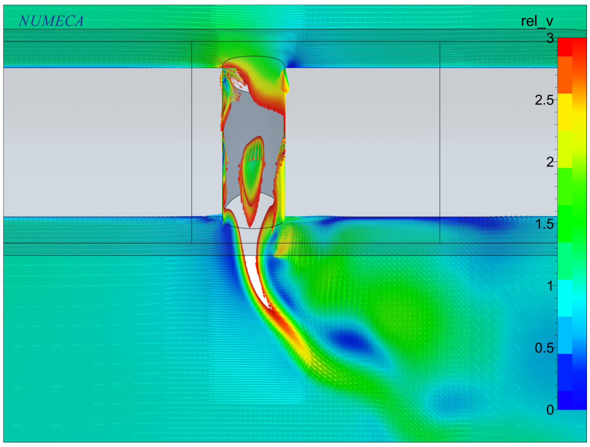

(d) mesh d

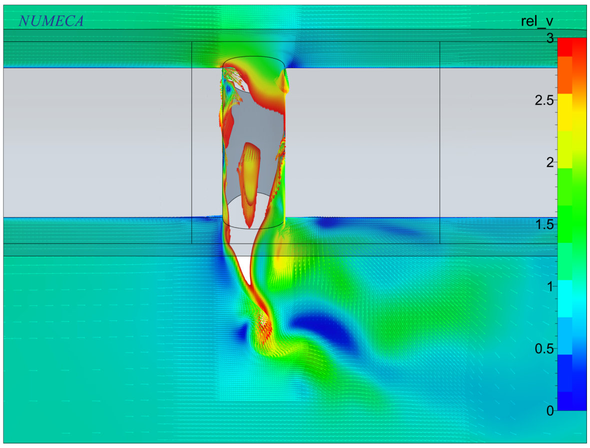

(e) mesh e

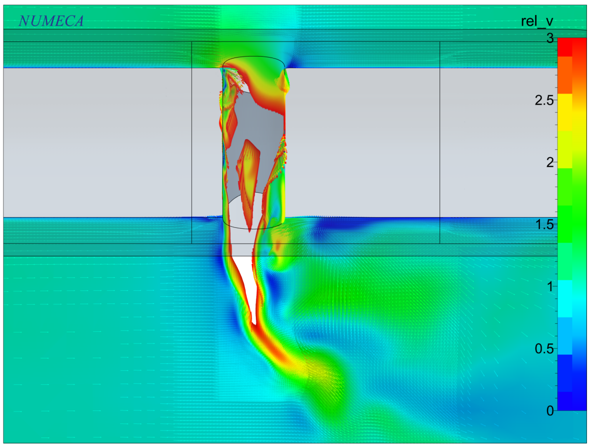

(f) mesh f

Figure 3.41: Grid study: base case. Relative velocity v_{rel} in the xy-plane at z=0.152 [m]. Topside of the wedge is inlet side and bottom the outlet side.

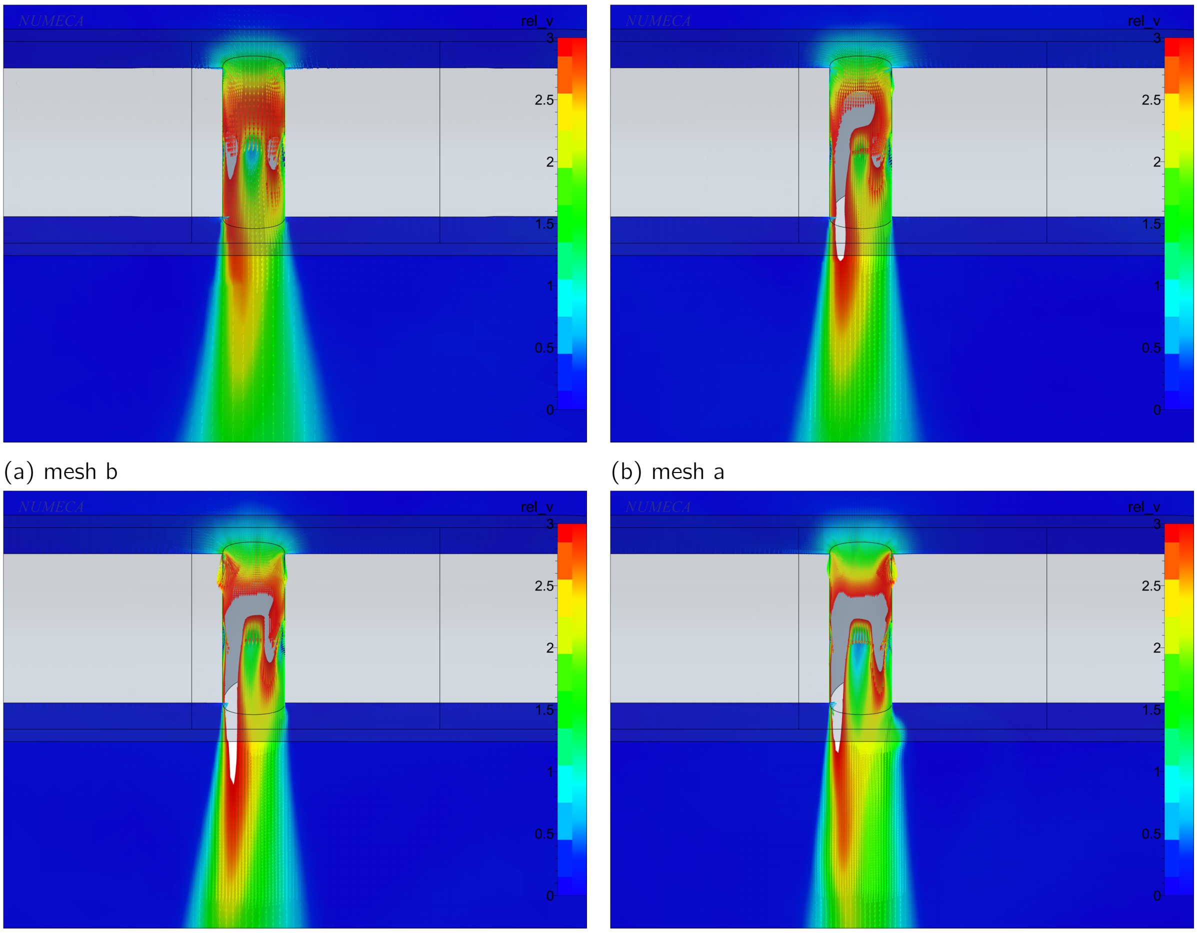

(a) mesh b

(b) mesh a

(c) mesh c

(d) mesh d

Figure 3.42: Grid study: zero speed case. Relative velocity v_{rel} in the xy-plane at z=0.152 [m]. Topside of the wedge is inlet side and bottom the outlet side.

spreading of the jet in the y-direction seems to decrease with an increase in grid cells. As for the base case it is noticed that with an increase in grid cells more local effects are visible.

From the qualitative comparison it is concluded that an increase in grid size shows more local flow phenomena. As the flow field differs between the cases it is expected that this is also visible in the quantitative comparison.

Quantitative

In this section a quantitative comparison of the results of the grid study is given. First for the base case and after that for the zero speed case.

Base case The time trace of the base case in x-direction is shown in Figure 3.43a. Besides mesh b and mesh d, the meshes fluctuate between 5.5 and 6.0 [N]. The decrease in time step for an increase in grid cells is visible. As mesh b is the coarses grid it is expected that it can show a different behavior than the other meshes. For the difference in behavior for mesh d, compared to the other meshes, no explanation can be given.

The frequency spectrum show a significant peak for mesh e at around 0.12 [1/s] in Figure 3.43b. Mesh d also has a significant peak at around 0.02 [1/s]. For the other meshes a lot of small peaks exists, but no clear peaks can be identified. This frequency spectrum, however, shows that the meshes show different behavior, as other fluctuations and interactions are presented. This is inline with the observation of the qualitative comparison.

The time trace for the force in the direction of the tunnel in Figure 3.44a shows significant fluctuations. These fluctuations are in line with observations of animated simulations of the cases, which indicate a largely unsteady flow. The results of these high fluctuations is that the mean is very sensitive to the chosen measuring range and ranges between -0.3 and 1.2 [N]. Furthermore mesh f and mesh e show the highest fluctuations.

In Figure 3.44b the frequency spectrum of the force in y-direction is shown. The scale of the y-axis should be noticed which gives for all meshes at least a amplitude of 0.3 [N]. All meshes have a first harmonic at a very low frequency, between 0.001 and 0.02 [1/s]. In general the spectrum shows a lot of noise, which corresponds with the time trace.

The number of cells and the means of the force in x- and y-direction are used as input for the method of Eça and Hoekstra [17]. The obtained results are plotted against the mean cell size h_i. The mean cell size has been divided by the mean cell size of mesh a h_a. At h_i/h_a=0 the extrapolated result, independent of the grid size, is shown. The presented errorbars show the 95 [%] uncertainty interval U_i for each mesh.

For the force in x-direction in Figure 3.45a a decay is seen, however the uncertainties are high and in the range of 40 to 85 [%]. The numerical results are shown in Table 3.19. Where the mean force of the time trace is used as ϕ_i. The method predicts the value, independent of a grid, as 5.41 [N], the best fit has a standard deviation of 0.34 [N].

Table 3.19: Grid study base case for the forces in x-direction.

Mesh	Cells [-]	$\mu = \phi_i$ [N]	U_i [N]	U_i/ϕ_i [%]
Independent	∞	5.41		
mesh f	6998258	5.77	2.41	41.8
mesh e	4902549	5.90	2.85	48.3
mesh d	3242320	5.25	3.63	69.1
mesh c	1967995	5.60	3.18	56.8
mesh a	1099699	5.84	3.62	62.0
mesh b	444769	6.70	5.61	83.7

The grid study for the force in y-direction gives very large uncertainties. First of all the values for the force in y-direction are small and based on this the best fit, with a standard deviation σ of 0.28 [N] results in a prediction ϕ_0 of -3.3 [N]. As the uncertainties are based on a safety factor (3 in this case) and the error between the value of the grid (ϕ_i) and the prediction ϕ_0 results in large uncertainties. When these

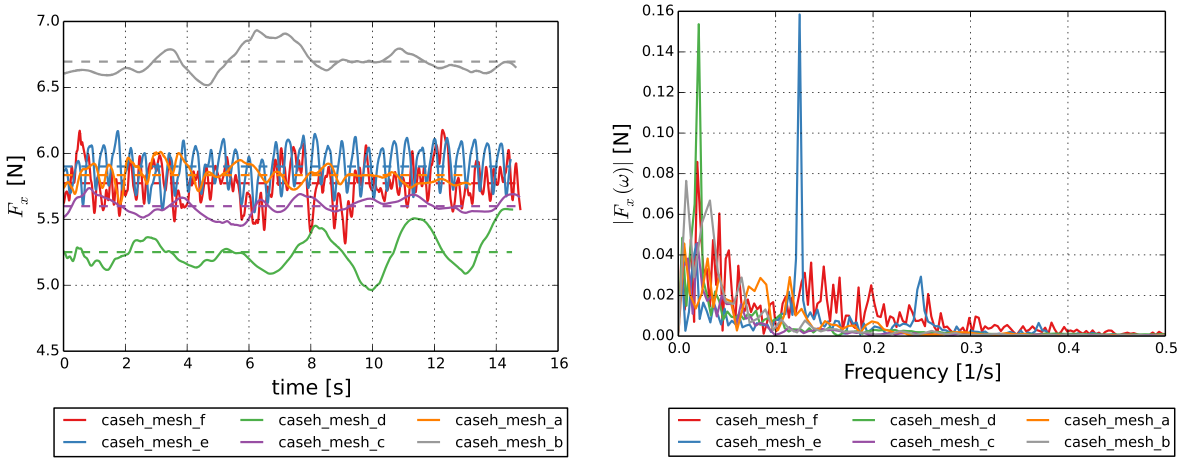

(a) Time trace x-direction

(b) Frequency spectrum x-direction

Figure 3.43: Grid study base case: Time trace and frequency spectrum of the force in x-direction of the measuring section. The dashed line in the time trace indicates the mean value.

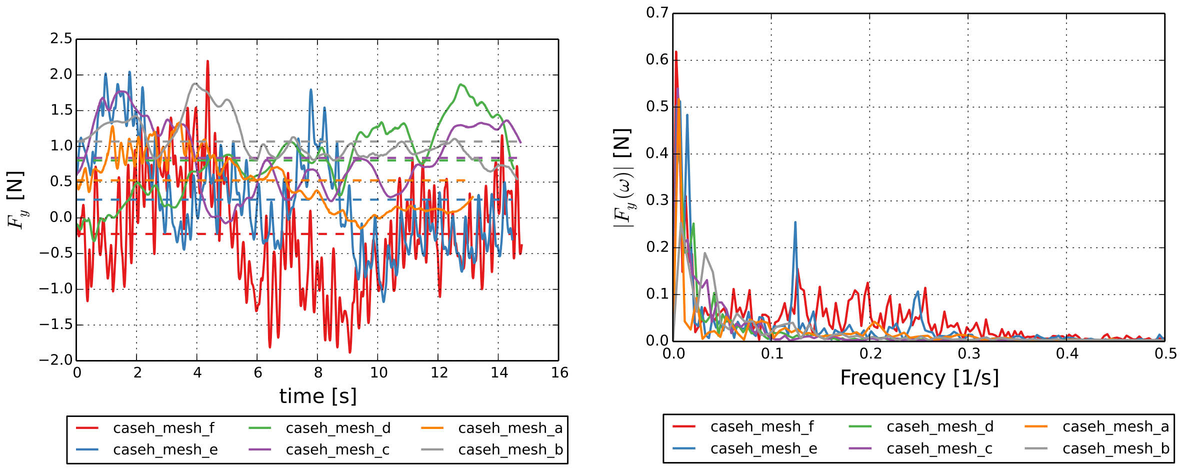

(a) Time trace y-direction

(b) Frequency spectrum y-direction

Figure 3.44: Grid study base case: Time trace and frequency spectrum of the force in y-direction of the measuring section. The dashed line in the time trace indicates the mean value.

uncertainties are presented as percentages of the value of the grid, the percentages are between 1400 and 5200 [%]. Both can be seen in Figure 3.45b and in Table 3.20.

Table 3.20: Grid study base case for the forces in y-direction.

Mesh	Cells [-]	$\mu = \phi_i$ [N]	U_i [N]	U_i/ϕ_i [%]
Independent	∞	-3.27		
mesh f	6998258	-0.23	12.0	5200
mesh e	4902549	0.25	12.4	5000
mesh d	3242320	0.80	14.2	1800
mesh c	1967995	0.84	14.4	1700
mesh a	1099699	0.74	16.2	2200
mesh b	444769	1.07	15.1	1400

The grid study of the forces of the base case show large uncertainties. This was already noticed during the base case studies, it is very hard to get close results. It should be realized that the measured values are very small and an absolute variation of 1.5 [N] would be perfectly fine if the values had much higher magnitude. However the measured values are in the range of a few newtons, and therefore relative uncertainties are very high. As the discretization error for this case are high, it is suitable to assume that the round-off errors ϵ_{round} and iteration errors $\epsilon_{iteration}$ are small enough to be neglected (Compare Chapter 2). It must be concluded that the discretization error is the dominant error in this study and is to high, especially for the y-direction.

Before the zero speed case is analyzed the pressure profile depending on the different grids is shown. In Figure 3.46 points at the center location (z=0.159 [m]) along the hull of the wedge are defined and the pressure for each case is measured at those points. For all 56 points on both sides grid studies have been performed. The plotted errorbars are the uncertainties of mesh a from each grid study.

For the inlet side in Figure 3.46a it can be seen that all meshes show similar pressures. The uncertainty increases from the bow towards the tunnel, and the uncertainties at the edge of the tunnel are the largest. Behind the tunnel a high pressure region is noticed, which is smaller than the low pressure region before the tunnel. At the high pressure region the uncertainties seem to increase slightly as moving backwards.

At the outlet side in Figure 3.46b the pressures before the tunnel are similar for the different grids and result in low uncertainties. Close to the tunnel the pressures diverge for different grids, resulting in large uncertainties. Behind the tunnel the differences in measured pressures are clearly visible, resulting in large uncertainties. However the trend is the same for all grids.

Zero speed case A second grid study is made for the zero speed case. The wedge is has zero speed (v_s=0 [m/s]) and the thrust is T=10 [N]. When looking at the time trace shown in Figure 3.47a it can be seen that the values are very small, which is expected, as the resistance of the wedge should be zero when the wedge has zero speed. Mesh b shows a strange behavior, next to that the values of mesh a seem to increase during the complete measuring section.

The frequency spectrum in Figure 3.47b shows a first harmonic at low frequencies and for mesh c and d multiple peaks are recognized around 0.1 [1/s], the other two meshes do not show this behavior, which means that these oscillations only occur at smaller time and spatial discretization.

The time trace in the direction of the tunnel in Figure 3.48a shows some interesting things. First mesh b shows again an odd behavior, secondly the values of mesh a are increasing during the entire measuring time. Mesh a, c and d fluctuate around -1 [N], which is 10 [%] of the applied thrust. The theoretical maximum for this value is 50 [%] ([3]).

The frequency spectrum in Figure 3.48b is comparable to the one in the x-direction. The first harmonic of mesh b is however significantly higher.

The result from the grid study for the four meshes is shown in Figure 3.49. The values in the x-direction show no clear convergence. The resulting independent grid solution is 0.39 [N], while a value of 0 [N] is expected. In Table 3.21 The relative uncertainties are very large, as the force values are small.

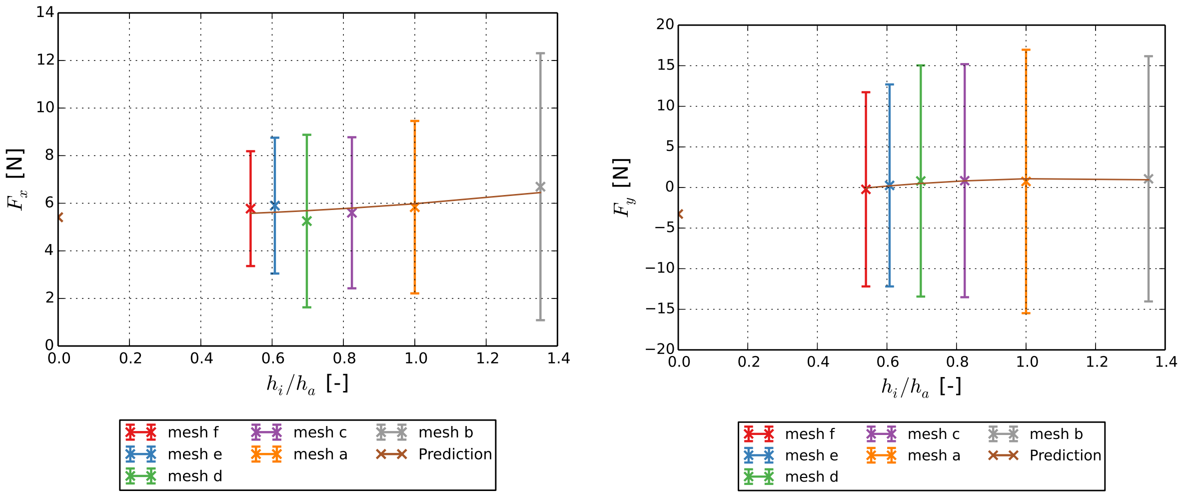

(a) Forces in the x-direction (b) Forces in the y-direction

Figure 3.45: Results of the grid study using the method of Eça and Hoekstra [17] for the force in x and y-direction for the base case. The errorbars indicate a 95[%] uncertainty interval, the prediction line is the best fit regression of the method.

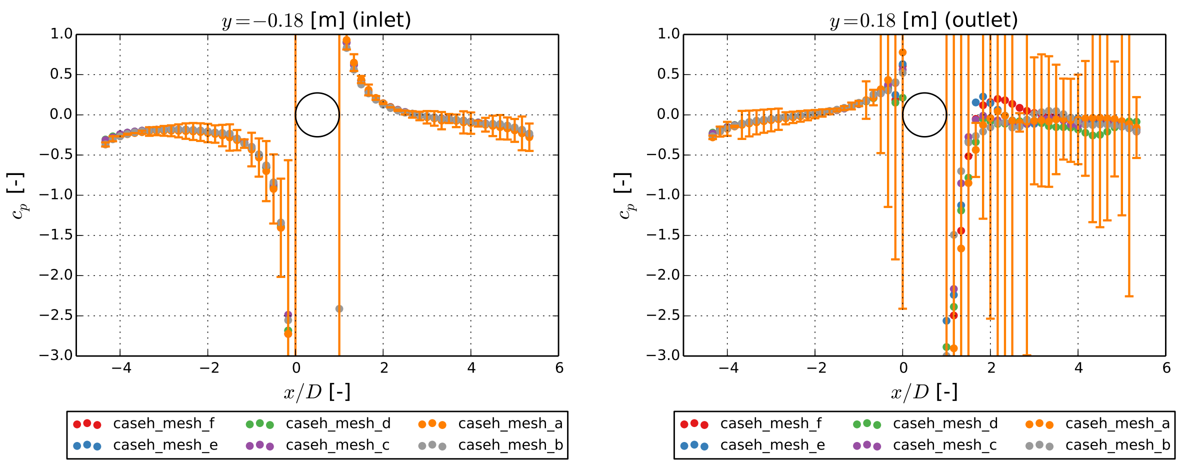

(a) Inlet (b) Outlet

Figure 3.46: Grid study: base case. Pressure profile for the in- and outlet side of the bow thruster tunnel. The uncertainties are calculated using the the method of Eça and Hoekstra [17] and are shown for mesh a.

Table 3.21: Grid study rest case for the forces in x-direction.

Mesh	Cells [-]	$\mu = \phi_i$ [N]	U_i [N]	U_i/ϕ_i [%]
Independent	∞	0.39		
mesh d	3242320	-0.01	1.3	13000
mesh c	1967995	0.48	1.4	290
mesh a	1099699	0.04	1.4	3500
mesh b	444769	-0.33	0.9	270

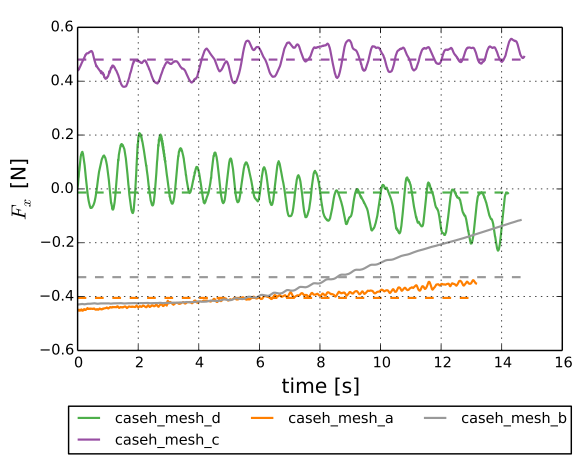

(a) Time trace x-direction

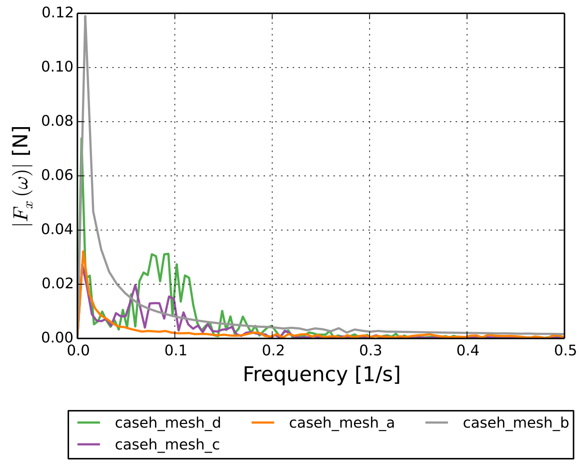

(b) Frequency spectrum x-direction

Figure 3.47: Grid study zero speed case: Time trace and frequency spectrum of the force in x-direction of the measuring section. The dashed line in the time trace indicates the mean value.

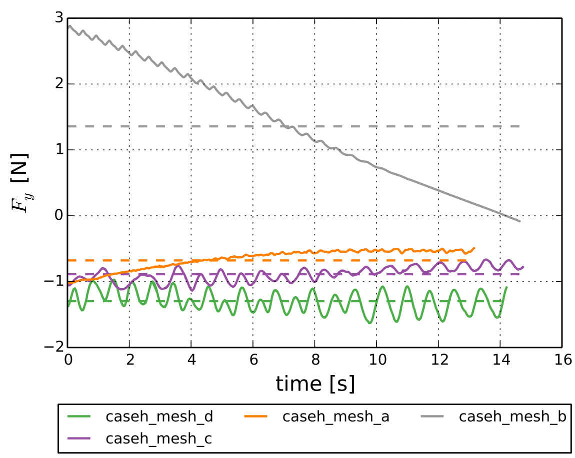

(a) Time trace y-direction

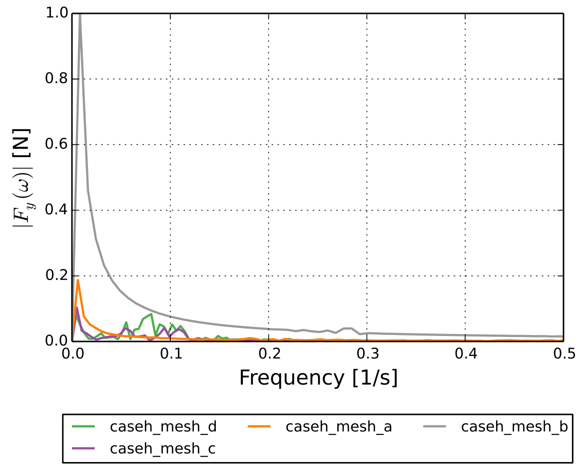

(b) Frequency spectrum y-direction

Figure 3.48: Grid study zero speed case: Time trace and frequency spectrum of the force in y-direction of the measuring section. The dashed line in the time trace indicates the mean value.

For the y-direction a nice convergences can be seen in Figure 3.49b. The independent grid solution becomes -2.29 [N] for this case. It should be noticed that the sign of the force is changed for mesh b compared to the other meshes (Table 3.22). The relative uncertainties are again very high. This means that a large numerical uncertainty is present in the results.

Table 3.22: Grid study rest case for the forces in y-direction.

Mesh	Cells [-]	$\mu = \phi_i$ [N]	U_i [N]	U_i/ϕ_i [%]
Independent	∞	-2.29		
mesh d	3242320	-1.30	3.1	240
mesh c	1967995	-0.89	4.2	470
mesh a	1099699	-0.68	6.3	920
mesh b	444769	1.36	10.9	800

3.4.2. Speed and thrust variation

In this section the Nienhuis wedge is tested for different ship speeds and thrusts using mesh a. The following settings were derived during the previous sections and are used for the speed and thrust variation:

- ship speed and thrust varied
- grid refinement ratio r=2 (mesh a)
- $y+$=1 [-], no slip
- free-surface: double body with mirror plane at waterline
- actuator disk: constant distribution with tangential forces
- time step based on Courant cell number t depends on grid
- 4 non-linear iterations for 1000 [-] time steps, restart with 256 non-linear iterations until vessel has moved 1.5 L

In Table 3.23 the different testing situations are explained. The values for the ship speed u_s, the thrust T and applied torque Q are presented. These values are based on Nienhuis [1]. In the following the velocity

Table 3.23: Definition of the testing situations for the speed and thrust variation.

Situation	u_s [m/s]	T [N]	Q [Nm]
1	0	5	0.0695
2	0	10	0.139
3	0	30	0.417
4	0.159	0	0
5	0.159	5	0.0695
6	0.159	10	0.139
7	0.159	30	0.417
8	0.318	0	0
9	0.318	5	0.0695
10	0.318	10	0.139
11	0.318	30	0.417
12	0.478	0	0
13	0.478	5	0.0695
14	0.478	10	0.139
15	0.478	30	0.417

ratio m is used to describe the behavior of the flow. In literature a dependency of the force in the tunnel direction F_y with the velocity ratio m is often found, for example in [1], [22] and [24]. On the other hand Karlikov & Sholomovich [4] state that the ratio gives a good indication for the type of flow, but has no clear effect on the force in the tunnel direction. The ratio m and it's standard deviation $\sigma(m)$ is defined as the ratio between the ship speed u_s and the tunnel jet speed v_j as:

$$m = \frac{u_s}{v_j} \quad \sigma(m) = m\frac{\sigma(v_j)}{v_j} \tag{3.8}$$

The ship velocity is known and it is assumed that the standard deviation of the ship velocity is zero. The tunnel jet speed v_j needs to be obtained from the results of the computations. For this multiple longitudinal cutting planes through the tunnel are defined. On each of this planes the velocities are integrated for all three directions x, y and z. To get the mean tunnel jet speed the resulting value from the integral is multiplied with the area of the cutting plane, which is by definition the cross-sectional area A of the tunnel.

Using this approach leads to a velocity distribution along the tunnel axis. In Figure 3.50 these velocity distribution is given for Situation 10. In Figure 3.50a it can be seen that the velocity in the z-direction is at the inlet side (left side of the figure) positive, is decelerated and becomes negative. This behavior can be explained with the geometry of the tunnel itself. As the tunnel is longer at the top in comparison to the bottom. This form has a large influence on the flow inside the tunnel, as can be seen in Figure 3.51.

The velocities in the x- and y-direction in Figure 3.50a are more or less constant over the length. When focusing on the velocity in y-direction in Figure 3.50b it is noticed that there are changes in velocity. To encounter for these small fluctuation the tunnel jet speed v_j is defined in this study as:

$$v_j = \sum_{i}^{N} \frac{v_{ji}}{N} \quad \sigma, \text{ where } v_{ji} = A\int_{A_{j,k}} u_{i,j,k}\, dA_{j,k} \tag{3.9}$$

Where A is the cross-section area, $A_{j,k}$ is the area of the cutting plane inside the tunnel in the xz-plane, which is by definition equal to A. $u_{i,j,k}$ stands for the velocity at a node point at position x,y,z. The mean tunnel jet speed at each cutting plane is called v_{ji}. By taking the mean and the standard deviation on all values of v_{ji} the tunnel jet speed v_j is obtained. The tunnel jet speed represents therefore the mean value through the tunnel of the velocities in the tunnel and the standard deviation of the tunnel jet speed is a measure how much the mean tunnel speed is varying in the y-direction inside the tunnel.

In the following a qualitative and quantitative discussion for all 12 situations of the speed and thrust variation is given.

Qualitative

When the wedge has zero speed the influence of the thrust can be studied. In Figure 3.52 the thrust and therefore the torque is increased and it can be seen that the tunnel jet is accelerated. Next to that due to an increase of torque the tunnel jet gets more asymmetric. The torque introduces a rotation to the flow and because the torque is applied in the radial direction an effect in the radial distribution must be visible. This can be seen for all three situations.

The flow field at a ship speed of u_s=0.159 [m/s], which corresponds with a Froude number of 0.03 [-] can be seen in Figure 3.53. In Situation 4 the velocities inside the tunnel are nearly at rest. The tunnel jet for a thrust of 5 [N] (Situation 5) is slightly bent aft due to the ship speed. For situation 6, the flow is bent at a significant distance from the tunnel outlet. While in situation 7 for a thrust of 30 [N] the ship speed seems to have only a minor effect on the behavior of the tunnel jet.

For a ship speed of 0.318 [m/s], the effect of the ship speed on the tunnel jet is clearly visible. For situation 9 in Figure 3.54b the flow is bent directly towards the hull and a large region of low velocities exists behind the tunnel flow. For situation 10 a smaller region of low velocities is visible. The tunnel jet in situation 11 has also an effect on the flow behind the jet, but at a greater distance towards the back.

For a ship speed of 0.478 [m/s] the ship speeds causes to bent the tunnel jet towards he hull. Resulting in a large region behind the tunnel jet with low velocities (Figure 3.55).

Quantitative

For the time traces of all situations the mean and standard deviations have been calculated. The results are shown in Table 3.24. First of all when analyzing the resistance (force in x-direction) it can be seen that for the ship at rest a small negative force exists. This is probably due to the asymmetric behavior of the

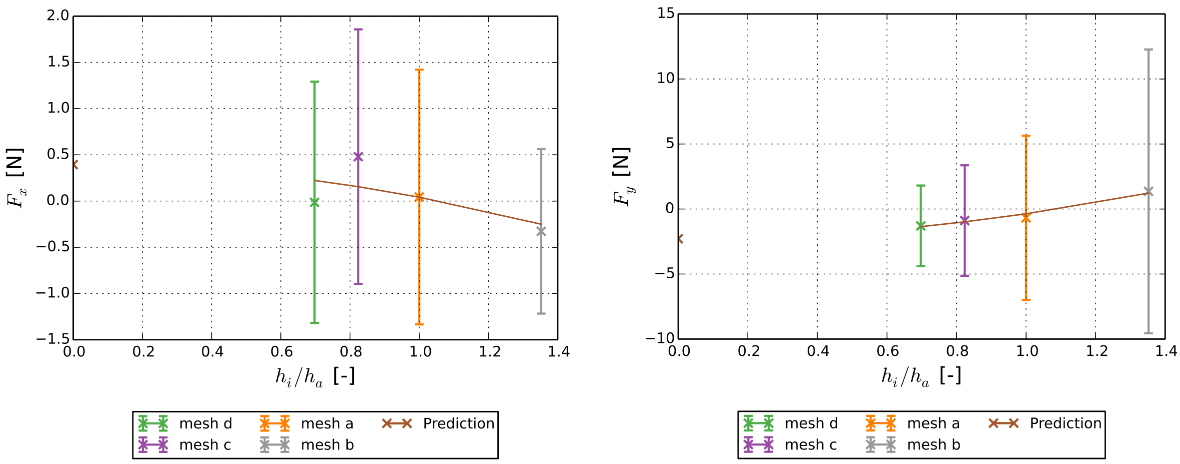

(a) Forces in the x-direction (b) Forces in the y-direction

Figure 3.49: Results of the grid study using the method of Eça and Hoekstra [17] for the force in x- and y-direction for the rest case. The errorbars indicate a 95[%] uncertainty interval, the prediction line is the best fit regression of the method.

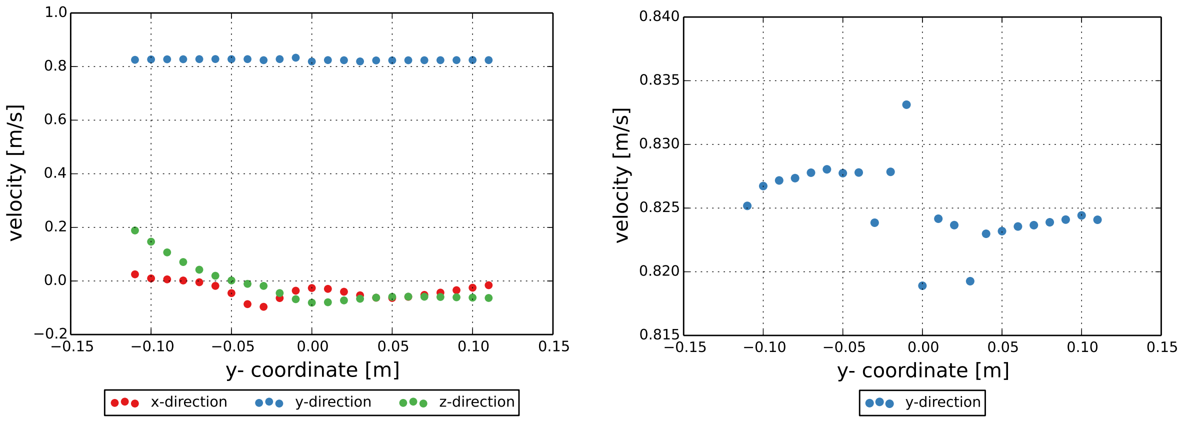

(a) Tunnel jet velocity in all three dimensions (b) Tunnel jet velocity in the direction of the tunnel

Figure 3.50: Tunnel jet velocity v_j throughout the tunnel. The figure shown is created with the data of Situation 10.

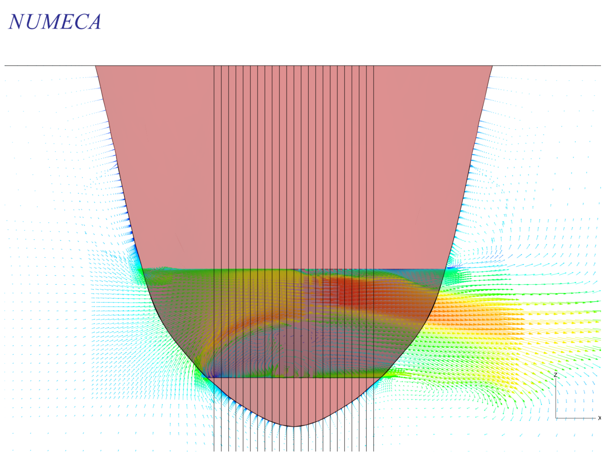

Figure 3.51: Situation 10. Definition of the xz-cutting planes inside the tunnel. The plot shows the velocity vector in the yz-plane at x=1.55 [m].

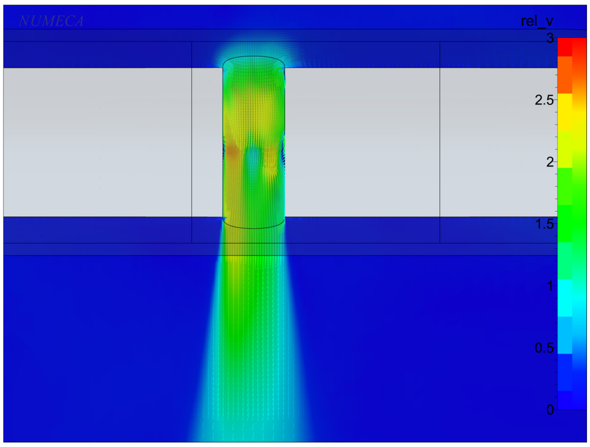

(a) Situation 1, T=5 [N]

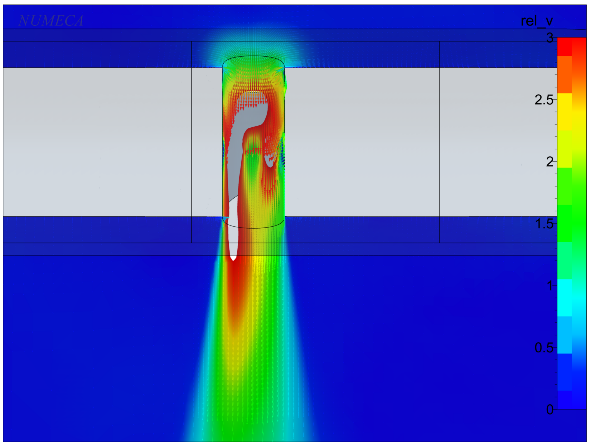

(b) Situation 2, T=10 [N]

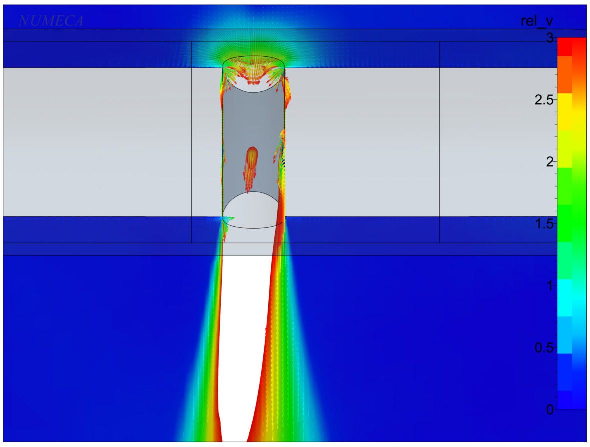

(c) Situation 3, T=30 [N]

Figure 3.52: Speed and thrust variation. Ship velocity u_s=0 [m/s]. Relative velocity v_{rel} scaled with u_s=0.318 [m/s] in the xy-plane at z=0.152 [m]. Topside of the wedge is inlet side and bottom the outlet side.

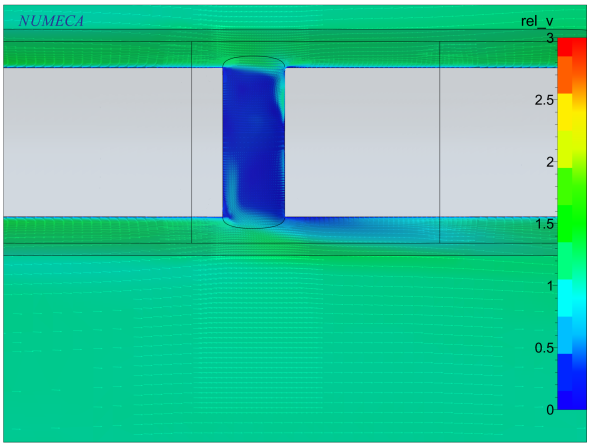

(a) Situation 4, T=0 [N]

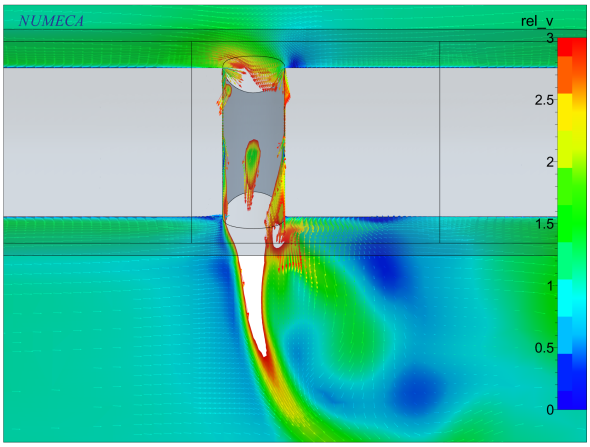

(b) Situation 5, T=5 [N]

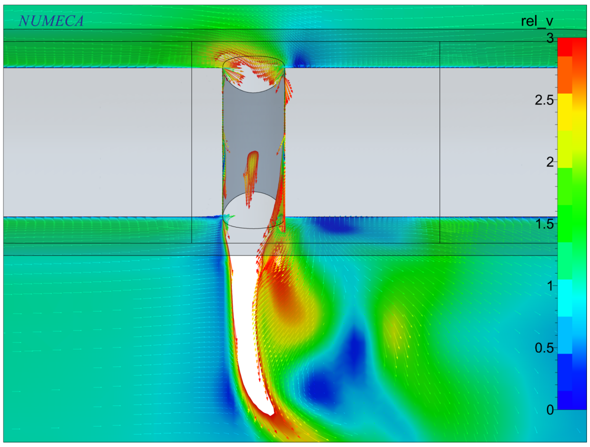

(c) Situation 6, T=10 [N]

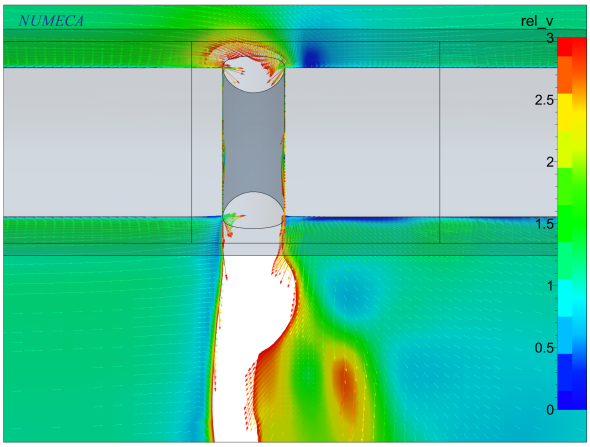

(d) Situation 7, T=30 [N]

Figure 3.53: Speed and thrust variation. Ship velocity u_s=0.159 [m/s]. Relative velocity v_{rel} in the xy-plane at z=0.152 [m]. Topside of the wedge is inlet side and bottom the outlet side.

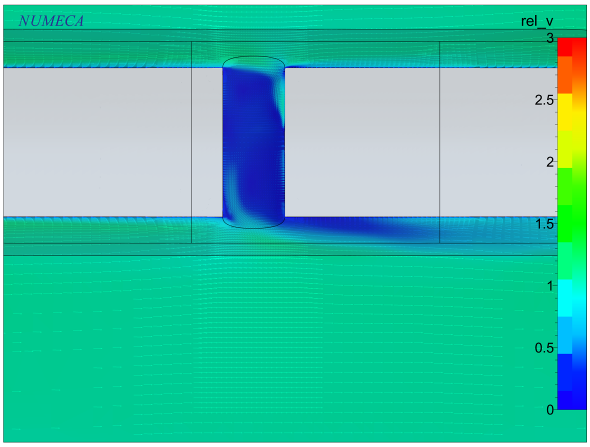

(a) Situation 8, T=0 [N]

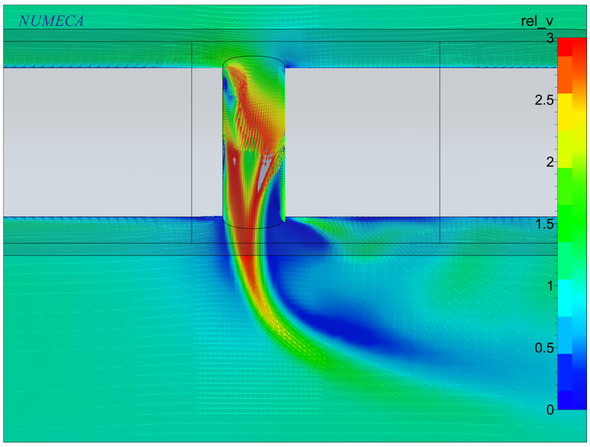

(b) Situation 9, T=5 [N]

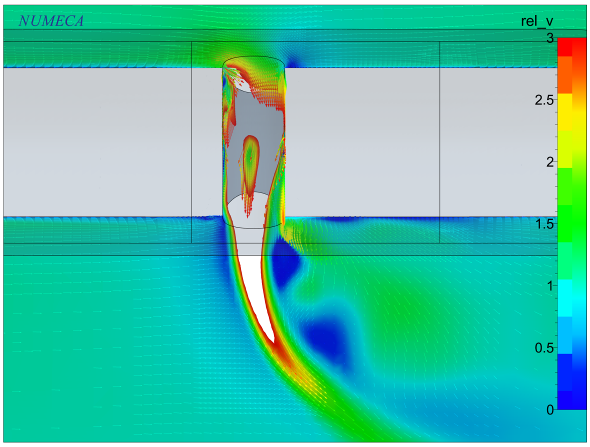

(c) Situation 10, T=10 [N]

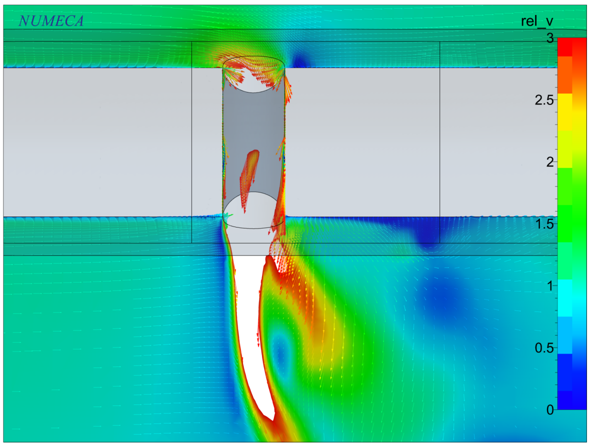

(d) Situation 11, T=30 [N]

Figure 3.54: Speed and thrust variation. Ship velocity u_s=0.318 [m/s]. Relative velocity v_{rel} in the xy-plane at z=0.152 [m]. Topside of the wedge is inlet side and bottom the outlet side.

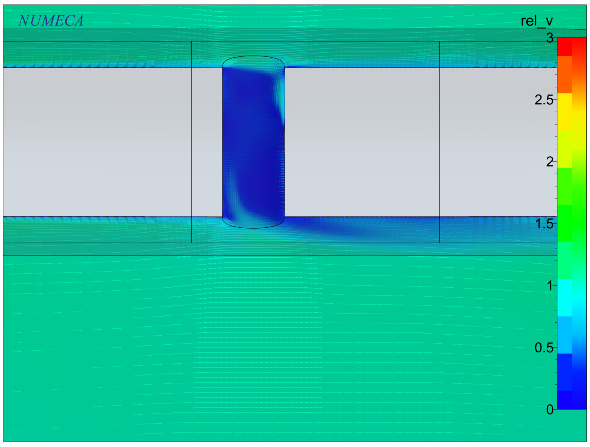

(a) Situation 12, T=0 [N]

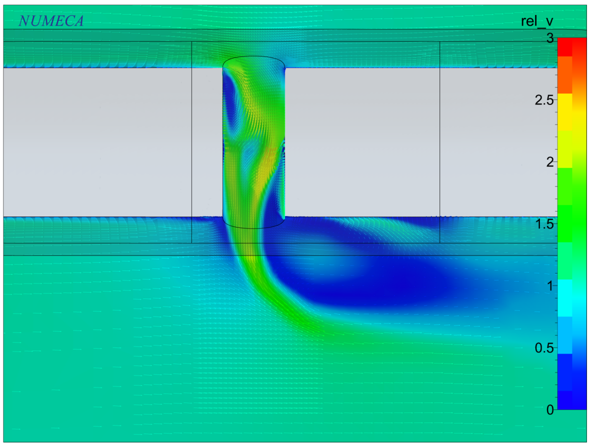

(b) Situation 13, T=5 [N]

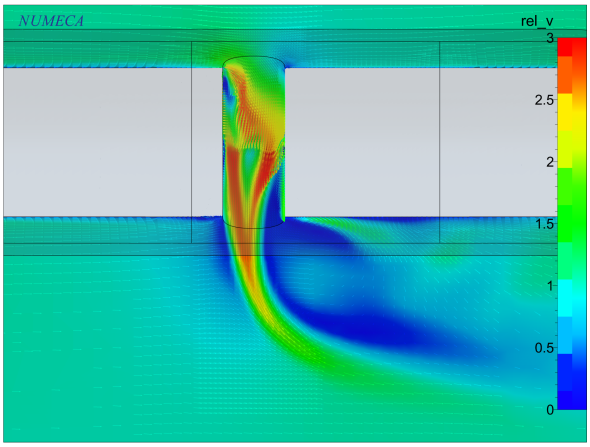

(c) Situation 14, T=10 [N]

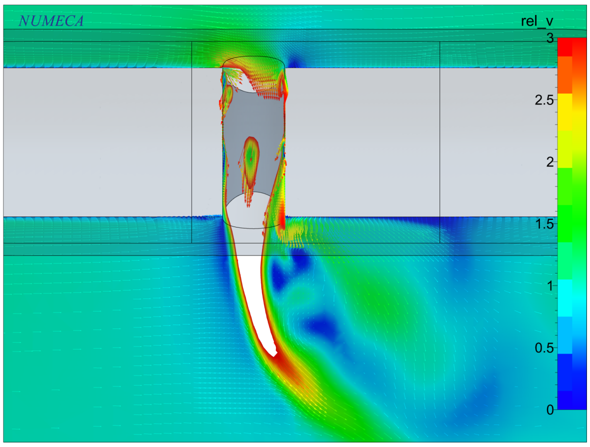

(d) Situation 15, T=30 [N]

Figure 3.55: Speed and thrust variation. Ship velocity u_s=0.478 [m/s]. Relative velocity v_{rel} in the xy-plane at z=0.152 [m]. Topside of the wedge is inlet side and bottom the outlet side.

tunnel jet due to the tangential force in the actuator disk (Compare Figure 3.52). In Figure 3.56a it can be seen that the resistance increases when the bow tunnel thruster is active. Next to that it can be seen that an increase in thrust leads to an increase in resistance. Which is expected and can be explained with the flow behavior. The ship is decelerated by the tunnel jet, as the flow around the ship needs to pass the jet. This is line with the derivation of the hypothesis [3].

When analyzing the force in the direction of the tunnel in Figure 3.56b it can be seen that the forces for the wedge at zero speed are all negative. This is due to the definition of the axis and the applied thrust. As the thrusts wake is pointing in the positive y-direction for a positive thrust T, the resulting force should be pointing in the negative y-direction. Furthermore it can be stated that for the wedge at zero speed, an increase in thrust results in an increase in force in that direction, however the relative contribution seems to decrease. From 8.6[%] for T=5 [N] to 4.5[%] for T=30 [N]. As mentioned earlier, these relative values are very low, compared with the expectation. For a ship speed of 0.159 [m/s] the force of T=30 [N] is negative, while the other two thrusts result in a positive force. This can be explained by studying the velocity ratio m for this case. In Figure 3.57b it can be seen that the value of m is roughly 0.2 [-] for T=30 [N], while m becomes roughly 0.4 and 0.6 [-], for T=10 and T=5 [N] respectively. As mentioned in the Definition Study [3] for a velocity ratio of around 0.2 [-] the tunnel jet is considered to be a strong jet that shows only little distraction from the ships flow (Compare Figure 3.53). While velocity ratios m between 0.4 and 0.6 [-] are considered a weak jet which show large interactions with the surrounding ship flow. Both can be seen in the qualitative comparison and by looking at the values in this quantitative comparison.

For higher ship velocities also the T=30 [N] case becomes a weak jet, as the ship velocity increases and while the tunnel jet velocity stays more or less constant.

Table 3.24: Result of the speed and thrust variation. The calculated mean μ and standard deviation σ is based on 1110 time steps.

	m	F_x		F_y	
Situation	[-]	μ [N]	σ [N]	μ [N]	σ [N]
1	∞	-0.36	0.004	-0.43	0.055
2	∞	-0.39	0.022	-0.58	0.062
3	∞	-0.26	0.080	-1.35	0.122
4	0.0	0.57	0.004	-0.06	0.033
5	0.28	2.58	0.075	0.68	0.464
6	0.21	3.91	0.109	0.91	0.586
7	0.12	6.39	0.116	-2.89	0.173
8	0.0	1.52	0.095	-0.20	0.096
9	0.59	4.41	0.015	0.90	0.136
10	0.39	5.83	0.060	0.36	0.342
11	0.23	12.29	0.412	3.41	2.068
12	0.0	2.88	0.067	-0.40	0.124
13	0.92	6.82	0.130	0.87	0.611
14	0.64	8.99	0.009	1.83	0.077
15	0.34	15.81	0.206	3.16	1.030

3.4.3. Qualitative and quantitative validation

Non-dimensonless data is available in literature from model test testing to validate the results of the Nienhuis wedge calculations. First a comparison of the qualitative results with literature is made, later in this section a quantitative comparison is presented.

Qualitative validation

For the qualitative validation cross-flow experiments by Goplan et al. [28] and theory of the diffusion of submerged jet by Albertson et al [29] are selected. First of all the diffusion of the tunnel jet is compared

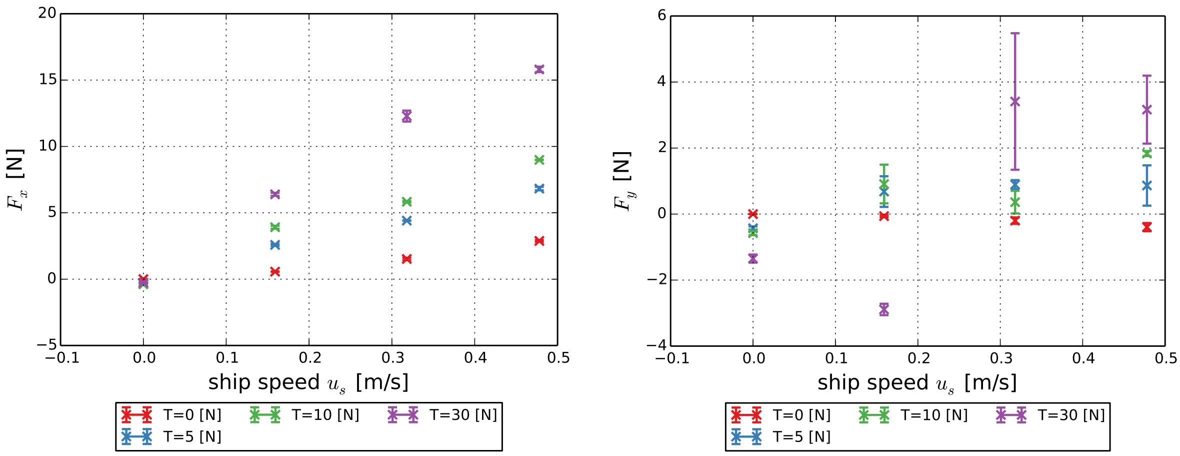

(a) F_x (b) F_y

Figure 3.56: Speed and thrust variation: Forces versus ship speed. The errorbar shows one standard deviation of the force from the time trace.

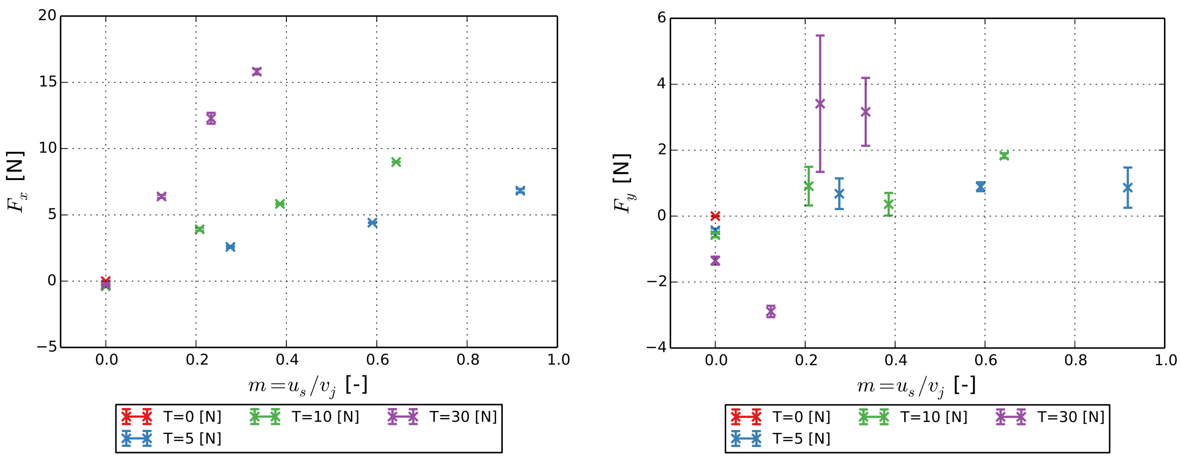

(a) F_x (b) F_y

Figure 3.57: Speed and thrust variation: Forces versus non dimensionell velocity ratio m. The errorbar shows one standard deviation of the force from the time trace.

with the velocity profile proposed by Albertson et al [29]. Secondly it is studied if a jet in a cross-flow is comparable to the flow of the bow tunnel thruster. A cross-flow study is used to verify the finding in literature (compare with the definition study [3]), which states that the bow thruster at slow forward motion shows the same behavior as a jet in a cross-flow.

Comparison of the velocity profile of the tunnel jet with Albertson et al. Albertson et al [29] presented algebraic equations for the diffusion of submerged jets. The equations are discussed in the definition study [3]. The velocity profiles of the four grids used during the grid study are used to make a comparison.

In Figure 3.58a it can be seen that the general trend is captured. It can be seen that the jet diffuses with increasing distance to the tunnel outlet (increase in y/D). Together with the diffusion also the maximum velocity decreases. Both was noticed during the grid study in Figure 3.42. The diffusion and decrease in maximum velocity agrees with the equations of Albertson et al.. However a differences are visible, while the shape of Albertson et al. is symmetric with at x/D=0.5 [-] all four computations show an asymmetric shape that is pointing forward. Again this was concluded from Figure 3.42. The asymmetric behavior is most likely due to the rotation which is due to the applied torque. Therefore an additional computation for mesh a is done where the sign of the torque in the actuator disk has been changed. The velocity profile from this computation (Q negative) are plotted together with the velocity profile of mesh a (Q positive) in Figure 3.58b. The figure shows that the velocity profile for Q negative is also asymmetric, but pointing towards the back. Based on this comparison it can be concluded, that the asymmetric is due to the direction of the applied torque. In the equation of Albertson et al. only uni-axial flow is considered, therefore a symmetric shape is obtained.

Next the velocity profile in the yz-plane is studied. In Figure 3.59a the velocity in the tunnel direction is seen. It can be seen that the flow diffuses and is asymmetric. The asymmetric in the far field points downwards in the direction of the keel. For this view the effect of the sign of torque is plotted in Figure 3.59b. It can be seen that independent of the sign of the torque the flow is moving downwards. This can be explained by the geometry of the side of the wedge. In Figure 3.51 it can be seen that side of the wedge has an angle with the vertical and is therefore not straight. This shape causes the flow to be bend downwards.

In general it can be concluded that the velocity profiles agree with the proposed equations of Albertson et al.. The differences between Albertson et al. and the computations are due to the shape of the tunnel in vertical direction and due to the included torque.

Comparison with jet in a cross-flow experiments Goplan et al. [28] performed jet in a cross-flow experiments. They injected a turbulent circular liquid jet into a turbulent cross flow at a Reynolds number Re(u_s,D_h) of 1.9E4 [-]. The presented results were measured using particle image velocimetry for values of m of 1 and 0.4 [-]. The result from Situation 10 and 13 are used to compare the normalized mean velocities. During the post-processing a similar location and plot is created as Goplan et al. [28] have made.

In Figure 3.60 a comparison for Situation 10 is given. Situation 10 (u_s=0.318 [m/s], T=10 [N]) is chosen as the velocity ratio of that Situation is the closed to the tested velocity ratio by Goplan at al [28]. In the top of the figures the velocities near the outlet are shown. Qualitative comparison shows a similar trend for the flow behavior. The bending of the tunnel jet is very similar. When looking at the normalized mean velocities it can be seen that the CFD results show higher magnitudes, but the trend seems to be similar. At a location y/D=0.5 [-] and x/D=1.0 [-] the two cases show a significant difference, while the mean velocities of the CFD results in this region are close to zero, the measured normalized mean velocities are 1.1 [-]. On the other side of the tunnel jet (y/D=-1 [-]) shows however the same behavior. The crossflow/ flow due to the speed of the wedge is significantly decreased. Also a similar shape of the isoline region can be noticed.

In the bottom of Figure 3.60 the region downstream of the tunnel exit can be seen close to the wedge. Again both cases show a similar behavior. The streamlines and the orientation of the vector agrees. The isolines and corresponding normalized mean velocities do not, but show the same trend.

A second case Goplan et al. [28] measured has a velocity ratio m of 1.0 [-]. The only CFD calculation at this velocity ratio is Situation 13 (u_s=0.478 [m/s], T=5 [N]), therefore Situation 13 is chosen as comparison. The velocity ratio of Situation 13 is around 0.9 [-]. When analyzing the flow fields in Figure

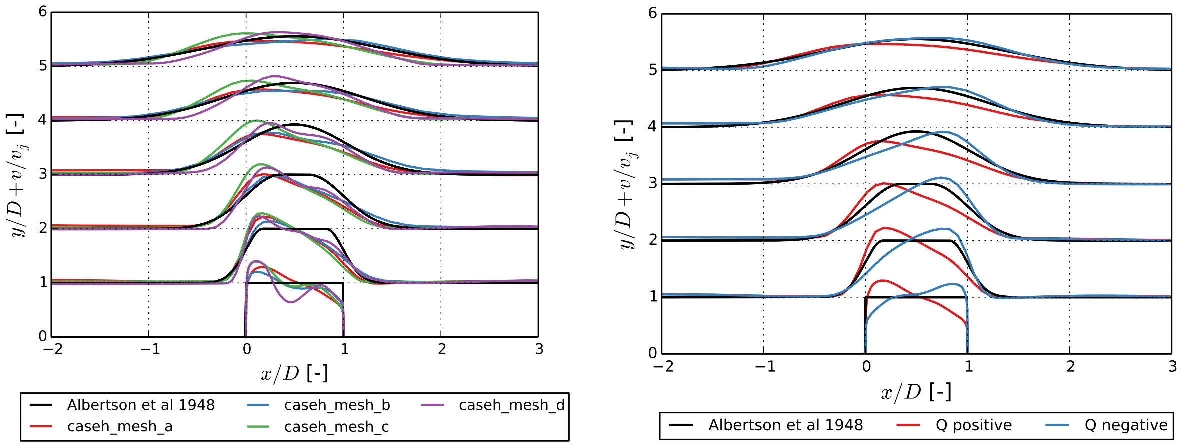

(a) Velocity profiles of the grid study in y-direction (b) Effect of the sign of the torque

Figure 3.58: Velocity profile of the grid study results and the effect of the sign of the applied torque in the actuator disk in the xz-plane. The origin of x/D is at the most forward part of the tunnel, the origin of y/D is at the side of the wedge. All velocities are at the vertical center of the tunnel (z=0.158 [m])

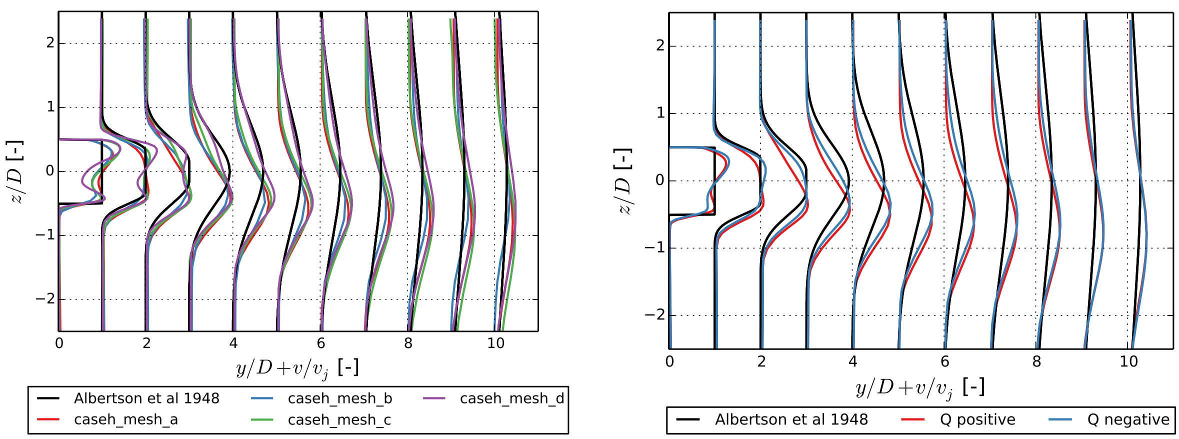

(a) Velocity profiles of the grid study (b) Effect of the sign of the torque

Figure 3.59: Velocity profile of the grid study results and the effect of the sign of the applied torque in the actuator disk in the yz-plane. The origin of z/D is at the vertical center of the tunnel (z=0.158 [m]), the origin of y/D is at the side of the wedge. All velocities are at the longitudinal position of 1.55 [m] (x/D=0.5 [-])

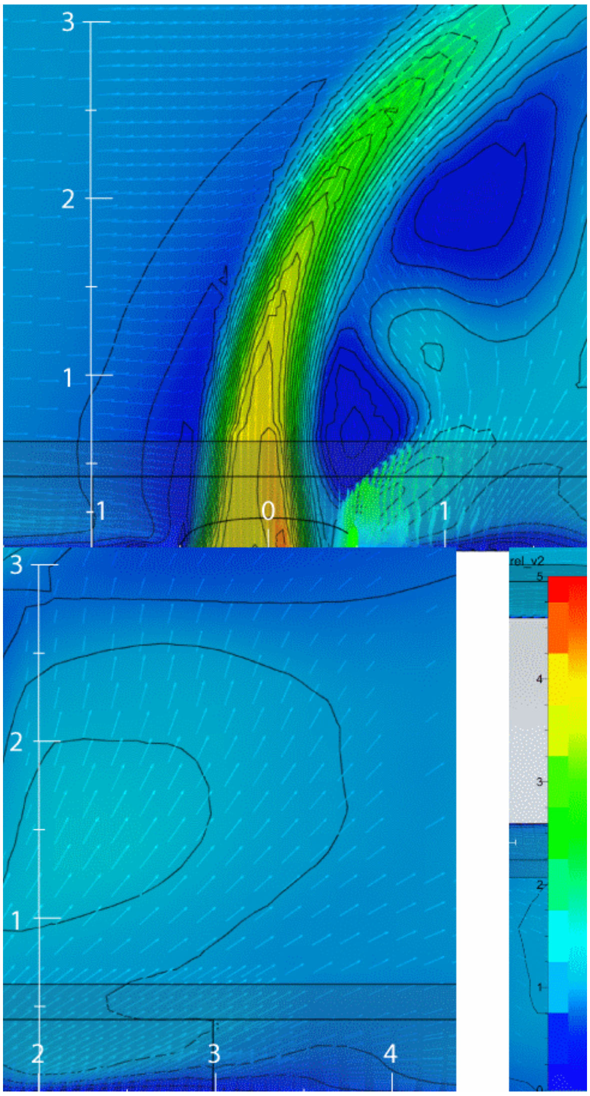

(a) Situation 10

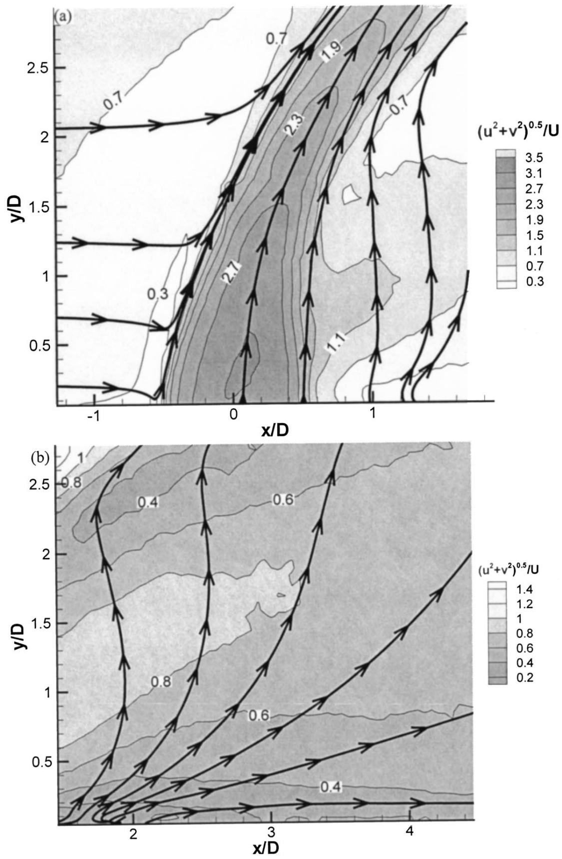

(b) Goplan et al [28, Fig. 8]

Figure 3.60: Qualitative comparison of Situation 10 with Goplan et al [28, Fig. 8]

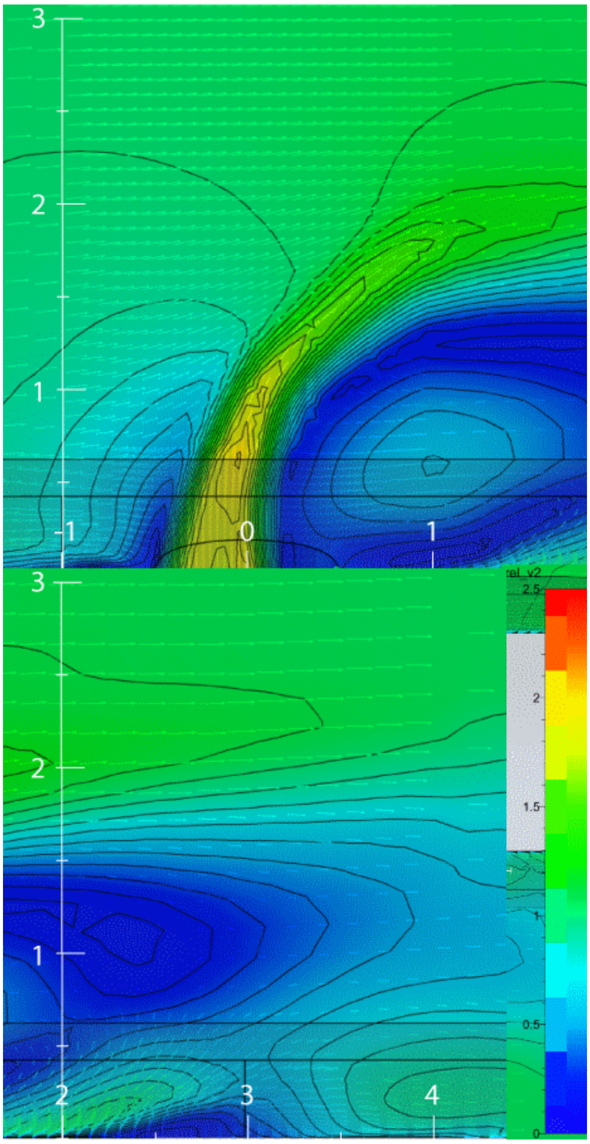

(a) Situation 13

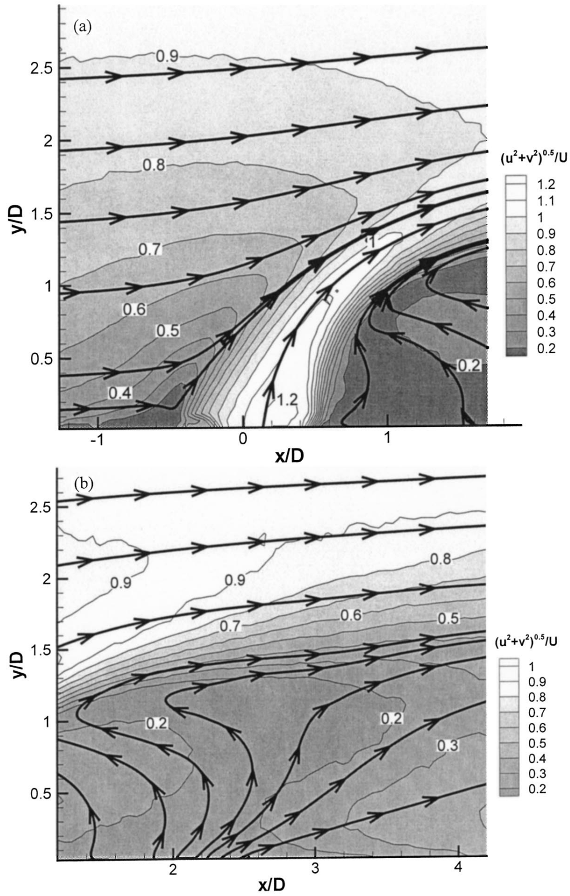

(b) Goplan et al [28, Fig. 6]

Figure 3.61: Qualitative comparison of Situation 13 with Goplan et al [28, Fig. 6]

3.61 one can see that the test of Goplan et al [28] is bending earlier than the CFD calculations. This can be explained with the difference in velocity ratio. In the CFD calculation the tunnel jet velocity is 11 [%] higher than in the tests. Besides this the same pattern is recognized. The cross-flow/ship speed is decreased significantly by the tunnel jet in the upstream direction. Behind the jet an annulus of low velocities is visible. Inside the annulus a region with large velocities can be seen for both cases.

Also for this second comparison with Goplan et al [28] the magnitude of the normalized flow velocities do not match.

In general it can be stated that Situation 10 and 13 are qualitative valid with the measurements of Goplan et al. However some local flow features and the magnitude (quantitative) of the velocities differ. This comparison clearly indicates that the flow of a bow tunnel thruster at slow forward motion is qualitative comparable with the jet in a cross-flow. And it indicates that the CFD results are qualitative valid.

Quantitative validation

The quantitative results of the CFD computations are compared in three different ways: First a comparison with the modeltests of Nienhuis is made. For the zero speed case data of the model test exists using the exact same model. The second comparison is made with multiple model test studies and literature in general, which show that a decrease in turning ability is recognized when the ship velocity increases, when the thruster is operating at the same rate of revolution. The third comparison is made with a CFD study by MARIN. The study uses a full scale hopper dredger with two bow thrusters.

Comparison with modeltest by Nienhuis For the quantitative comparison the result of Nienhuis [1] is used. The result is shown together with the result from the CFD study, Situation 1,2 and 3. The comparison in Figure 3.62 shows that the CFD results are far off the results of Nienhuis. First of all there is a definition question. Nienhuis defines the thrust deduction factor for bow tunnel thruster C_F as the ratio between the measured force F_T of the wedge in the tunnel direction divided by the measured thrust T:

$$C_{F-Nienhuis} = \frac{F_T(u_s,T) - F_T(u_s,0) - T}{T} \tag{3.10}$$

As the measured force F_T of the wedge includes by definition the thrust force applied on the wedge a different definition for the CFD results has been used:

$$C_F = \frac{F_y(u_s,T) - F_y(u_s,0)}{T} \tag{3.11}$$

In CFD the thrust is added into the source term of the governing equations, using an actuator disk. The force on the wedge is therefore only the force that the wedge feels due to the flow and not the thrust of the thruster itself.

For the results shown in Figure 3.62 the value of $F_y(0,0)$ is assumed to be zero and therefore only the side force on the wedge F_y is divided by the described thrust T.

The grid study resulted in an uncertainty of 6.3 [N] for T=10 [N]. This uncertainty corresponds with and uncertainty of C_F=0.63 [-]. Which means that the model test results of Nienhuis fall within the numerical uncertainty of the presented CFD study. However the presented results show large differences, therefore it is analyzed were the differences could possibly come from.

On the differences between the modeltests of Nienhuis and the CFD model The first difference between the model tests of Nienhuis and the CFD model is the definition of the Force coefficient C_F. In the model tests the forces of the complete model are measured in the x- and y-direction. This measured force F_T in the tunnel direction (y-direction) includes the thrust of the thruster, the reaction force of the thruster on the wedge and the force on the wedge due to the flow. In the CFD model the measured force is only the force due to the flow F_y. As the force coefficient is defined as the thrust deduction factor t the coefficient represents how much thrust is reduced due to the interaction of the thrust and the wedge.

The second aspect is, that the propeller hub and propeller strut are not included in the CFD model. The exact geometry of the tested geometry is known (Figure 3.2b) and from this geometry it can be concluded that the projected area of the hub and strut is about 20 [%] of the tunnel cross-sectional area (Compare Figure 3.63). The hub and strut have a resistance, which is not included in the CFD model. In the model

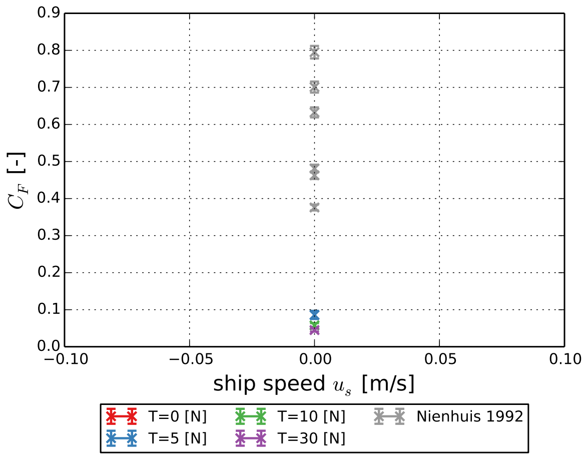

Figure 3.62: Comparison of the CFD results with model test data of Nienhuis [1].

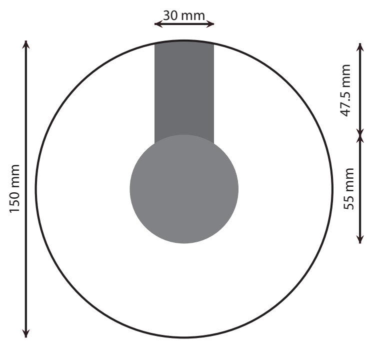

Figure 3.63: Projected area of the hub and strut inside the bow thruster tunnel used by Nienhuis [1] during model tests of the Nienhuis wedge.

used by Nienhuis this resistance is assumed to be only present when the thruster is operating. When the thruster is not operating, the flow and therefore the tunnel jet speed are negligible small. However when the thruster rotates the flow passes through the tunnel with a tunnel jet speed, which causes an increase in resistance due to the propeller hub and strut.

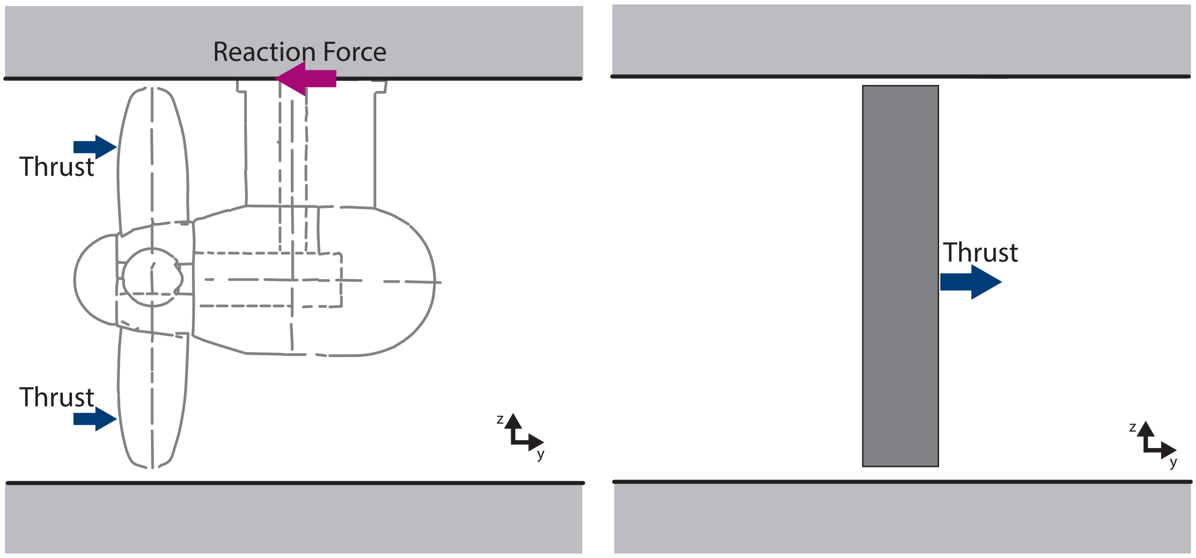

(a) Model test by Nienhuis [1]

(b) CFD model

Figure 3.64: Thrust force acting on the propeller drive and the corresponding reaction force for the model test and the CFD model. The propeller drive is adapted from [1]. The figures show only a small part of the tunnel in the yz-plane.

The third aspect is that in the model tests a reaction force of the tunnel thruster on the hull is present. According to Newton's third law if a force is exerted on an object, the object pushes back with the same force in the opposite direction. Applying this to the thruster inside the tunnel (Figure 3.64a), we can see that the thrust of the propeller pushes on the hub and strut of the propeller. As the thruster is connected to the wedge, the wedge including the thruster pushes back with the same magnitude opposite to the direction of the thrust. In the CFD model (Figure 3.64b) this is different and the reaction force is not included. The actuator disk has a prescribed thrust, which is added in the source term of the governing equations. No physical reaction force is present, that could act on the wedge. This would explain why the qualitative results are valid and the quantitative results show differences. The actuator disk induces a pressure difference. This pressure difference results in the flow through the tunnel. As the prescribed thrust in the actuator disk and the measured thrusts of Nienhuis are comparable, the same behavior is noticed. Quantitatively however the results do not agree as the reaction force of the thruster is not included in the CFD model.

When considering all three aspects together, it can be seen that the results do not differ a lot. Assuming a resistance of the hub and strut of about 2 [N] for the T=10 [N] case and adding this to the value of F_x results in a force of -2.5 [N]. When adding the reaction force, which is equal to the thrust, but in opposite direction the total force becomes 7.5 [N]. A division by the thrust results in a force coefficient C_F of 0.75 [-]. Which is within the range. It is recommended to perform computations with sliding grid and with the geometry of the hub and strut, to study the differences between the model tests and the CFD model in more detail.

Comparison with Karlikov & Sholomovich and other literature In this comparison the focus is to study the effect of an increase in ship velocity on the turning ability, while the thruster operation does not change. As discussed in the definition study [3] many authors noticed a significant decrease in transversal force with an increase in ship velocity. In most studies a relation with the speed ratio m is found. In this comparison a force coefficient C_y is used, which is defined as:

$$C_Y(u_s, T) = \frac{2F_y(u_s, T)}{\rho_w v_j^2 A} \tag{3.12}$$

Where F_y is the transverse force at ship velocity u_s and a thrust T, ρ_w the density of water, v_j the tunnel jet speed and A the area of the tunnel cross-section. The force coefficient C_y is used to define the normalized force coefficient C as:

$$C(u_s, T) = \frac{C_y(u_s, T)}{C_y(0, T)} \tag{3.13}$$

The first comparison is the normalized force coefficient C versus the speed ratio m with Karlikov & Sholomich [4] and results used by Wartsila [25]. In Figure 3.65 it can be seen that both Karlikov & Sholomovich and Wartsila shows the lowest force coefficient C at a speed ratio m of 0.5 to 0.7 [-]. It can be seen that the results of Wartsila and Karlikov & Sholomovich do not agree fully, however both show the same trend. In both studies the thruster operating is kept constant. Karlikov & Sholomovich use a water jet to simulate the thruster and therefore influence the tunnel jet speed v_j directly. They keep the tunnel jet speed constant for each line in Figure 3.65a. Wartsila on the other hand uses one full scale thruster at different thruster powers. Each polyline stands for a different constant power. When comparing the results with the CFD results in Figure 3.65c it can be seen that the trend is different. The CFD results show values around C=1 [-] and instead of a decrease an increase is noticed. This is due to the underestimated values for the zero speed case. However, when the scale of the y-axis is ignored it is noticed that a decrease in C is present between m=0.2 [-] and m=0.4 [-].

From Figure 3.65a Karlikov & Sholomovich concluded that the decrease in force coefficient C is not only dependent on the speed ratio m, but on the Reynolds number based on the ship velocity. A comparison between Karlikov & Sholomovich and the CFD results of the Nienhuis wedge based on the ship speed based Reynolds number is shown in Figure 3.66. First of all two curves are seen in Figure 3.66a. The top curve is for a streamlined cross-section and is not of interest at the moment. The bottom curve can be used to compare the results of the CFD computations in Figure 3.66b. From the comparison it can be seen that the CFD results to not result in a single curve, but three curves with different behavior.

The CFD results for the Nienhuis wedge do not agree with literature and no decrease of the transverse force coefficient C is noticed if the ship velocity is increased. It is assumed that the under prediction of the zero speed case, is a major contributor to the high values of C in comparison with literature.

Comparison with CFD results by MARIN MARIN has performed a CFD study on a trailing suction hopper wedge using CFD [7]. The settings of their calculations are comparable with the settings used in this study, with the difference that MARIN used a full scale model of the ship. Next to that MARIN used a actuator disk distribution that is similar to the default distribution of Numeca FineMarine. Two cases from the CFD tests are used for comparison with the CFD results of this study. Case 1 is the zero speed case: The ship has zero speed and the tunnel thrusters deliver a constant thrust, Case 2 is comparable to the base case: the ship moves at Fr=0.07 [-] and the tunnel thrusters deliver the same constant thrust as in the zero speed case. Case 2 has a velocity ratio m of approximately 0.5 [-]. The report of MARIN mentioned nothing about the uncertainties involved, therefore a uncertainty of 1.5 [%] is assumed.

Table 3.25: Data of a comparison with a CFD study of MARIN [7] Case 1.

	m	$(F_y + T)/T$	
Case	[-]	μ [-]	σ [-]
MARIN Case 1	∞	0.916	0.019
Situation 1	∞	0.914	0.050
Situation 2	∞	0.942	0.058
Situation 3	∞	0.955	0.117

When comparing Case 1 (Table 3.25 and Figure 3.67a) it can be seen that the exact same magnitude of the non-dimensional force is noticed in this study and for the MARIN study. This suggest that the very

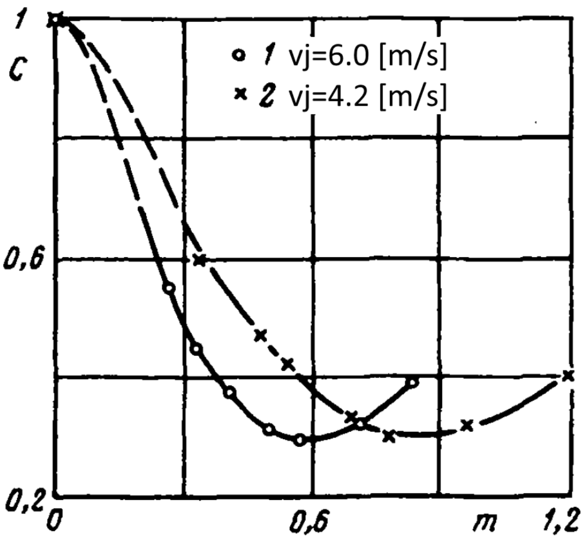

(a) Adapted from Kalikov & Sholomovich [4, Fig. 4]

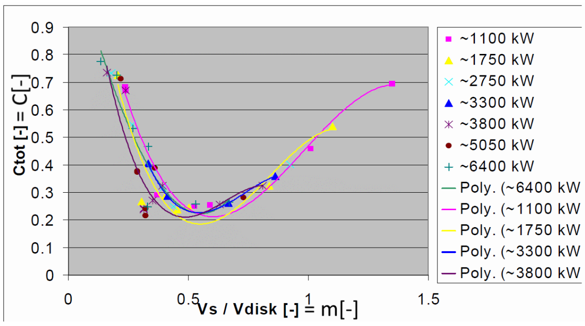

(b) Adapted from Wartsila [25, p. 58]

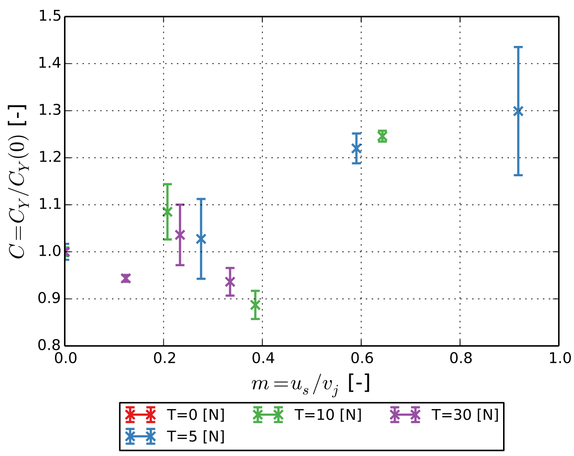

(c) CFD results of Nienhuis Wedge

Figure 3.65: Comparison with Karlikov & Sholomovich [4] and Wartsila [25].

low forces (<10 [%] T] in the direction of the tunnel are not due to the selected geometry or the used scaling.

Secondly both the MARIN CFD computation and the presented CFD studies in this report use an actuator disk with a constant thrust. The question arises if this is a good assumption.

Table 3.26: Data of a comparison with a CFD study of MARIN [7] Case 2.

	m	$(F_y + T)/T$	
Case	[-]	μ [-]	σ [-]
MARIN Case 2	0.5	0.904	0.019
Situation 15	0.34	1.105	1.139
Situation 10	0.39	1.036	0.354
Situation 9	0.59	1.180	0.160
Situation 14	0.64	1.183	0.091

When the ship is moving in Case 2, MARIN noticed a slight increase in the force [7]. For the presented CFD study the forces have changed sign and result in non-dimensional forces higher than 1 [-]. The standard deviation of the presented study are high as can be seen in Table 3.26. This results in the plot shown in Figure 3.67b. This Figure show that MARIN Case 2 results are within the errorbar of Situation 10 and 15.

MARIN [7] concluded that based on their CFD computations the effect of a decrease in turning ability in slow forward motion can not be fully explained. This is interesting as the same occurs based on the results of the presented study. This means in general it can be stated that the non-dimensional forces for Case 1 agree with the results of MARIN and for Case 2 a similar trend was noticed. Which means that the results of both CFD studies are comparable, but do not explain the behavior that is noticed during sea-trials or during model testing.

Effect of the tunnel velocity due to the wedge velocity It was noticed that the velocity inside the tunnel seems to increase when the wedge forward velocity increases. To check this a tunnel speed ratio is defined as the ratio between the tunnel speed at a certain wedge velocity u_s divided by the tunnel speed when the wedge has zero speed:

$$v_T = \frac{v_j(u_s)}{v_j(0)} \tag{3.14}$$

Figure 3.68a shows that the tunnel speed is dependent on the wedge speed. However no clear trend is visible. For T=5 [N] the effect seems to decrease, were as for T=30 [N] the effect seems to increase for an increase in ship speed. All three thrusts have one point were the tunnel speed is increased by at least 10 [%] in comparison to the tunnel speed at zero speed. The fluctuation suggests to plot the tunnel speed ratio versus the velocity ratio m. Figure 3.68b shows this. It can be seen that all points follow the same trend. This trend indicates that the tunnel speed ratio increases until a velocity ratio of 0.4 [-] and then decreases again.

An increase in tunnel speed, means that the actuator disk is accelerating the water more, to reach the desired constant thrust. For a real propeller this means, if the rate of revolution n of the propeller is constant and the pitch and diameter D of the propeller remain the same the advance number of the propeller J increases, as the advance speed increases [30].

$$J = \frac{v_a}{nD} \tag{3.15}$$

When the advance number J increases the thrust coefficient K_T decreases. And with a constant rate of revolution n, diameter D and water density ρ_w the thrust T will decrease as well [30]:

$$K_T = \frac{T}{\rho n^2 D^4} \tag{3.16}$$

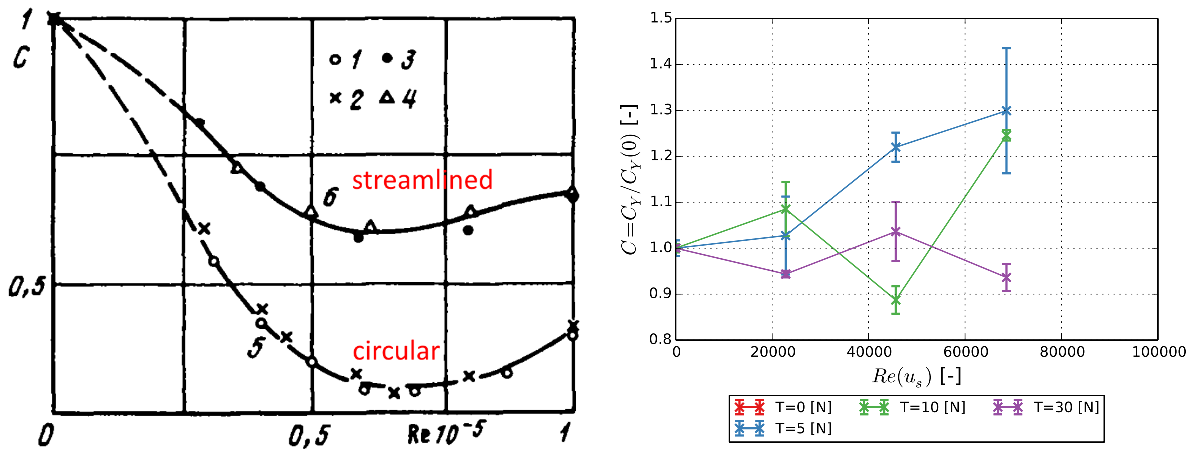

(a) Adapted from Kalikov & Sholomovich [4, Fig. 5] (b) CFD results of Nienhuis Wedge

Figure 3.66: Comparison with Karlikov & Sholomovich [4] versus the ship speed based Reynolds number. The numbers correspond with tunnel jet speeds v_j: 1=6.0 [m/s], 2=4.2 [m/s], 3=6.8 [m/s], 4=4.7 [m/s]. The top curve is for a streamlined cross-section the bottom for a circular cross-section. The plotted results of the CFD study are for the Nienhuis wedge with circular cross-section.

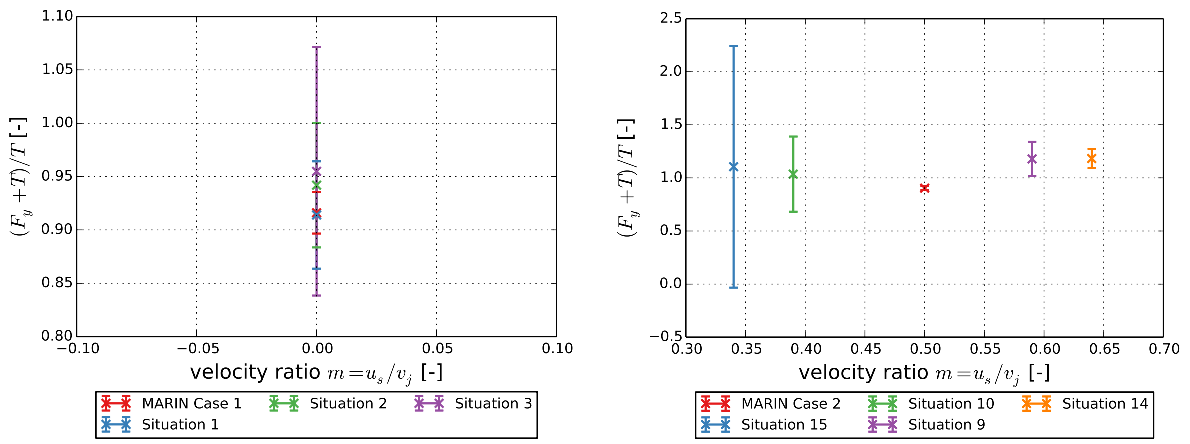

(a) Case 1 (b) Case 2

Figure 3.67: Comparison with CFD results of MARIN [7]. Error bars are based on 1.5 [%] for the Marin results and on the standard deviation of the time trace for this study.

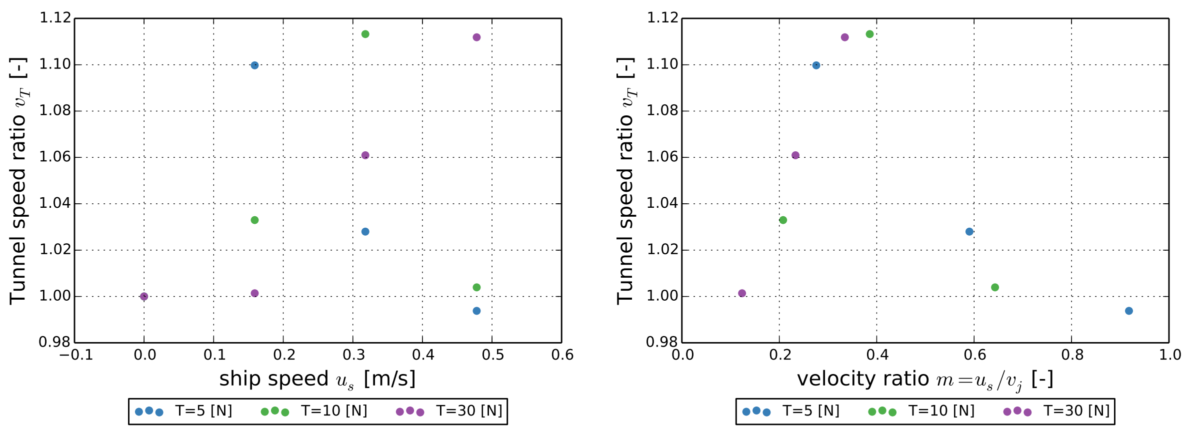

(a) Function of wedge speed u_s (b) Function of velocity ratio m

Figure 3.68: Tunnel speed ratio v_T as function of the wedge speed and the velocity ratio.

Next to the thrust coefficient K_T also the torque coefficient K_Q decreases with an increase of the propeller advance number J. And therefore again with a constant rate of revolution n, diameter D and water density ρ_w the torque Q will decrease as well[30].

$$K_Q = \frac{Q}{\rho n^2 D^5} \tag{3.17}$$

It is therefore concluded that at a velocity ratio m of 0.4 [-] an increase of 10 [%] for the tunnel speed v_j is noticed in comparison to the zero speed case. It is assumed that this results in a decrease in thrust and torque that the propeller inside the bow tunnel thruster delivers. This decrease seems to be of importance. The assumption that a constant thrust can be used in the comparison is invalid. It is advised to use a sliding grid with a constant rate of revolution and measure the corresponding thrusts at different wedge velocities.

The presented conclusion is expected to be another contribution to explain the differences between the measured trends and the trends shown in CFD simulations in this study and by [7].

4

Systematic tunnel cross-section variation for a Hopper wedge

After the study of the Nienhuis wedge in Chapter 3 a wedge based on a trailing suction hopper dredger is developed, the so called Hopper wedge. The details of the model, its meshing and the set-up of the computations for the Hopper wedge are presented in the first part of this chapter. The second part gives a small comparison between the Hopper wedge with a cylindrical tunnel and the Nienhuis wedge. In the last part of this chapter computations with three systematic varied cross-sections of the tunnel are shown.

4.1. Modeling, meshing and set-up of the computations

In this section the modeling of the geometry and the settings used during meshing and the set-up of the computations are shortly discussed. In general the procedure described in Chapter 3 is used.

4.1.1. Modeling of the geometry

The Hopper wedge is based on the trailing suction hopper dredger Vox Maxima. The frame where the most forward bow tunnel thruster is located has been used for this study. The frame is scaled linear based on the tunnel diameter. The used scaling ratio is 15.28 [-]. The points and resulting frame used to create the hopper wedge are shown in Figure 4.1. As linear scaling was used, the position of the tunnel centerline above keel has changed as well. The main particulars of the Hopper wedge is shown in Table 4.1. The biggest changes are the increase in beam and in block coefficient.

Table 4.1: Main particulars of the Nienhuis wedge and the Hopper wedge as used in this study

Particular	Symbol	Unit	Nienhuis wedge	Hopper wedge
Length overall	L	[m]	3.1	3.1
Beam	B	[m]	0.546	1.506
Draft	T	[m]	0.508	0.508
Block coefficient straight section	C_B	[-]	0.715	0.932
Tunnel diameter	D	[m]	0.15	0.15
Tunnel center z location above keel	z_{ref}	[m]	0.152	0.1096

4.1.2. Systematic variation of the tunnel cross-section

In the definition study [3] a systematic variation for the tunnel cross-section has been developed. In the following these equations are given, the three selected cross-sections are shown and the modeling of the bow thruster tunnel is explained.

The cross-section as defined in Figure 4.2a consists of two semicircles which ends are connected by a straight line. The diameter of the semicircles are D_L and D_R for the left and right semicircle, respectively.

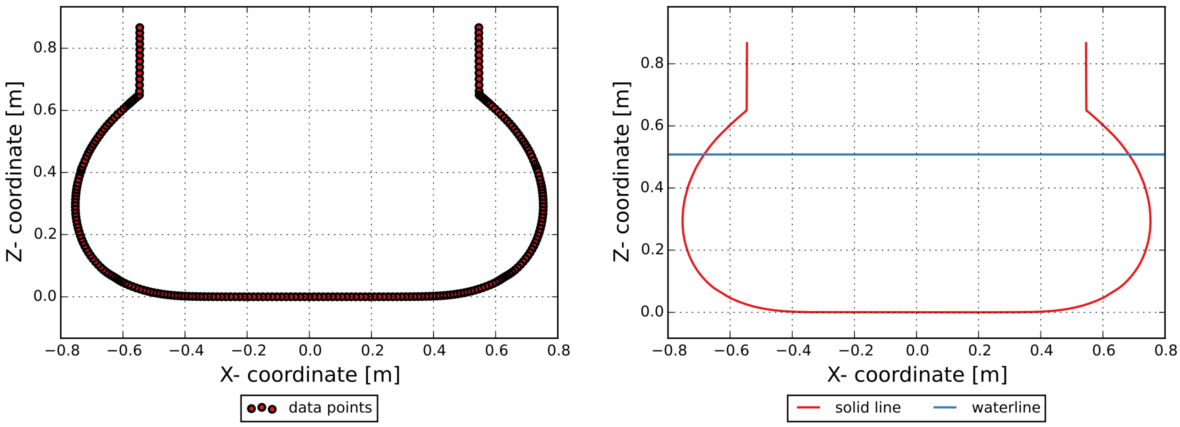

(a) Data points

(b) Solid line

Figure 4.1: Frame of the CFD model of the Hopper wedge. The data points and the resulting frame using solid lines.

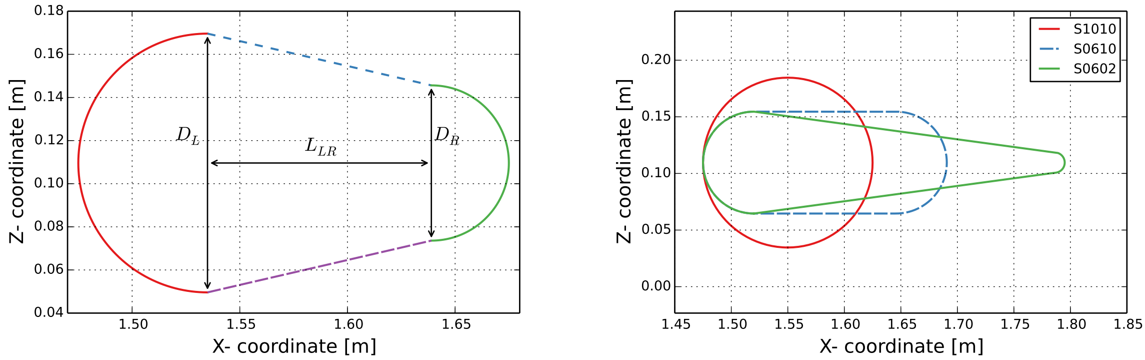

(a) Definition of the SAABB series

(b) Used SAABB cross-sections in this study

Figure 4.2: Definition of the SAABB cross-section series and the three used SAABB cross-sections.

The systematic tunnel cross-section series SAABB is defined by two values AA and BB. Dividing the values for AA and BB by ten results in the ratios r_{AA} and r_{BB}. The ratio r_{AA} between a reference diameter D_{ref} and the left diameter D_L is defined as:

$$r_{AA} = \frac{D_L}{D_{ref}} \tag{4.1}$$

The ratio between the left and the right diameter is defined as r_{BB}:

$$r_{BB} = \frac{D_R}{D_L} \tag{4.2}$$

To allow a comparison of all tunnel cross-sections the area of the systematic outlet series is the same as the area of a reference circle with diameter D_{ref}. The area of the cross-section can be expressed using the two diameters of the semicircle and the distance L_{LR} between the semicircles as:

$$A = \frac{\pi}{8}\left(D_L^2 + D_R^2\right) + L_{LR}\left(\frac{D_L}{2} + \frac{D_R}{2}\right) = \frac{\pi D_{ref}^2}{4} \tag{4.3}$$

The distance L_{LR} can thus be determined as:

$$L_{LR} = \frac{\pi\left(D_{ref}^2 - 2D_L^2 - 2D_R^2\right)}{2\left(D_L + D_R\right)} \tag{4.4}$$

The perimeter P can be calculated as:

$$P = \frac{\pi}{2}\left(D_L + D_R\right) + 2\sqrt{L_{LR}^2 + \left(\frac{D_L - D_R}{2}\right)^2} \tag{4.5}$$

In this study three cross-sections are used S1010, S0610 and S0602, all three are shown in Figure 4.2b. To install such a cross-section in a real ship, it needs to be cylindrical at midship to install a standard bow thruster propeller. To the side the cross-section changes fluently to the defined cross-section. In this study the following dimensions have been used for this: for the cylindrical section 0.05 [m] from midship, the transition area from 0.05 to 0.035 [m] from midship and the SAABB cross-section hereafter. A rendering can be seen in Figure 4.3. The hull of the vessel is used to cut the tunnel on the open end. The tunnel design is axis symmetric with the y-axis. Next to that the forward most point of the tunnel is kept constant as can be seen in Figure 4.2b. This definition inside the wedge is further referred to as "A" behind the SAABB number, in this case S0602A.

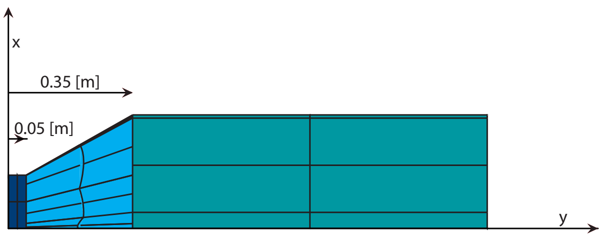

Figure 4.3: Rendering of the tunnel geometry. At the left midship is located and a cylindrical section is used for the propeller, then a transition area is used before the SAABB cross-section is used. The plot shows the S0602A tunnel.

The tunnel inside the hopper wedge can be seen in Figure 4.4 for the S0602A case. A perspective view for S1010A and S0610A are shown in Figure 4.5a and 4.5b

4.1.3. Meshing

For the meshing the same settings have been used as for the Nienhuis wedge (Section 3.2.2). The only difference is the definition of the refinement boxes. The refinement boxes for the Hopper wedge have been increased to capture more from the flow behavior, next to that due to the change in tunnel cross-section bigger boxes are needed to cover all possible variations. The boxes are defined as shown in Table 4.2.

The resulting mesh for S0602A can be seen in Figure 4.6. The number of cells for the three cases are shown in Table 4.3.

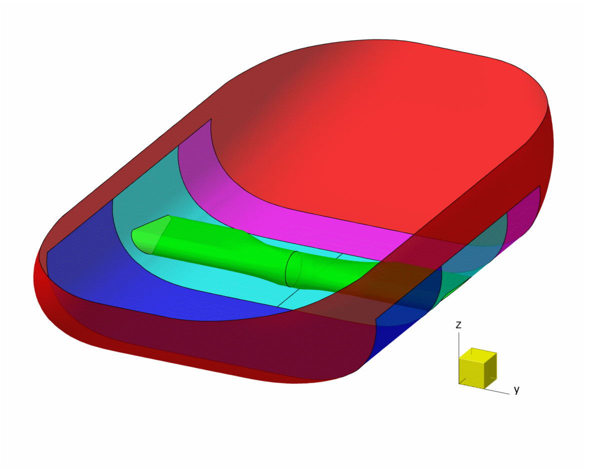

(a) Perspective

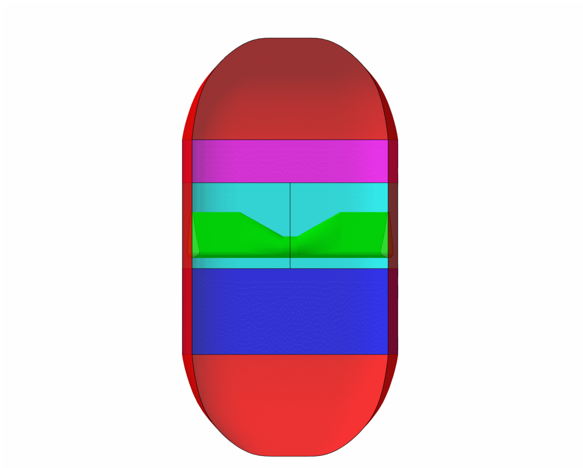

(b) XY-plane

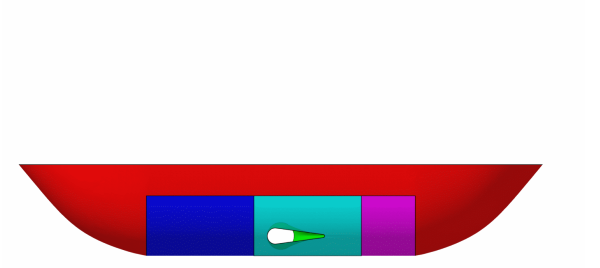

(c) XZ-plane

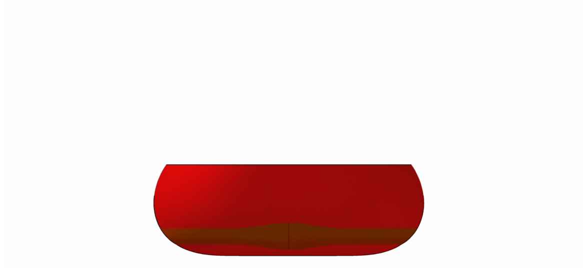

(d) YZ-plane

Figure 4.4: Overview of the hopper wedge with the S0602A tunnel. Names of the solids are: red= Hull, blue= front_midship, tourquoise= TT_side, green= TT_tunnel, magenta= aft_midship

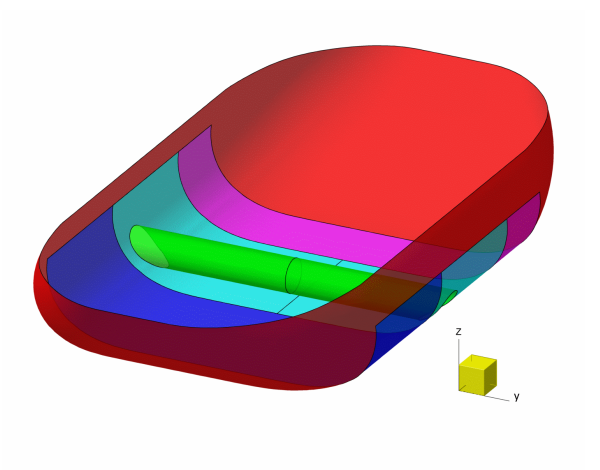

(a) S1010A

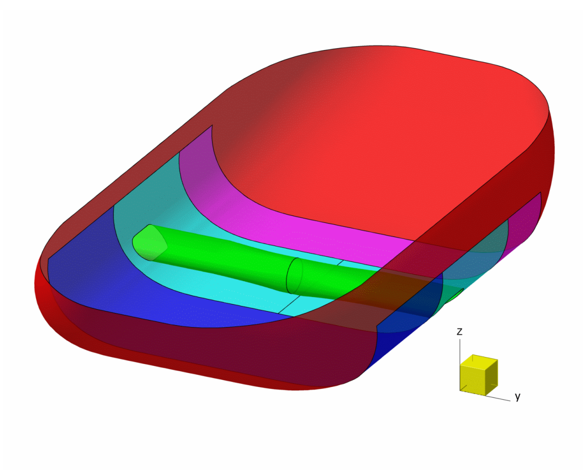

(b) S0610A

Figure 4.5: Perspective view of the hopper wedge with the S1010A and S0610A tunnels. Names of the solids are: red= Hull, blue= front_midship, tourquoise= TT_side, green= TT_tunnel, magenta= aft_midship

Table 4.2: Definition of the refinement boxes used for the Hopper wedge.

	lower boundary			upper boundary		
Name	x [m]	y [m]	z [m]	x [m]	y [m]	z [m]
Box 1	1.4	-2.0	0	2.0	2.0	0.3346
Box 2	1.475	-0.05	0.02	1.625	0.05	0.2
Box 3	1.4	-0.8	0.02	2.0	-0.05	0.2
Box 4	1.4	0.05	0.02	2.0	0.8	0.2
Box 5	1.4	-1.4	0.02	2.0	-0.8	0.2
Box 6	1.4	0.8	0.02	2.0	1.4	0.2

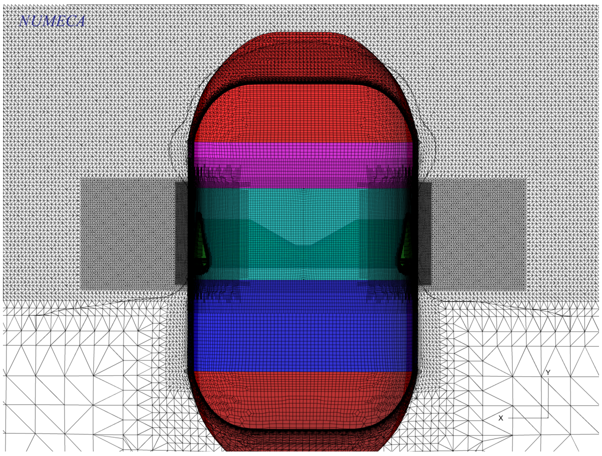

Figure 4.6: Grid of S0602A at the center location of the tunnel z=0.1096 [m]. The grids of S1010A and S0610A are generated in the same way.

Table 4.3: Overview of the three tunnel cross-sections and there corresponding grids.

Tunnel	Number of cells [-]	time step [s]
S1010A	3370292	0.0061
S0610A	3280307	0.0061
S0602A	3474569	0.0061

4.1.4. Computation settings

The same settings as for the Nienhuis wedge are used for the hopper wedge. These are:

- testing matrix with two different ship speeds and one thrust
- grid refinement ratio r=2
- y+=1 [-], no slip
- free-surface: double body with mirror plane at waterline
- actuator disk: constant distribution with tangential forces
- time step based on Courant cell number t depends on grid
- 4 non-linear iterations for 1000 [-] time steps, restart with 256 non-linear iterations until vessel has moved 1.5 L

A test matrix is developed to compare the three different tunnel cross-sections. The test matrix is shown in Table 4.4, the time step is constant for all three cases and is 0.0061 [s]. The same actuator disk settings as for the Nienhuis wedge are used.

Table 4.4: Testmatrix for the Hopper wedge

Case	u_s [m/s]	T [N]	Q [Nm]
1	0	10	0.139
2	0.159	10	0.139
3	0.318	10	0.139
4	0.318	0	0

4.2. Comparison of the Hopper wedge with the Nienhuis wedge

In this section the Hopper wedge with a cylindrical cross-section (S1010A) is compared to the Nienhuis wedge. This is done for three cases Case 1, 2 and 3 in a qualitative and quantitative way.

4.2.1. Qualitative

When looking at the relative velocities for the Hopper and the Nienhuis wedge in Figure 4.7, it can be seen that the velocities at the outlet of the tunnel are lower for the Hopper wedge in comparison to the Nienhuis wedge. This is as expected as an increase in tunnel length will result in a pressure loss and therefore in a decrease of the velocity, as described in the Definition study [3] . As a result of this, the tunnel flow is bent earlier towards the hull, compare Figure 4.7c and 4.7d and Figure 4.7e and 4.7f. For Case 3 a wake region for the Hopper wedge is visible behind the tunnel jet.

Due to the wide shape of the Hopper wedge it is expected that the resistance for the Hopper wedge is higher in comparison to the Nienhuis wedge. The tunnel length seems to result in a more ordered flow. When the tunnel jet leaves the Hopper wedge it is less spread in the x-direction in comparison with the Nienhuis wedge. The core of the tunnel jet is in Case 1 for the Nienhuis wedge more towards the back of the wedge (Figure 4.7a), while for the Hopper wedge it is more in the center of the flow (Figure 4.7b).

4.2.2. Quantitative

In Figure 4.8 the forces of the two wedges for the Case 1, 2 and 3 are shown. First of all it is noticed that the Hopper wedge has a similar velocity ratio m compared to the Nienhuis wedge. However at m=0.4 [-] the speed ratio is higher for the Hopper wedge, this means that the mean tunnel jet speed of the Hopper wedge is smaller than of the Nienhuis wedge for that case. Next to that it can be seen that the resistance for Case 1 and Case 3 is higher for the Hopper wedge in comparison to the Nienhuis wedge and for Case 2, the other way around.

When analyzing the forces in y-direction in Figure 4.8b it can be seen that the absolute values for the Hopper wedge are higher in comparison to the Nienhuis wedge. The same can be noticed from the numerical results in Table 4.5.

From the comparison between the two wedges it can be concluded, that the resistance for the hopper wedge is significant higher at m=0.4 [-] in comparison to the Nienhuis wedge. At the other two tested

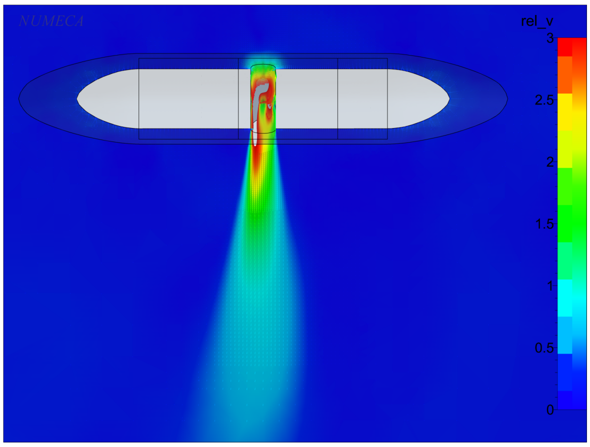

(a) Nienhuis wedge, Case 1 (=Situation 2)

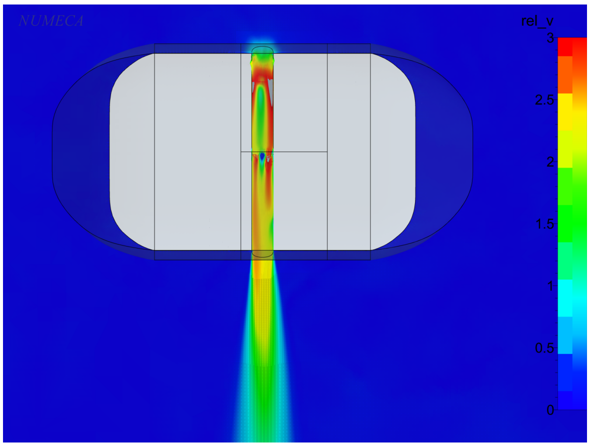

(b) Hopper wedge S1010A, Case 1

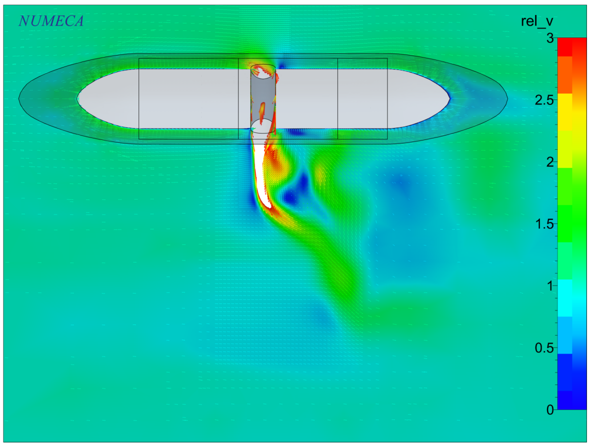

(c) Nienhuis wedge, Case 2 (=Situation 6)

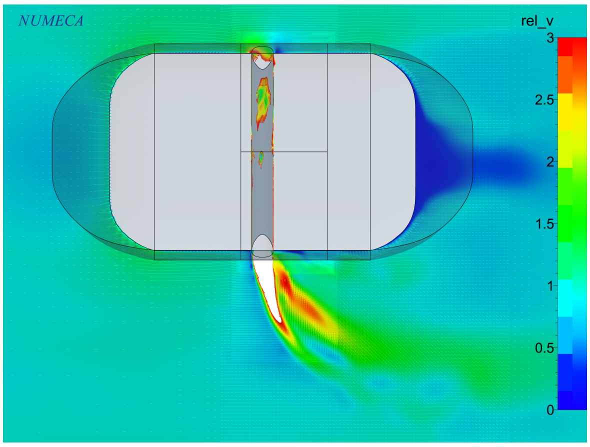

(d) Hopper wedge S1010A, Case 2

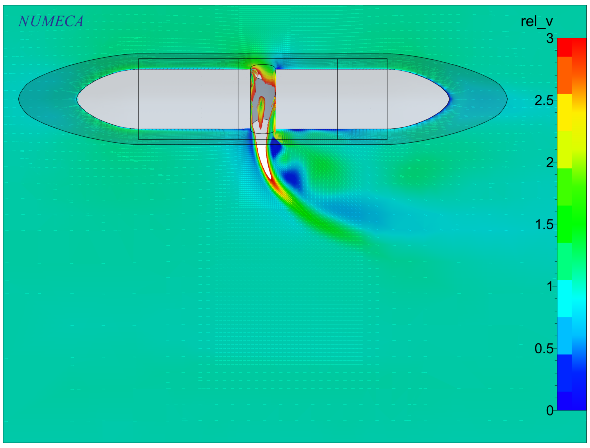

(e) Nienhuis wedge, Case 3 (=Situation 10)

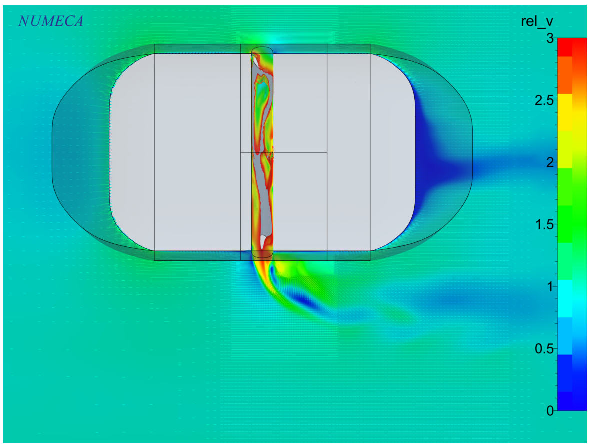

(f) Hopper wedge S1010A, Case 3

Figure 4.7: Comparison of the Nienhuis and Hopper wedge. Relative velocity v_{rel} in the xy-plane. Topside of the wedge is inlet side and bottom the outlet side.

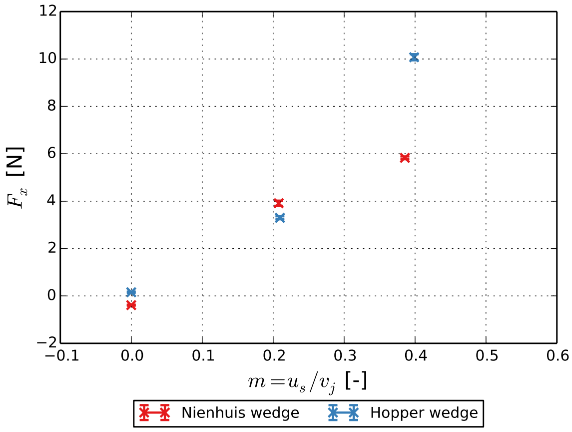

(a) F_x

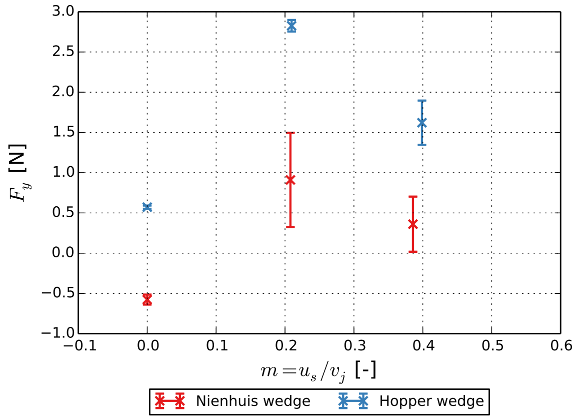

(b) F_y

Figure 4.8: Comparison of the Nienhuis and Hopper wedge: Forces versus velocity ratio m. The errorbar shows one standard deviation of the force from the time trace.

Table 4.5: Result of the comparison between the Nienhuis and Hopper wedge. The calculated mean μ and standard deviation σ are based on the measuring section of 1.5 L.

		m	F_x		F_y	
Case	Wedge	[-]	μ [N]	σ [N]	μ [N]	σ [N]
1	Nienhuis	∞	-0.40	0.022	-0.58	0.062
1	Hopper	∞	0.16	0.028	0.57	0.020
2	Nienhuis	0.208	3.91	0.109	0.91	0.586
2	Hopper	0.210	3.30	0.063	2.82	0.072
3	Nienhuis	0.386	5.83	0.060	0.36	0.342
3	Hopper	0.399	10.07	0.13	1.62	0.275

m values the difference in resistance is small. A small decrease of the mean tunnel jet velocity v_j of the Hopper wedge for m=0.4 [-] is recognized in comparison to the Nienhuis wedge, however at m=0.2 [-] the trend is the other way around. For the forces in the direction of the tunnel it is observed that the absolute values for the Hopper wedge are higher than for the Nienhuis wedge.

4.3. Systematic tunnel cross-section variation

Three different systematic tunnel cross-sections have been analyzed. First the S1010A, which is the standard circular tunnel cross-section. Second the S0610A, which is flattened and is often used within IHC for trailing suction hoppers. The shape is often used to ensure that the bow thruster tunnel is underneath the water and therefore a flattening of the tunnel is chosen to avoid the suction of air into the bow thruster tunnel. The third cross-section the S0602A is chosen, because it is a streamlined cross-section and will be used to test the hypothesis of this study. In the following the three cross-sections are computed in CFD and are compared.

4.3.1. Qualitative

When the hopper wedge has zero speed and the bow thruster (actuator disk) is working (Case 1) the relative velocity shown in Figure 4.9 is changing with the different cross-sections. The tunnel jet gets wider for the S0610A and S0602A, this is mainly, because the tunnel cross-section is longer in the longitudinal direction. The shapes of S0610A and S0602A result in a different velocity distribution inside the tunnel. Case 2 at a wedge speed of 0.159 [m/s] in Figure 4.10 shows similar behavior for S1010A and S0610A. For both cases, the tunnel jet is bent at some distance from the tunnel outlet. This implies that the relative speed of the tunnel jet is high enough at the outlet to travel some distance before the influence of the ship flow is bending the flow towards the stern of the wedge. The behavior has completely changed at Case 3 in Figure 4.11. Here the relative velocity is about twice the wedge speed. The weak jet is bent directly by the flow of the ship towards the stern. S1010A shows a clear wake region towards the back, this same wake region occurs for S0610A and S0602A, but are much smaller. This region for S0602A is smaller than for S0610A. It is expected that the wake region gives a good indication on the performance of the wedge. A smaller region should result in better turning performance.

In Figure 4.12 Case 4 is shown. In Case 4 the thruster is not working, while the ship is moving with u_s=0.318 [m/s]. This case is analyzed to study the effect on the resistance of the change in cross-section. It can be seen that the water inside the tunnel is at rest. At both sides of the tunnel an interaction with the flow around the ship is visible. For the S0602A cross-section in Figure 4.12c higher velocities can be seen at the back of the tunnel. In general the flow pattern is as expected, however the wake region behind the wedge is asymmetric.

For Case 1,2 and 3 the interaction of the tunnel jet with the flow around the ship is studied. For this multiple cuts at different y-positions have been made and the normalized tunnel jet speed has been plotted in the resulting xz-planes. In Figure 4.13 Case 1 is shown. It can be seen that the cross-sectional shape pushes the flow in the desired shape. With an increase in distance from the tunnel outlet the shapes begins to fade away and the outside at the side of the jet the velocity is decreased. As the flow around the ship is zero for this case the tunnel jet shows normal jet behavior.

In Case 2 the ship is moving and therefore interaction between the tunnel jet and the ship flow can be seen in Figure 4.14. At a distance close to the center of the tunnel (y=0.7 [m]) the three cross-sectional shapes can be recognized. With an increase in distance the shape becomes harder to recognize. All three cross-sections show horseshoe vortices at a distance y=0.8 [m]. For the S1010A cross-section the round jet is squeezed together, moves to the back and is affecting a large region. The shape of the jet transforms into a moon shape. Behind the jet a region with re-circulation is developed. For the S0610A and S0602A cross-section also regions of re-circulations are visible. However the jet is not as much effected by the surrounding flow in comparison to the S1010A cross-section. The shape of the S0602A flow is more compact in comparison to the S0610A and the S1010A cross-section. Overall it can be stated that the surrounding ship flow has an influence on the shape of the tunnel jet flow. The flow is moving to the back of the vessel, nevertheless the jet can be still recognized at a position y=1.1 [m] which is 2.75 D away from the outlet.

It is interesting to see that the development of the tunnel jet flow is completely different for Case 3.

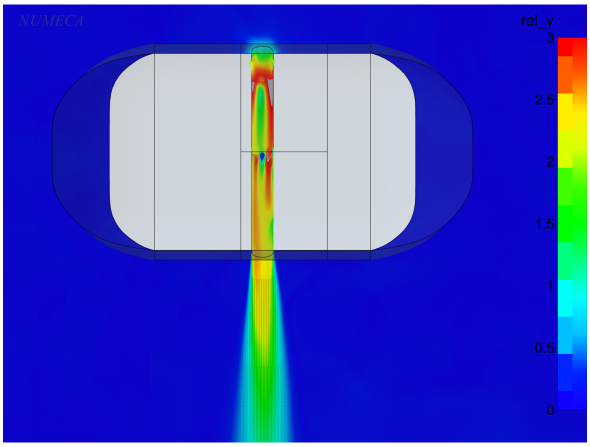

(a) Hopper wedge S1010A, Case 1

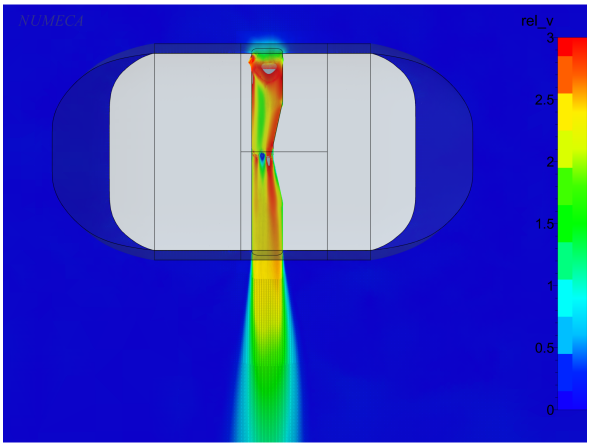

(b) Hopper wedge S0610A, Case 1

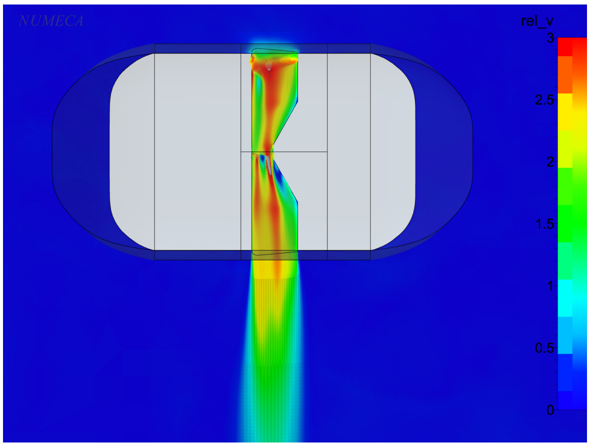

(c) Hopper wedge S0602A, Case 1

Figure 4.9: Systematic tunnel cross-section variation: Case 1. Ship velocity u_s=0 [m/s], normalized with u_s=0.318 [m/s]. Relative velocity v_{rel} in the xy-plane at z=0.1096 [m]. Topside of the wedge is inlet side and bottom the outlet side.

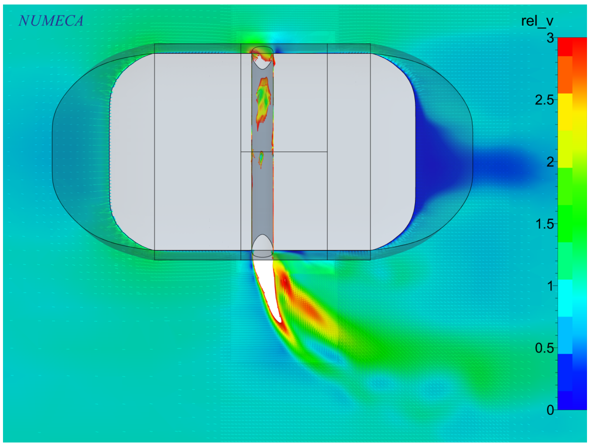

(a) Hopper wedge S1010A, Case 2

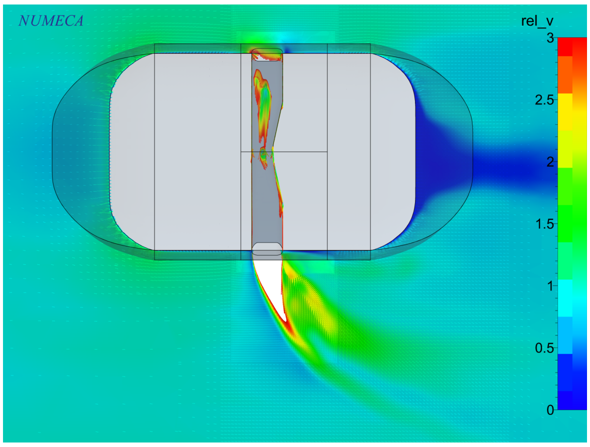

(b) Hopper wedge S0610A, Case 2

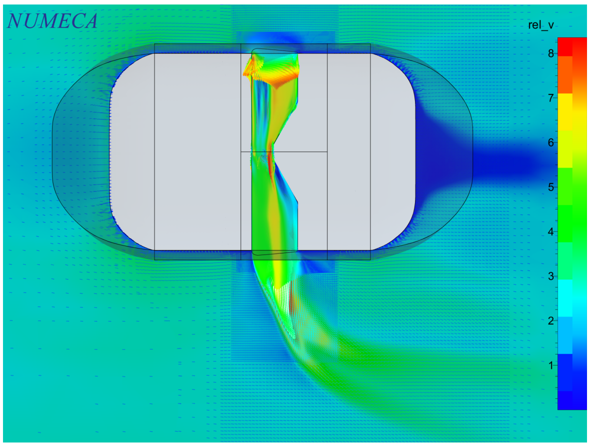

(c) Hopper wedge S0602A, Case 2

Figure 4.10: Systematic tunnel cross-section variation: Case 2. Ship velocity u_s=0.159 [m/s]. Relative velocity v_{rel} in the xy-plane at z=0.1096 [m]. Topside of the wedge is inlet side and bottom the outlet side.

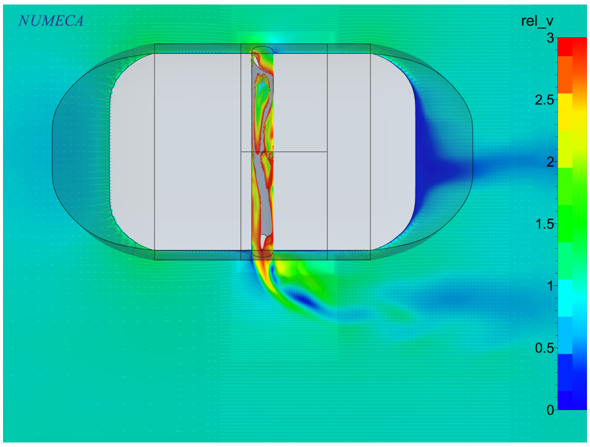

(a) Hopper wedge S1010A, Case 3

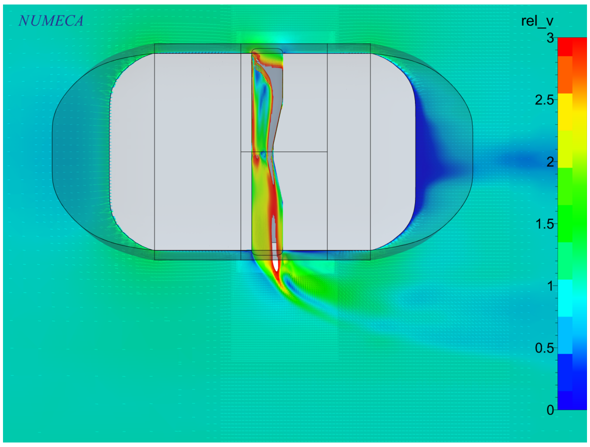

(b) Hopper wedge S0610A, Case 3

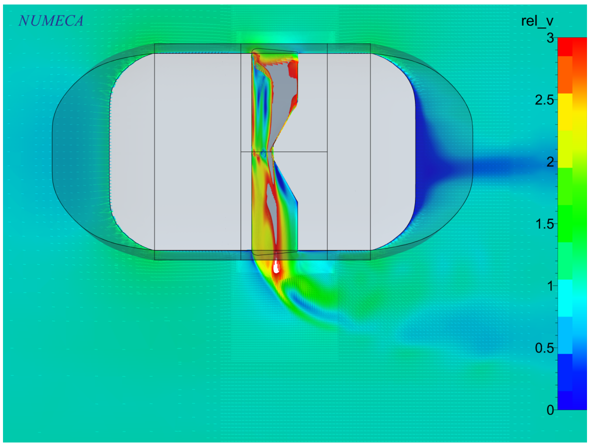

(c) Hopper wedge S0602A, Case 3

Figure 4.11: Systematic tunnel cross-section variation: Case 3. Ship velocity u_s=0.318 [m/s]. Relative velocity v_{rel} in the xy-plane at z=0.1096 [m]. Topside of the wedge is inlet side and bottom the outlet side.

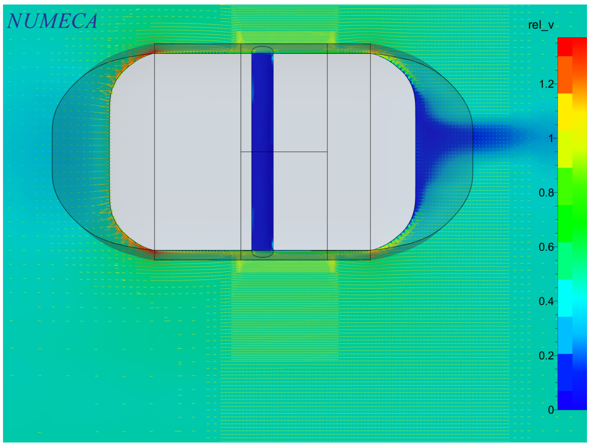

(a) Hopper wedge S1010A, Case 4

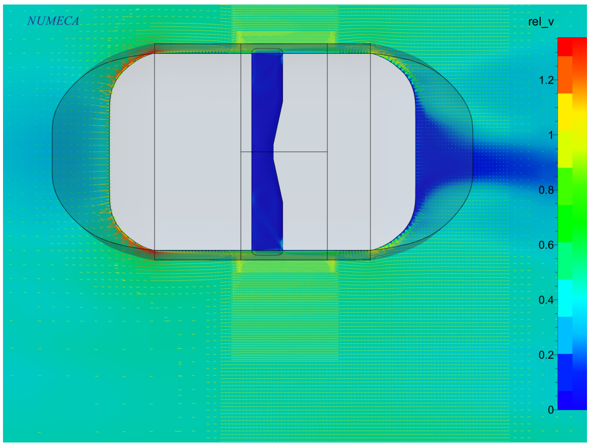

(b) Hopper wedge S0610A, Case 4

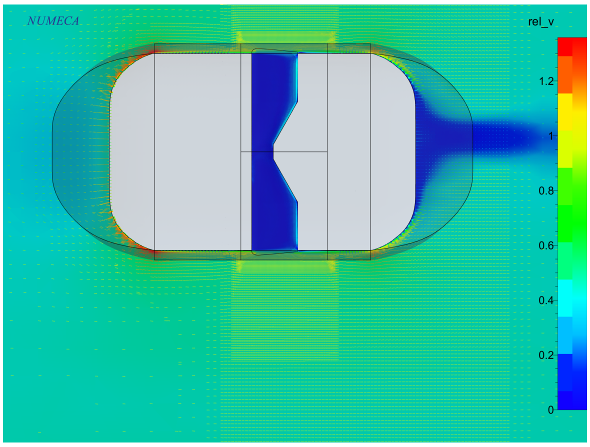

(c) Hopper wedge S0602A, Case 4

Figure 4.12: Systematic tunnel cross-section variation: Case 4. Ship velocity u_s=0.318 [m/s], no thrust. Relative velocity v_{rel} in the xy-plane at z=0.1096 [m]. Topside of the wedge is inlet side and bottom the outlet side.

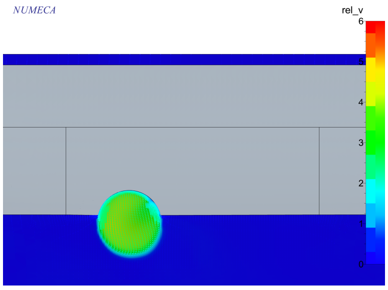

(a) Hopper wedge S1010A, Case 1, y=0.7 [m]

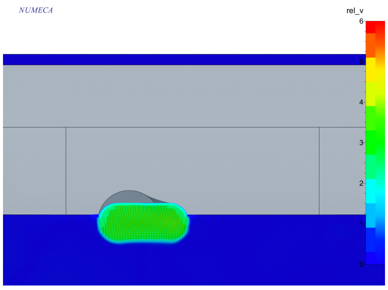

(b) Hopper wedge S0610A, Case 1, y=0.7 [m]

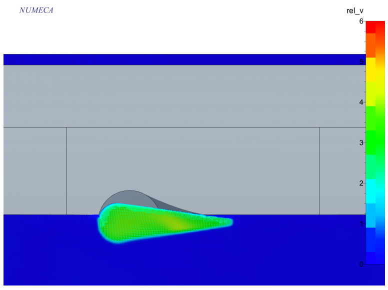

(c) Hopper wedge S0602A, Case 1, y=0.7 [m]

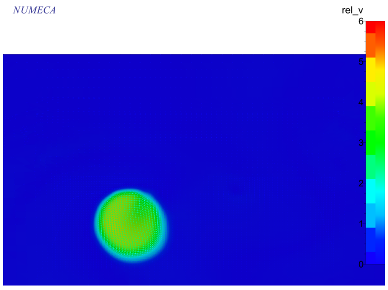

(d) Hopper wedge S1010A, Case 1, y=0.8 [m]

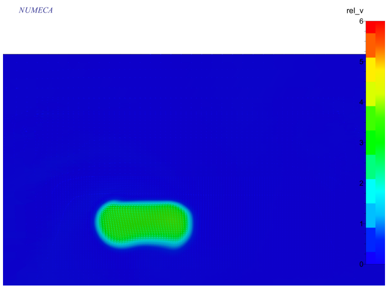

(e) Hopper wedge S0610A, Case 1, y=0.8 [m]

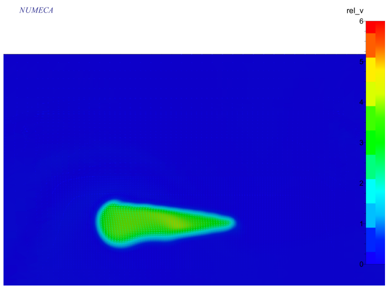

(f) Hopper wedge S0602A, Case 1, y=0.8 [m]

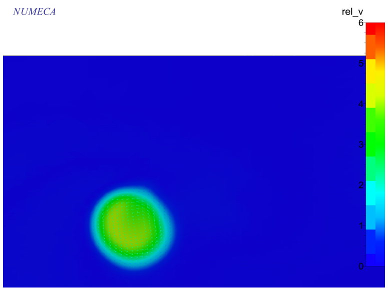

(g) Hopper wedge S1010A, Case 1, y=0.9 [m]

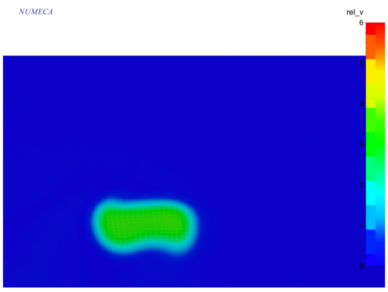

(h) Hopper wedge S0610A, Case 1, y=0.9 [m]

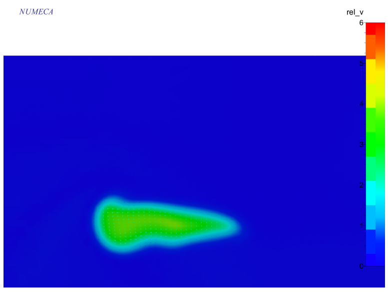

(i) Hopper wedge S0602A, Case 1, y=0.9 [m]

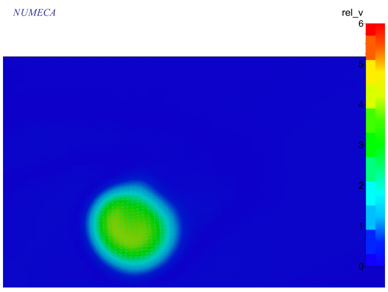

(j) Hopper wedge S1010A, Case 1, y=1.0 [m]

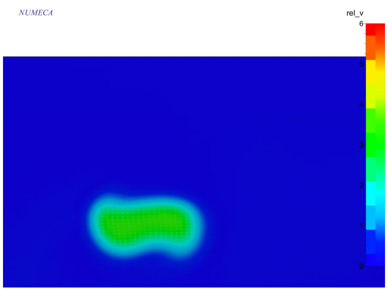

(k) Hopper wedge S0610A, Case 1, y=1.0 [m]

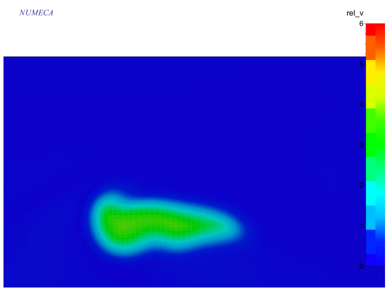

(l) Hopper wedge S0602A, Case 1, y=1.0 [m]

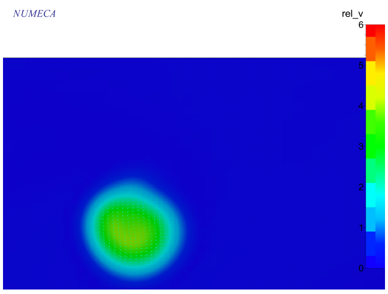

(m) Hopper wedge S1010A, Case 1, y=1.1 [m]

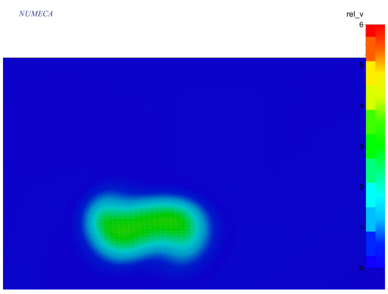

(n) Hopper wedge S0610A, Case 1, y=1.1 [m]

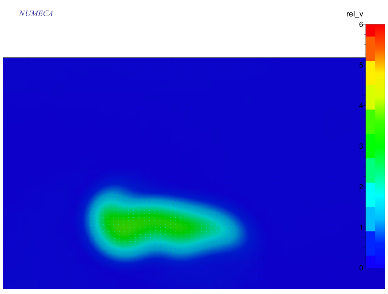

(o) Hopper wedge S0602A, Case 1, y=1.1 [m]

Figure 4.13: Development of the tunnel jet flow of Case 1. Cuts in the xz-plane at the given y-coordinate. The plot shows the magnitude of the tunnel jet velocity scaled by the ship speed u_s=0.318 [m/s].

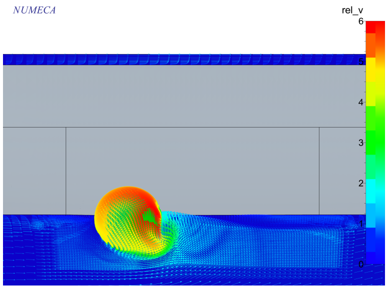

(a) Hopper wedge S1010A, Case 2, y=0.7 [m]

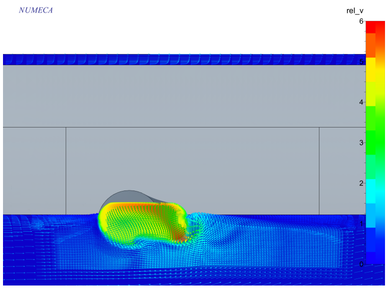

(b) Hopper wedge S0610A, Case 2, y=0.7 [m]

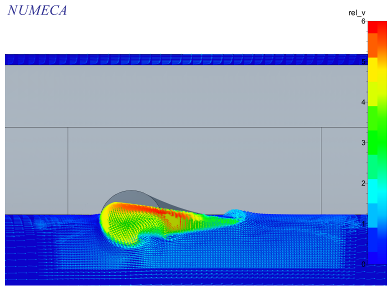

(c) Hopper wedge S0602A, Case 2, y=0.7 [m]

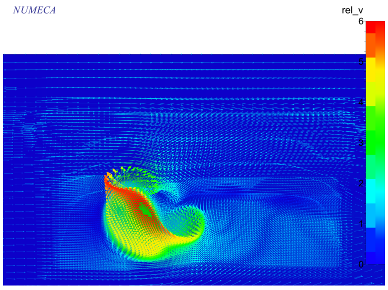

(d) Hopper wedge S1010A, Case 2, y=0.8 [m]

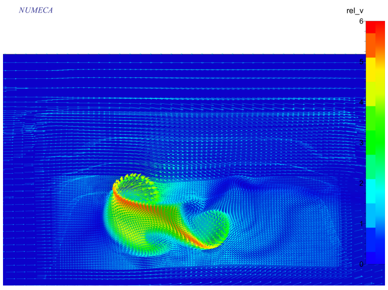

(e) Hopper wedge S0610A, Case 2, y=0.8 [m]

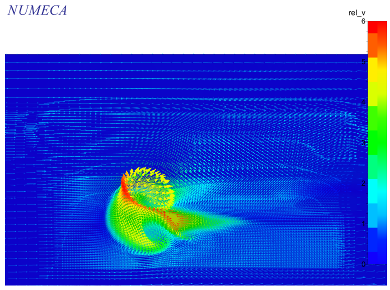

(f) Hopper wedge S0602A, Case 2, y=0.8 [m]

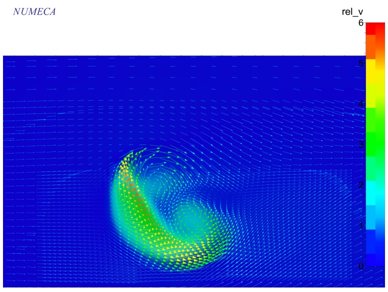

(g) Hopper wedge S1010A, Case 2, y=0.9 [m]

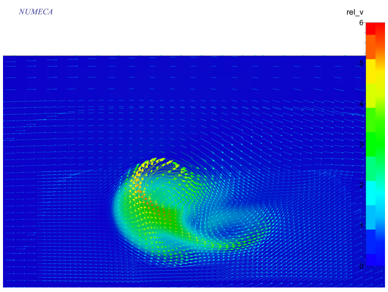

(h) Hopper wedge S0610A, Case 2, y=0.9 [m]

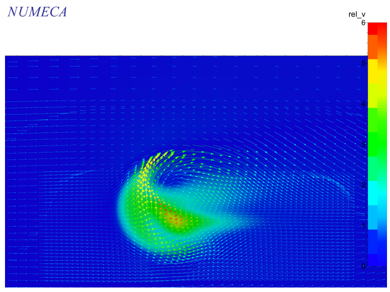

(i) Hopper wedge S0602A, Case 2, y=0.9 [m]

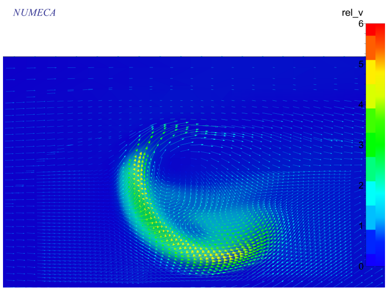

(j) Hopper wedge S1010A, Case 2, y=1.0 [m]

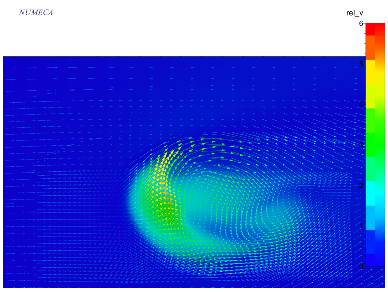

(k) Hopper wedge S0610A, Case 2, y=1.0 [m]

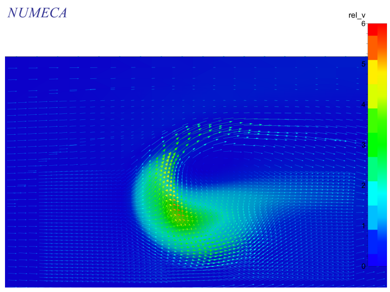

(l) Hopper wedge S0602A, Case 2, y=1.0 [m]

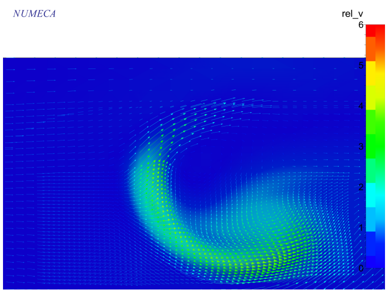

(m) Hopper wedge S1010A, Case 2, y=1.1 [m]

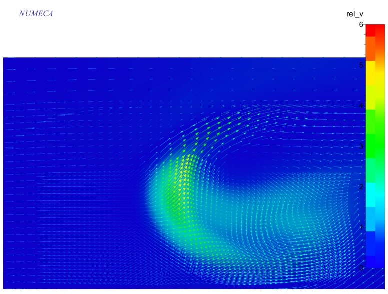

(n) Hopper wedge S0610A, Case 2, y=1.1 [m]

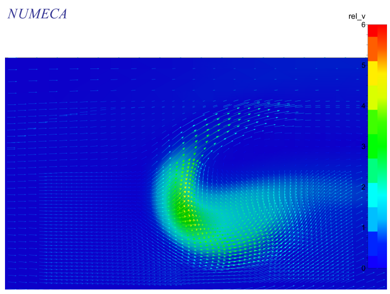

(o) Hopper wedge S0602A, Case 2, y=1.1 [m]

Figure 4.14: Development of the tunnel jet flow of Case 2. Cuts in the xz-plane at the given y-coordinate. The plot shows the magnitude of the tunnel jet velocity by the ship speed u_s=0.159 [m/s].

The fundamental difference between Case 2 and Case 3 is that for Case 2 the velocity ratio is in the strong jet region and for Case 3 in the weak jet region. Therefore a lot more influence of the ship flow on the tunnel jet flow is expected in Case 3 in comparison to Case 2. This can be seen in Figure 4.15. Close to the tunnel outlet the shape of the jet is as desired, but already a small distance away from the hull the jet is deformed by the surrounding flow. Large re-circulation occurs aft of the jet. The velocities of all three cross-section decrease fast with an increase in distance, and at 1.1 [m] from midship, 2.75 D from the outlet, the jet is not recognizable anymore for the S1010A cross-section, only a bit visible for the S0610A and is still good recognizable for the S0602A cross-section. This indicates that the S0602A cross-section bends at higher distance from the hull, in comparison to the other two cross-sections. Next to that the height of the region affected by the jet is smaller compared to the other cross-sections, however it should be remembered that the initial height for S0602A is also smaller than for the other two cross-section.

The comparison of the development of the tunnel jet flow has shown that there is a different behavior for a velocity ratio of 0.2 [-] (Case 2) and 0.4 [-] (Case 3). For Case 2 the flow is effected by the ship flow, but the core of the jet is still intact 2.75 D from the outlet, for Case 3 the interaction with the ship flow causes the jet to bend earlier and at 2.75 D from the outlet only small parts of the jet are still present. In general the S0602A seems to have the best flow behavior, based on this comparison as the jet is compacter and stays longer intact.

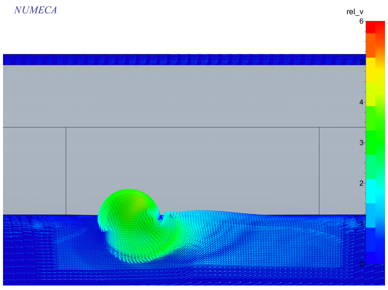

(a) Hopper wedge S1010A, Case 3, y=0.7 [m]

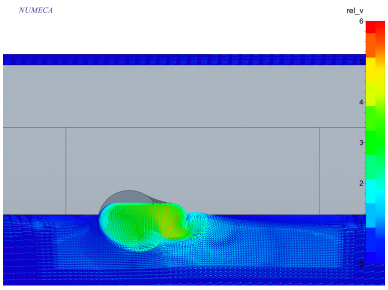

(b) Hopper wedge S0610A, Case 3, y=0.7 [m]

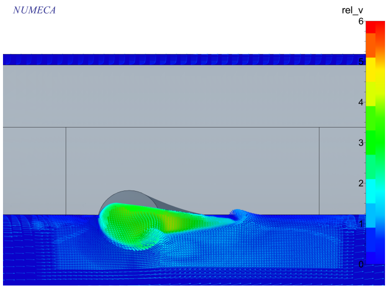

(c) Hopper wedge S0602A, Case 3, y=0.7 [m]

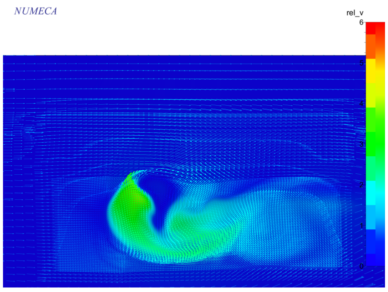

(d) Hopper wedge S1010A, Case 3, y=0.8 [m]

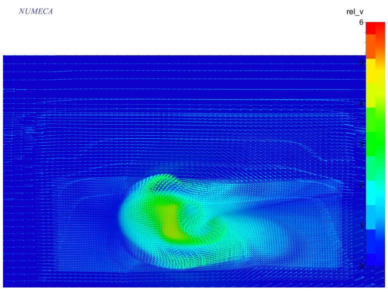

(e) Hopper wedge S0610A, Case 3, y=0.8 [m]

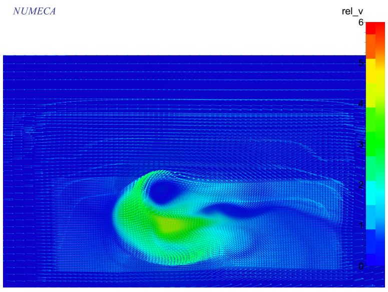

(f) Hopper wedge S0602A, Case 3, y=0.8 [m]

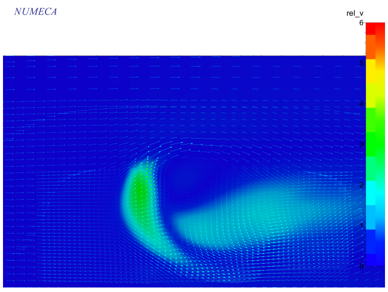

(g) Hopper wedge S1010A, Case 3, y=0.9 [m]

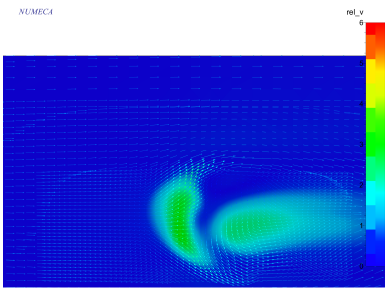

(h) Hopper wedge S0610A, Case 3, y=0.9 [m]

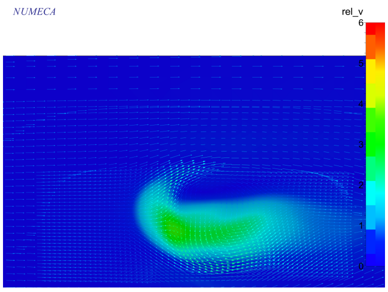

(i) Hopper wedge S0602A, Case 3, y=0.9 [m]

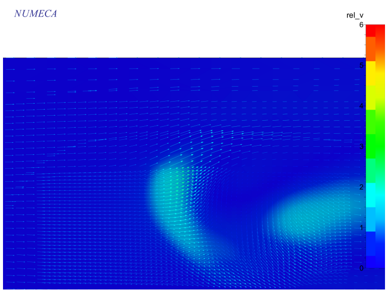

(j) Hopper wedge S1010A, Case 3, y=1.0 [m]

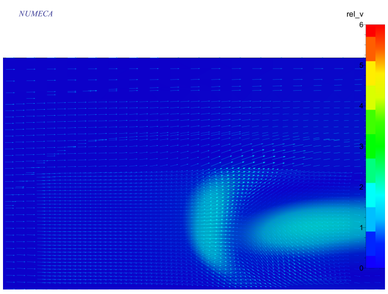

(k) Hopper wedge S0610A, Case 3, y=1.0 [m]

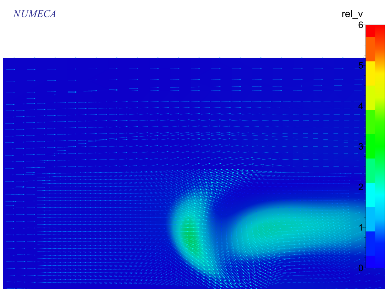

(l) Hopper wedge S0602A, Case 3, y=1.0 [m]

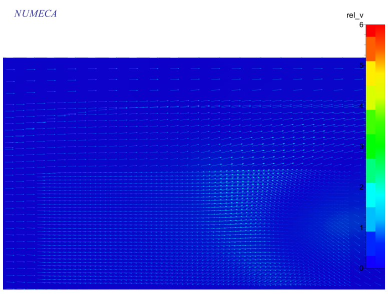

(m) Hopper wedge S1010A, Case 3, y=1.1 [m]

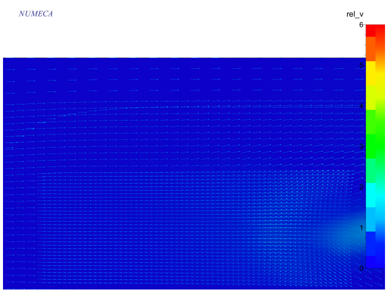

(n) Hopper wedge S0610A, Case 3, y=1.1 [m]

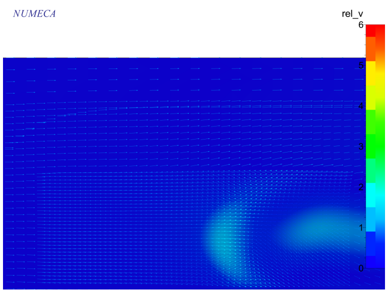

(o) Hopper wedge S0602A, Case 3, y=1.1 [m]

Figure 4.15: Development of the tunnel jet flow of Case 3. Cuts in the xz-plane at the given y-coordinate. The plot shows the magnitude of the tunnel jet velocity by the ship speed u_s=0.318 [m/s].

4.3.2. Quantitative

In Figure 4.16 the forces of the three different cross-sections are shown versus the velocity ratio m for Case 1,2 and 3. It can be seen that the tunnel jet speeds for S1010A, S0610A and S0602A are different. For the S0602A cross-section the velocities are a bit lower resulting in a higher velocity ratio m. The resistance (force in x-direction) is more or less comparable for the three cases, which means a change in cross-section has only a very small influence on the resistance, when the wedge is moving forward.

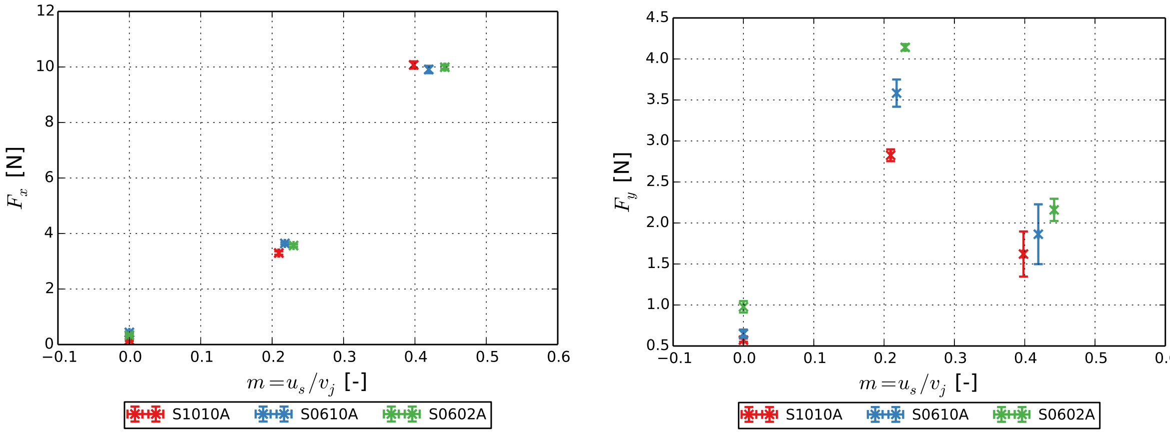

(a) F_x (b) F_y

Figure 4.16: Systematic tunnel cross-section variation:: Forces versus non dimensional velocity ratio m. The errorbar shows one standard deviation of the force from the time trace.

For Case 3 an increase in force in the y-direction is noticed for S0602A in comparison to S1010A and S0610A (Compare Table 4.6). This increase is 33 and 16 [%] respectively. In Case 4 the resistance of the wedge for the three cross-section is computed. It can be seen that the resistance of the three cross-sections is comparable, however the resistance for S0602A is the highest. The influence of the jet on the resistance is 46 [%] for S1010A, 45 [%] for S0610A and 43 [%] for S0602A. From this it can be concluded that for this case the overall resistance for the S0602A is increased when the thruster is off, when the thruster is operating the resistance of all three cross-sections is close together.

Table 4.6: Result of cross-section variation. The calculated mean μ and standard deviation σ are based on the measuring section of 1.5 L.

		m	F_x		F_y	
Case	Model	[-]	μ [N]	σ [N]	μ [N]	σ [N]
1	S1010A	0	0.16	0.028	0.57	0.020
1	S0610A	0	0.44	0.010	0.65	0.051
1	S0602A	0	0.34	0.020	0.98	0.070
2	S1010A	0.21	3.30	0.063	2.83	0.072
2	S0610A	0.22	3.64	0.041	3.58	0.166
2	S0602A	0.23	3.57	0.045	4.41	0.039
3	S1010A	0.40	10.07	0.129	1.62	0.275
3	S0610A	0.42	9.91	0.133	1.86	0.365
3	S0602A	0.44	10.00	0.058	2.16	0.136
4	S1010A	∞	5.44	0.119	0.75	0.096
4	S0610A	∞	5.42	0.077	0.69	0.038
4	S0602A	∞	5.67	0.078	0.47	0.036

For the Nienhuis wedge the tunnel speed ratio $v_T = \frac{v_j(u_s)}{v_j(0)}$ has been calculated and an interesting trend was found. In Figure 4.17 the same plots as for the Nienhuis wedge have been created. All three cross-sections show different values. The values for a cylindrial cross-section S1010A are the highest, followed by S0610A and S0602A. This means that the tunnel speed ratio is not as high as for the Nienhuis wedge and therefore the tunnel jet speed is increased only up to 9 [%] for the S1010A, 5 [%] for the S0610A and about 2 [%] for the S0602A cross-section. For the Nienhuis wedge at a speed ratio m of 0.4 [-] an increase of more than 10 [%] was recognized. This difference can be explained with the long tunnel of the hopper wedge and the change in cross-section of the tunnel.

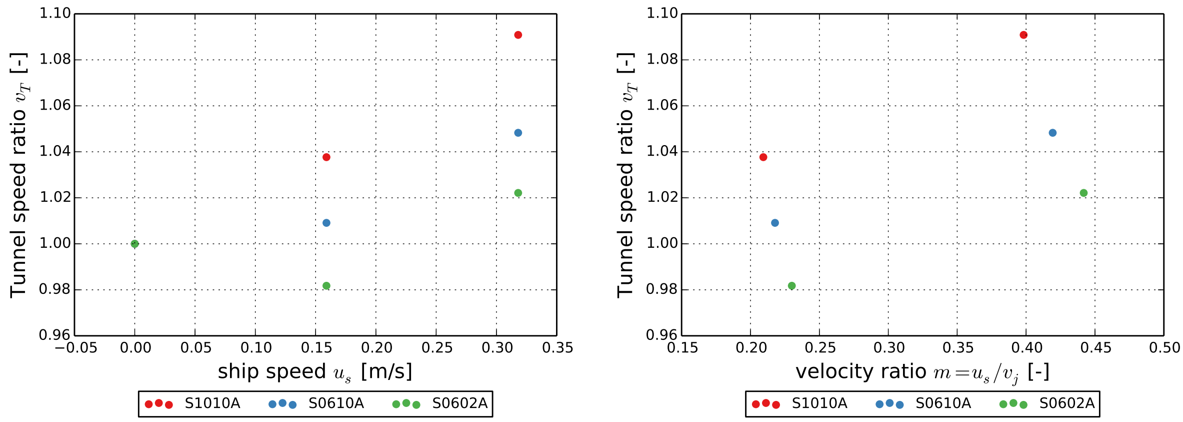

(a) Function of wedge speed u_s

(b) Function of velocity ratio m

Figure 4.17: Tunnel speed ratio v_T as function of the wedge speed and the velocity ratio for the cross-section variation.

It was already stated that the tunnel jet speed is lower for the S0602A cross-section in comparison to the other two cross-sections. Therefore the tunnel jet speed v_j is compared with the hydraulic diameter D_h. Where the hydraulic diameter is defined as [3]:

$$D_H = \frac{4A}{P} \tag{4.6}$$

In Figure 4.18 the axis are normalized with the value from the S1010A computations and for each cross-section two cases (Case 2 and 3) are considered. The datapoints S1010A are by definition equal for both cases. The figure indicates that the tunnel jet velocity is dependent on the hydraulic diameter. This is inline with pipe flow theory, where the hydraulic diameter is a important parameter in characterizing the flow. The differences between the datapoints of a cross-section are probably due to the speed ratio m.

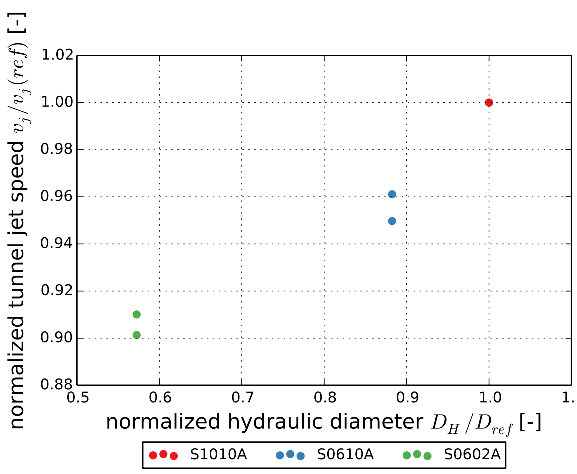

Figure 4.18: Relation between the hydraulic diameter and the tunnel jet speed for Case 2 and 3.

The comparison of three different cross-sections has shown that a S0602A is an interesting alternative to the used cross-sections S1010A and S0610A. The force on the ship increases significantly due to the change in cross-sectional shape. The flow bends later and the jet is maintained better. On the downside an increase in resistance was noticed. Next to that a decrease of the tunnel jet speed and a dependency with the hydraulic diameter has been shown.

5

Conclusions and Recommendations

In this thesis a computational fluid dynamics (CFD) study on the performance of bow tunnel thrusters is performed for the Nienhuis wedge, based on a container ship, and the Hopper wedge, based on a trailing suction hopper dredger. All presented conclusions are based on the described geometries and computations.

5.1. Conclusions

The conclusions are split in three categories: general, conclusions based on the Nienhuis wedge and conclusions based on the Hopper wedge.

General conclusions The flow through the tunnel and the flow around the ship are comparable to the flow of a jet in a cross-flow. The tunnel jet interacts with the ship flow, dependent on the velocity ratio m. For strong jets ($m \approx 0.2$ [-]) the tunnel jet flow forces the ship flow to decelerate and to flow around the jet. The jet itself is bent at a distance from the tunnel outlet toward the back of the vessel. For a weak jet ($m \approx 0.4$ [-]) the jet is pushed by the ship flow towards the back of the ship. The jet speed decelerates quickly with an increase in distance to the tunnel outlet. The jet is bent close to the hull towards the back of the ship. Both has been reported also by [1] and [4].

The resistance of the wedge is increased with an increase in thrust of the tunnel thruster. The tunnel jet increases the resistance, as the ship flow is decelerated by the jet. The increase in resistance is significant for this study (around 50 [%]). The same effect is described by Nienhuis [1] as well.

The transverse forces on the wedge are low for the zero speed case, where the wedge is at rest and the tunnel thruster is operating. The obtained forces do not agree with trends reported in literature [1], [4], [25].

In this study the hub and strut of the bow tunnel thruster are not modeled, but they do have an influence on the side force on the wedge. It is therefore advised to model the hub and strut in future CFD studies on this subject.

In the study an actuator disk is used to model the tunnel thruster in CFD. It was concluded that torque needs to be included, to add rotation to the flow, which is present in real life. Next to that a uniform distribution is used, it is expected that the distribution of the actuator disk has only a minor effect on the resulting forces on the wedge. However it is advised to use either a distribution based on a propeller in a tunnel or to use a sliding grid and model the propeller.

Conclusions based on the Nienhuis wedge A grid study gives large numerical uncertainties for two cases using the method of Eça and Hoekstra. The cases are the zero speed case, where the wedge has zero speed and the tunnel thruster is operating and the base case, where the wedge is moving at Froude number 0.058 [-] and the tunnel thruster is operating. It is assumed that the large uncertainties are partly due to the small magnitude of measured forces, which are caused by the chosen length scale.

A qualitative comparison of the velocity profile of the tunnel jet with theory shows, that the tunnel jet is asymmetric. It is shown that this is caused by the direction of the applied torque within the actuator disk and by the form of the wedge.

A qualitative comparison with a jet in a cross-flow experiment shows that the computations are qualitative valid and that a jet in a cross-flow description is a good description of the tunnel jet flow at slow forward motion.

A quantitative validation with model tests of Nienhuis for the zero speed case shows that the results are not quantitative valid. A large disagreement between the model tests and the CFD results is found.

A quantitative comparison with literature shows that the trends reported in literature are not observed in the CFD results. It is assumed that the low transverse force for the zero speed case has a negative effect on the observed trend.

A quantitative comparison with an other CFD study by MARIN [7] shows that the results are similar and within the uncertainty of each other.

A dependency between the normalized tunnel jet speed and the speed ratio m for the Nienhuis wedge is found. The results indicate a trend that has a local maximum at a speed ratio m of 0.4 [-]. At this local maximum the normalized tunnel speed is increased by more than 10 [%] in comparison to the normalized tunnel speed for the zero speed case.

Conclusions based on the Hopper wedge The three tunnel layouts are suitable to direct the tunnel flow in the defined shape of the cross-sections for the cross-sections tested. At the zero speed case the shape of the cross-section remains nearly unchanged at far distances to the hull

The wake region behind the tunnel jet is decreased for the streamlined cross-section (S0602A) in comparison with the other two cross-sections.

The streamlined cross-section (S0602A) increases the transverse force at slow forward speed, in comparison with not-streamlined cross-sections S0610A and S1010A. For m=0.2 [-] an increase of more than 50 [%] has been found for a streamlined cross-section (S0602A) in comparison with a circular cross-section (S1010A), at m=0.4 an increase of more than 30 [%] is found. The results are outside the errorbar of each other, however the numerical uncertainty is higher than the mentioned increases.

The streamlined cross-section (S0602A) increases also the resistance of the wedge, in comparison to the other cross-sections. For the case tested (Froude number 0.058 [-]) the difference is 4 [%] in comparison to the other cross-sections.

It is concluded that a streamlined tunnel cross-section is a viable alternative to circular tunnel cross-sections, because the flow is improved and a positive effect on the side force is recognized. However more research is needed, especially the resistance increase needs to be studied in more detail and the numerical uncertainties need to be decreased.

5.2. Recommendations

During the study multiple effects were noticed, that require more research these are:

Effect of the actuator disk distribution In this thesis a constant actuator disk distribution has been used. The distribution is however different to a distribution of a ducted propeller. It is therefore advised to use a distribution that is based on results of a open-water test of a propeller in a tunnel. This could be done by using measurements of the propeller distribution on a ship, on model-scale during model testing or by using a sliding-grid method in CFD. It is expected that the effect of the actuator disk distribution on the overall trend is minor.

Modeling of the hub and strut of the thruster In this thesis the hub and strut of the thruster is not modeled in the CFD model. During comparison between the model used in the model test by Nienhuis [1] and the model used in this CFD study it is concluded that the hub and strut have an influence on the side force. Next to that the reaction force of the actuator disk is not exceeded on the wedge in the CFD study. It is therefore advised to model the hub and strut and include the reaction force on the wedge in the computation.

Constant thrust assumption In this thesis the thrust used in the actuator disk is kept constant. Measurements by Nienhuis [1] however indicate that the thrust is dependent on the wedge velocity. It is recommended to perform CFD computations with a sliding grid and a modeled propeller inside the tunnel.

During the computations the rotational speed should be kept constant, as this is in accordance with the actual situation inside a ship.

Increase in tunnel jet velocity as function of the speed ratio m In this study it is recognized for the Nienhuis wedge that a dependency between the velocity inside the tunnel and the speed ration m exists. For the Hopper wedge, this effect is significantly less. This is due to an increase in tunnel length, which decreases the velocity inside the tunnel and due to the variation in cross-sectional shape. It is interesting if this effect is recognized in other situations. Therefore it is advised to study this effect both numerically and using measurement at model and full scale.

Quantitative validation It is advised to test the hopper wedge with the three presented cross-sections in model tests. During such tests it is interesting to study the time traces of the measured forces and the measured flow field.

More variations using the systematic cross-section approach In this thesis three cross-section variations have been compared. It is advised to perform an in-depth study using various cross-sections and compare the results to find an optimum cross-section.

Effect of the hull shape The wedges used in this study are developed to simplify the hull of a real ship. The straight sides of the wedge are not present in the bow section of a trailing suction hopper wedges. It is interesting how a change in cross-section is affected by the form of the bow. Therefore it is advised to perform a study where the systematic cross-section variation is applied to a ship hull, both numerically and using measurements at model and full scale.

Scale effects In this thesis all computations are performed on model scale. This is done, because model test results are available for validation. It is known that scale effects between model scale and full scale exist. An in-depth study int multiple aspects such as: viscous effects, influence on forces and fluctuation of the flow is advised.

Perform study on influencing parameters In this study only the cross-section of the bow tunnel thruster is varied. It is interesting to study other influencing parameters as well. These parameters are: number of tunnels, position of the tunnel with in the vertical direction, tunnel-hull intersection, length of the tunnel, grid bars, angle of the hull raising at the intersection with the tunnel thruster, angle of the tunnel outlet with the surrounding flow. As explained in the Definition study [3] many studies exists on these parameters, however most of them are outdated and do not focus on slow forward motion, but on a ship at with zero speed.

Install a streamlined cross-section in a newbuild dredger It would be great to apply a streamlined cross-section in the design stage of a hopper dredger newbuilding project. It is assumed that the tunnel thruster will still perform well at no forward speed and this study has shown that an increase in transverse force is possible due to a change in cross-sectional shape of the tunnel.

A

Equations of the SST-Menter k-ω turbulence model

In this appendix the equations of the SST-Menter k-ω model are given. All equations are adopted from the ISIS-CFD theoretical manual [10, 2.3.2].

The eddy viscosity μ_t is defined using the turbulent kinetic energy K and the dissipation rate of the turbulent frequency ω as:

$$\mu_t = \frac{\frac{\rho K}{\omega}}{max\left\{1, \frac{\Omega F_2}{a_1 \omega}\right\}} \tag{A.1}$$

Where ρ is the density, F_2 is an auxiliary function, a_1 is taken as 0.31 [-] and the absolute value of the vorticity Ω. The auxiliary function is defined with the wall distance d as:

$$F_2 = \tanh\left(\left[max\left\{2\frac{\sqrt{K}}{0.009 d\omega}, \frac{500\mu}{\rho d^2 \omega}\right\}\right]^2\right) \tag{A.2}$$

A blending function F_1 is used to blend between the k-ω and the k-ϵ model:

$$F_1 = \tanh\left(\left[min\left\{max\left\{\frac{\sqrt{K}}{0.09 d\omega}, \frac{500\mu}{\rho d^2 \omega}\right\}, \frac{4\rho\sigma_{\omega 2}\kappa}{CD_{\kappa\omega} d^2}\right\}\right]^4\right) \tag{A.3}$$

With:

$$CD_{\kappa\omega} = max\left\{\frac{2\rho\sigma_{\omega 2}}{\omega}\frac{\partial K}{\partial x_j}\frac{\partial \omega}{\partial x_j}, 10^{-20}\right\} \tag{A.4}$$

The two transport equations are defined as:

$$\frac{\partial \rho K}{\partial t} + \frac{\partial}{\partial x_j}\left(\rho U_j K - (\mu + \sigma_k \mu_t)\frac{\partial K}{\partial x_j}\right) = \tau_{tij} S_{ij} - \beta^* \rho \omega K \tag{A.5}$$

$$\frac{\partial \rho \omega}{\partial t} + \frac{\partial}{\partial x_j}\left(\rho U_j \omega - (\mu + \sigma_\omega \mu_t)\frac{\partial \omega}{\partial x_j}\right) = P_\omega - \beta\rho\omega^2 + 2\left(1 - F_1\right)\frac{\rho\sigma_{\omega 2}}{\omega}\frac{\partial K}{\partial x_j}\frac{\partial \omega}{\partial x_j} \tag{A.6}$$

The production term of ω is defined as:

$$P_\omega = 2\gamma\rho\left(S_{ij} - \frac{\omega S_{nn}\delta_{ij}}{3}\right)S_{ij} \tag{A.7}$$

The constants of the SST k-ω model are:

$$a_1 = 0.31 \qquad \beta^* = 0.09 \qquad \kappa = 0.41 \tag{A.8}$$

The coefficients of the k-ω model are denoted ϕ_1, of the k-ϵ model as ϕ_2 and are blended as follows:

$$\phi = F_1\phi_1 + (1 - F_1)\phi_2 \qquad \text{where } \phi = \{\beta, \gamma, \sigma_k, \sigma_\omega\} \tag{A.9}$$

The constants are shown in Table A.1.

Table A.1: Constants used in the blending of coefficients of the SST Menter k-ω model. Adapted from [10].

Coefficient	ϕ_1 (k-ω model)	ϕ_2 (k-ϵ model)
σ_k [-]	0.85	1.00
σ_ω [-]	0.500	0.856
β [-]	0.0750	0.0828
$\gamma = \frac{\beta_1}{\beta^*} - \frac{\sigma_\omega \kappa^2}{\sqrt{\beta^*}}$ [-]	0.553	0.440

B

Discretization error according to Eça and Hoekstra

In this appendix the method of Eça and Hoekstra to determine the discretization error of a grid study is presented. All steps and equations are adapted from [17].

In order to follow this procedure it is assumed that at least 4 grids ($n_g \geq 4$) have been calculated, that the number of cells (N_i) and a flow parameter (ϕ_i) of all grids are known. First the typical cell size h_i is calculated as:

$$h_i = \left(\frac{1}{N_i}\right)^{\frac{1}{n}} \tag{B.1}$$

Based on the typical cell size the weights w_i and nw_i are defined as followed:

$$w_i = 1 \quad \text{and } nw_i = 1 \quad \text{(non-weighted approach)} \tag{B.2}$$

$$w_i = \frac{\frac{1}{h_i}}{\sum_{i=1}^{n_g} \frac{1}{h_i}} \quad \text{and } nw_i = n_g w_i \quad \text{(weighted approach)} \tag{B.3}$$

It should be noticed that the sum of all weights for the weighted approach yields to 1:

$$\sum_{i=1}^{n_g} w_i = 1 \tag{B.4}$$

B.1. Single term expansion with unknown order of grid convergence

The equation

$$\delta_{RE} = \alpha h_i^p \tag{B.5}$$

is solved using least squares with and without weights. The least square of Equation B.5 means to minimize the function:

$$S_{RE}\left(\phi_o, \alpha, p\right) = \sqrt{\sum_{i=1}^{n_g} w_i \left(\phi_i - \left(\phi_o + \alpha h_i^p\right)\right)^2} \tag{B.6}$$

Taking the partial derivatives of all three unknowns results in the following non-linear equations:

$$\phi_o = \sum_{i=1}^{n_g} w_i \phi_i - \alpha \sum_{i=1}^{n_g} w_i h_i^p \tag{B.7}$$

$$\alpha = \frac{\sum_{i=1}^{n_g} w_i \phi_i h_i^p - \left(\sum_{i=1}^{n_g} w_i \phi_i\right)\left(\sum_{i=1}^{n_g} w_i h_i^p\right)}{\sum_{i=1}^{n_g} w_i h_i^{2p} - \left(\sum_{i=1}^{n_g} w_i h_i^p\right)\left(\sum_{i=1}^{n_g} w_i h_i^p\right)} \tag{B.8}$$

$$\sum_{i=1}^{n_g} w_i \phi_i h_i^p \log(h_i) - \phi_o \sum_{i=1}^{n_g} w_i h_i^p \log(h_i) - \alpha \sum_{i=1}^{n_g} w_i h_i^{2p} \log(h_i) = 0 \tag{B.9}$$

To solve these non-linear equations numerically the secant method is used [31]. The minimum of the function has a standard deviation of:

$$\sigma_{RE} = \sqrt{\frac{\sum_{i=1}^{n_g} n w_i \left(\phi_i - (\phi_o + \alpha h_i^p)\right)^2}{(n_g - 3)}} \tag{B.10}$$

After this step we have two values for δ_{RE}, p and σ_{RE} one from the non-weighted approach and one form the weighted approach. If any of the values of p satisfies: $0.5 \leq p \leq 2.0$, then the error estimate ϵ_ϕ is equal to the corresponding fit δ_{RE} ($\epsilon_\phi = \delta_{RE}$). If both values of p satisfy this criteria, the value of δ_{RE} with the smallest standard deviation σ_{RE} is selected. For all other cases a single term expansion with first-order term and a single term with second-order term needs to be calculated. If $p < 0.5$ a two-term expansion with first and second-order terms is needed additionally.

B.2. Single term expansion with first-order term

The single term expansion with first-order term is defined as:

$$\delta_1 = \alpha h_i \tag{B.11}$$

The least square function for this function is:

$$S_1(\phi_o, \alpha) = \sqrt{\sum_{i=1}^{n_g} w_i \left(\phi_i - (\phi_o + \alpha h_i)\right)^2} \tag{B.12}$$

Taking the partial derivatives of the function yields to the following system of linear equations:

$$\begin{bmatrix} 1 & \sum_{i=1}^{n_g} w_i h_i \\ \sum_{i=1}^{n_g} w_i h_i & \sum_{i=1}^{n_g} w_i h_i^2 \end{bmatrix} \begin{bmatrix} \phi_o \\ \alpha \end{bmatrix} = \begin{bmatrix} \sum_{i=1}^{n_g} w_i \phi_i \\ \sum_{i=1}^{n_g} w_i \phi_i h_i \end{bmatrix} \tag{B.13}$$

The corresponding standard deviation is:

$$\sigma_1 = \sqrt{\frac{\sum_{i=1}^{n_g} n w_i \left(\phi_i - (\phi_o + \alpha h_i)\right)^2}{(n_g - 2)}} \tag{B.14}$$

B.3. Single term expansion with second-order term

The single term expansion with second-order term is defined as:

$$\delta_2 = \alpha h_i^2 \tag{B.15}$$

The least square function for this function is:

$$S_2(\phi_o, \alpha) = \sqrt{\sum_{i=1}^{n_g} w_i \left(\phi_i - (\phi_o + \alpha h_i^2)\right)^2} \tag{B.16}$$

Taking the partial derivatives of the function yields to the following system of linear equations:

$$\begin{bmatrix} 1 & \sum_{i=1}^{n_g} w_i h_i^2 \\ \sum_{i=1}^{n_g} w_i h_i^2 & \sum_{i=1}^{n_g} w_i h_i^4 \end{bmatrix} \begin{bmatrix} \phi_o \\ \alpha \end{bmatrix} = \begin{bmatrix} \sum_{i=1}^{n_g} w_i \phi_i \\ \sum_{i=1}^{n_g} w_i \phi_i h_i^2 \end{bmatrix} \tag{B.17}$$

The corresponding standard deviation is:

$$\sigma_2 = \sqrt{\frac{\sum_{i=1}^{n_g} n w_i \left(\phi_i - (\phi_o + \alpha h_i^2)\right)^2}{(n_g - 2)}} \tag{B.18}$$

B.4. Two-term expansion with first and second-order term

The two term expansion with first and second-order term is defined as:

$$\delta_{12} = \alpha_1 h_i + \alpha_2 h_i^2 \tag{B.19}$$

The least square function for this function is:

$$S_{12}(\phi_o, \alpha) = \sqrt{\sum_{i=1}^{n_g} w_i \left(\phi_i - (\phi_o + \alpha_1 h_i + \alpha_2 h_i^2)\right)^2} \tag{B.20}$$

Taking the partial derivatives of the function yields to the following system of linear equations:

$$\begin{bmatrix} 1 & \sum_{i=1}^{n_g} w_i h_i & \sum_{i=1}^{n_g} w_i h_i^2 \\ \sum_{i=1}^{n_g} w_i h_i & \sum_{i=1}^{n_g} w_i h_i^2 & \sum_{i=1}^{n_g} w_i h_i^3 \\ \sum_{i=1}^{n_g} w_i h_i^2 & \sum_{i=1}^{n_g} w_i h_i^3 & \sum_{i=1}^{n_g} w_i h_i^4 \end{bmatrix} \begin{bmatrix} \phi_o \\ \alpha_1 \\ \alpha_2 \end{bmatrix} = \begin{bmatrix} \sum_{i=1}^{n_g} w_i \phi_i \\ \sum_{i=1}^{n_g} w_i \phi_i h_i \\ \sum_{i=1}^{n_g} w_i \phi_i h_i^2 \end{bmatrix} \tag{B.21}$$

The corresponding standard deviation is:

$$\sigma_{12} = \sqrt{\frac{\sum_{i=1}^{n_g} n w_i \left(\phi_i - (\phi_o + \alpha_1 h_i + \alpha_2 h_i^2)\right)^2}{(n_g - 3)}} \tag{B.22}$$

B.5. Selection of the error estimate

Depending on the observed order of grid convergence p one has four or six additional fits. The error estimate ϵ_ϕ is obtained from the fit that has the smallest standard deviation σ. In Table B.1 an overview of the selection of the error estimate is shown:

Table B.1: Overview on the equations to solve and error estimation based on the condition of the observed order of grid convergence p

Condition of p	Equations to solve	Error estimate based on
$0.5 \leq p \leq 2$	2 (δ_{RE})	min(σ_{RE})
$p > 2$	6 ($\delta_{RE}, \delta_1, \delta_2$)	min(σ_1, σ_2)
$p < 0.5$	8 ($\delta_{RE}, \delta_1, \delta_2, \delta_{12}$)	min($\sigma_1, \sigma_2, \sigma_{12}$)

B.6. Calculating the uncertainty

From the selection of the error estimate the order of grid convergence p, the standard deviation of the best fit σ, the error estimate for each grid $\epsilon_\phi(\phi_i)$ and the estimated value based on the fit $\phi_{fit} = \phi_o + \epsilon_\phi(\phi_i)$ are known. To access the quality of the fit a data range parameter $\Delta\phi$ is defined as:

$$\Delta_\phi = \frac{(\phi_i)_{max} - (\phi_i)_{min}}{n_g - 1} \tag{B.23}$$

If the solution is monotonically convergent ($0.5 \leq p < 2.1$) and if $\sigma < \Delta_\phi$ then the error estimation is considered reliable and a safety factor of $F_S = 1.25$ [-] is chosen. If the solution doesn't fulfil the requirement a safety factor of $F_s = 3.0$ [-] is chosen. Finally the uncertainty U_ϕ with a 95[%] confidence interval is then defined as:

$$U_\phi(\phi_i) = \begin{cases} F_S \epsilon_\phi(\phi_i) + \sigma + |\phi_i - \phi_{fit}| & \text{for } \sigma < \Delta_\phi \\ 3\frac{\sigma}{\Delta_\phi}\left(\epsilon_\phi(\phi_i) + \sigma + |\phi_i - \phi_{fit}|\right) & \text{for } \sigma \geq \Delta_\phi \end{cases} \tag{B.24}$$

C
Mesh settings

In this appendix the mesh settings and python script to generate the meshes are shown. This appendix is divided in two sections one for the Nienhuis wedge and one for the Hopper wedge.

C.1. Nienhuis wedge

During the nienhuis wedge study multiple grids have been used. In Table C.1 all used meshes are defined, set-up refers to the approach of dealing with the free surface, $y+$ is the dimensionless first layer thickness that is used to calculate the viscous layer thickness and r is the scaling parameter of the mesh, that is varied during the grid refinement study.

Table C.1: Overview of the used meshes for the Nienhuis wedge

					Number of initial cells			
Mesh name	Number of Cells	set-up	$y+$	r	$x_{initial}$	$y_{initial}$	$z_{initial}$	internal name
Set-up 1	3944321	1	30	2	30	18	18	casec_mesh_a
Set-up 2	594416	2	30	2	30	18	18	cased_mesh_a
Set-up 3	585549	3	30	2	30	18	18	casee_mesh_a
Set-up 4	564196	4	30	2	30	18	18	casef_mesh_a
mesh a	1099699	4	1	2	30	18	18	caseh_mesh_a
mesh b	444769	4	1	1	15	9	9	caseh_mesh_b
mesh c	1967995	4	1	3	45	27	27	caseh_mesh_c
mesh d	3242320	4	1	4	60	36	36	caseh_mesh_d
mesh e	4902549	4	1	5	75	45	45	caseh_mesh_e
mesh f	6998258	4	1	6	90	54	54	caseh_mesh_f

C.1.1. Python script for the Nienhuis wedge

In the following the script for mesh A, set-up 4 is shown for the Nienhuis wedge. The script can be executed directly in Numeca FineMarine. For more details on the Python syntax of Numeca, please read the Hexpress Manual [19].

```
igg_script_version(2.1)

## Define refinement settings
Ref_gen=12 #general refinement settings
Ref_a=5 #top parts
Ref_b=6 # hull
Ref_c=3 # free surface
```

```
Ref_d=7 # TT section
Ref_e=3 # deck
Ref_f=8 # TT fine

L=3.1 #[m] Length overall
L_ref=1.5 #[m] Length constant section
FS= 0.508 #[m] Free surface z position
v=0.478 #[m/s] reference velocity, highest ship velocity
visc=0.00104362/998.4 #[m/s^2] kinematic viscosity
y_plus=1.0 #[-] y+ value
L_tunnel=0.361#[m] Length tunnel
v_tunnel=3.0#[m/s] maximum expected velocity in the tunnel

zmirror=0.508#[m] height of the mirror plane

r=2 # [-]domain constant r
d=3 #[-] domain scaling factor, constant throughout the gridstudy

#Define Domain size
xmin=-d*L
xmax=4*d*L
ymin=-1.5*d*L
ymax=1.5*d*L
zmin=zmirror-2.0*d*L
zmax=zmirror

#Define triangularity settings
dom1=L/1000
dom2=L
dom3=0.001
dom4=1.0

xinitial=5*r*d#(xmax-xmin)/deltainitial #30
yinitial=3*r*d#(ymax-ymin)/deltainitial #18
zinitial=2*r*d#(zmax-zmin)/deltainitial #12

deltainitial=(xmax-xmin)/xinitial #Calculate intial cell size

#Free surface refinement target cell sizes
fs_x=deltainitial/2
fs_y=deltainitial/2
fs_z=L/1000/r

##Box refinements settings
#box1 ref_b
x_box1_min=1.4
x_box1_max=2.0
y_box1_min=-1.5
y_box1_max=1.5
z_box1_min=0
z_box1_max=0.377

#box 2 ref_d
x_box2_min=1.475
```

```
x_box2_max=1.625
y_box2_min=-0.05
y_box2_max=0.05
z_box2_min=0.077
z_box2_max=0.227

#box 3 ref_f
x_box3_min=1.475
x_box3_max=1.625
y_box3_min=-0.25
y_box3_max=-0.05
z_box3_min=0.077
z_box3_max=0.227

#box 4 ref_f
x_box4_min=1.475
x_box4_max=1.625
y_box4_min=0.05
y_box4_max=0.25
z_box4_min=0.077
z_box4_max=0.227

#box 5 ref_d
x_box5_min=1.475
x_box5_max=1.625
y_box5_min=-0.6
y_box5_max=-0.25
z_box5_min=0.077
z_box5_max=0.227

#box 6 ref_d
x_box6_min=1.475
x_box6_max=1.625
y_box6_min=0.25
y_box6_max=0.6
z_box6_min=0.077
z_box6_max=0.227

#Calculate y wall using the Numeca based Method
y_wall=6.0*((v/visc)**(-7.0/8.0))*((L/2.0)**(1.0/8.0))*y_plus
y_wall_tunnel=6.0*((v_tunnel/visc)**(-7.0/8.0))*((L_tunnel/2.0)
    **(1.0/8.0))*y_plus #for the tunnel


FM.create_project("caseh_mesh_a") #create a new project
FM.open_project("caseh_mesh_a/caseh_mesh_a.iec") #open this project
FM.switch_to_HEXPRESS() #open Hexpress
HXP.close_project()#close previousely opened projects in Hexpress
HXP.import_parasolid("barehull_wedge3_TT_circular_90.x_t") #Import a
    para-solid
HXP.create_cube("B2",Point(xmin,ymin,zmin),Point(xmax,ymax,zmax)) #
    Create a cube that will be used as domain
HXP.subtract_bodies("B2",["B1"]) #Subtract the wedge from the box
```

```
HXP.create_domain("caseh_mesh_a/_mesh/caseh_mesh_a.dom",["B2"],dom1,
    dom2,dom3,dom4,dom3,dom4) #Create a domain from the box using the
    settings for the triangulation
HXP.import_domain("caseh_mesh_a/_mesh/caseh_mesh_a.dom") #import the
    domain that was just created
HXP.set_mesh_generation_mode("3D")#Set the mesh generation mode to 3D
HXP.save_project("caseh_mesh_a/_mesh/caseh_mesh_a.igg") #Save the
    project


HXP.merge_face_list([0,1]) #Merge faces to get one tunnel
HXP.merge_face_list([5,6,7,8]) #Merge faces to get one hull

## Boundary condition definition and nameing of solids
# # # # # # # Tunnel thruster definitions
HXP.domain("caseh_mesh_a").get_face(16).set_name("TT_tunnel_b1")
HXP.domain("caseh_mesh_a").get_face(16).set_type("SOL",0)
HXP.domain("caseh_mesh_a").get_face(2).set_name("TT_side_b1")
HXP.domain("caseh_mesh_a").get_face(2).set_type("SOL",0)

# # # # # Hull and miship definitions
HXP.domain("caseh_mesh_a").get_face(3).set_name("midship_aft_b1")
HXP.domain("caseh_mesh_a").get_face(3).set_type("SOL",0)
HXP.domain("caseh_mesh_a").get_face(4).set_name("midship_front_b1")
HXP.domain("caseh_mesh_a").get_face(4).set_type("SOL",0)
HXP.domain("caseh_mesh_a").get_face(19).set_name("hull_b1")
HXP.domain("caseh_mesh_a").get_face(19).set_type("SOL",0)

# # # # # # Box definition
HXP.domain("caseh_mesh_a").get_face(14).set_name("Box_BB")
HXP.domain("caseh_mesh_a").get_face(14).set_type("EXT",0)
HXP.domain_face(14).enable_trimming(False)
HXP.domain("caseh_mesh_a").get_face(9).set_name("Box_Top")
HXP.domain("caseh_mesh_a").get_face(9).set_type("MIR",0)
HXP.domain_face(9).enable_trimming(False)
HXP.domain("caseh_mesh_a").get_face(10).set_name("Box_Front")
HXP.domain("caseh_mesh_a").get_face(10).set_type("EXT",0)
HXP.domain_face(10).enable_trimming(False)
HXP.domain("caseh_mesh_a").get_face(11).set_name("Box_STB")
HXP.domain("caseh_mesh_a").get_face(11).set_type("EXT",0)
HXP.domain_face(11).enable_trimming(False)
HXP.domain("caseh_mesh_a").get_face(13).set_name("Box_Bottom")
HXP.domain("caseh_mesh_a").get_face(13).set_type("EXT",0)
HXP.domain_face(13).enable_trimming(False)
HXP.domain("caseh_mesh_a").get_face(12).set_name("Box_Back")
HXP.domain("caseh_mesh_a").get_face(12).set_type("EXT",0)
HXP.domain_face(12).enable_trimming(False)

HXP.save_project() #Save project
HXP.init_cartesian_mesh(xinitial ,yinitial ,zinitial) #Set the settings
    for the intial mesh
HXP.generate_initial_mesh() #create the initial mesh
```

```
#### Mesh Adaption defintion
HXP.set_global_number_of_refinements(Ref_gen) #global refinement
    settings
#Grouping of different solids
HXP.domain("caseh_mesh_a").create_adaptation_group("TT",[16,2])
HXP.domain("caseh_mesh_a").create_adaptation_group("hull_top",[19])
HXP.domain("caseh_mesh_a").create_adaptation_group("hull_bottom",[3,4])
######Tunnel thruster refinements
HXP.domain_face(2).enable_adaptation(True)
HXP.domain_face(2).set_number_of_refinements(Ref_d)
HXP.domain_face(2).set_adaptation_criteria(0,0,1)
HXP.domain_face(16).enable_adaptation(True)
HXP.domain_face(16).set_number_of_refinements(Ref_d)
HXP.domain_face(16).set_adaptation_criteria(0,1,1)
### midship refinements
HXP.domain_face(3).enable_adaptation(True)
HXP.domain_face(3).set_number_of_refinements(Ref_b)
HXP.domain_face(3).set_adaptation_criteria(0,0,1)
HXP.domain_face(4).enable_adaptation(True)
HXP.domain_face(4).set_number_of_refinements(Ref_b)
HXP.domain_face(4).set_adaptation_criteria(0,0,1)
#### hull refinements
HXP.domain_face(19).enable_adaptation(True)
HXP.domain_face(19).set_number_of_refinements(Ref_a)
HXP.domain_face(19).set_adaptation_criteria(0,0,1)
### Refinement of edges (Hull-thruster intersections)
HXP.domain_edge(30).enable_adaptation(True)
HXP.domain_edge(30).set_number_of_refinements((Ref_f+1))
HXP.domain_edge(30).set_adaptation_criteria(0,1,1)
HXP.domain_edge(31).enable_adaptation(True)
HXP.domain_edge(31).set_number_of_refinements((Ref_f+1))
HXP.domain_edge(31).set_adaptation_criteria(0,1,1)
HXP.domain_edge(32).enable_adaptation(True)
HXP.domain_edge(32).set_number_of_refinements((Ref_f+1))
HXP.domain_edge(32).set_adaptation_criteria(0,1,1)
HXP.domain_edge(33).enable_adaptation(True)
HXP.domain_edge(33).set_number_of_refinements((Ref_f+1))
HXP.domain_edge(33).set_adaptation_criteria(0,1,1)

#RefinementBoxes
#Box1
HXP.create_refinement_cube(x_box1_min,y_box1_min,z_box1_min,x_box1_max,
    y_box1_max,z_box1_max)
HXP.refinement_box(0).set_target_size(0,0,0)
HXP.refinement_box(0).set_refinement_level(Ref_b)
#Box2
HXP.create_refinement_cube(x_box2_min,y_box2_min,z_box2_min,x_box2_max,
    y_box2_max,z_box2_max)
HXP.refinement_box(1).set_target_size(0,0,0)
HXP.refinement_box(1).set_refinement_level(Ref_d)
#Box3
HXP.create_refinement_cube(x_box3_min,y_box3_min,z_box3_min,x_box3_max,
    y_box3_max,z_box3_max)
HXP.refinement_box(2).set_target_size(0,0,0)
```

```
HXP.refinement_box(2).set_refinement_level(Ref_f)
#Box4
HXP.create_refinement_cube(x_box4_min,y_box4_min,z_box4_min,x_box4_max,
    y_box4_max,z_box4_max)
HXP.refinement_box(3).set_target_size(0,0,0)
HXP.refinement_box(3).set_refinement_level(Ref_f)
#Box5
HXP.create_refinement_cube(x_box5_min,y_box5_min,z_box5_min,x_box5_max,
    y_box5_max,z_box5_max)
HXP.refinement_box(4).set_target_size(0,0,0)
HXP.refinement_box(4).set_refinement_level(Ref_d)
#Box6
HXP.create_refinement_cube(x_box6_min,y_box6_min,z_box6_min,x_box6_max,
    y_box6_max,z_box6_max)
HXP.refinement_box(5).set_target_size(0,0,0)
HXP.refinement_box(5).set_refinement_level(Ref_d)

HXP.adapt_mesh() #Adapt the mesh to the refinements
HXP.snap_mesh() #Snap the mesh step

HXP.regularize_mesh() #Mesh reglularize
HXP.set_optimization_params(0,4,100,7,3,0,10) # Mesh optimization with
    the default parameters

#Enter viscouslayers in GUI
#All solids based y_wall
#TT_tunnel based on y_wall_tunnel

#Insert viscouslayers
HXP.save_project() #Save project
#End of mesh generation
```

C.2. Hopper wedge

In this section the used meshes for the Hopper wedge are shown. In Table C.2 all used meshes are defined, set-up refers to the approach of dealing with the free surface, $y+$ is the dimensionless first layer thickness that is used to calculate the viscous layer thickness and r is the scaling parameter of the mesh.

Table C.2: Overview of the used meshes for the Hopper wedge

					Number of initial cells			
Mesh name	Number of Cells	set-up	$y+$	r	$x_{initial}$	$y_{initial}$	$z_{initial}$	internal name
S1010A	3370292	4	1	2	30	18	18	S1010A_mesh_a
S0610A	3280307	4	1	2	30	18	18	S0610A_mesh_a
S0602A	3474569	4	1	2	30	18	18	S0602A_mesh_a

C.2.1. Python script for the Hopper wedge

In the following the script for S0602A mesh A is shown for the Hopper wedge. The script can be executed directly in Numeca FineMarine. For more details on the Python syntax of Numeca, please read the Hexpress Manual [19].

```
igg_script_version(2.1)

```

```
## Define refinement settings
Ref_gen=12 #general refinement settings
Ref_a=5 #top parts
Ref_b=6 # hull
Ref_c=3 # free surface
Ref_d=7 # 7 TT section
Ref_e=3 # top
Ref_f=8 # 8 TT fine

L=3.1 #[m] Length overall
L_ref=1.5 #[m] Length constant section
FS= 0.508 #[m] Free surface z position
v=0.478 #[m/s] reference velocity, highest ship velocity
visc=0.00104362/998.4 #[m/s^2] kinematic viscosity
y_plus=30.0 #[-] y+ value
L_tunnel=1.372#[m] Length tunnel
v_tunnel=3.0#[m/s] maximum expected velocity in the tunnel

zmirror=0.508#[m] height of the mirror plane

r=2# [-]domain constant r
d=3#[-] domain scaling factor, constant throughout the gridstudy

#Define Domain size
xmin=-d*L
xmax=4*d*L
ymin=-1.5*d*L
ymax=1.5*d*L
zmin=zmirror-2.0*d*L
zmax=zmirror

#Define triangularity settings
dom1=L/1000
dom2=L
dom3=0.001
dom4=1.0

xinitial=5*r*d#(xmax-xmin)/deltainitial #30
yinitial=3*r*d#(ymax-ymin)/deltainitial #18
zinitial=3*r*d#(zmax-zmin)/deltainitial #18

deltainitial=(xmax-xmin)/xinitial #Calculate intial cell size

#Free surface refinement target cell sizes
fs_x=deltainitial/2
fs_y=deltainitial/2
fs_z=L/1000/r

##Box refinements settings
#box1 ref_b
x_box1_min=1.4
x_box1_max=3.1
y_box1_min=-2.0
y_box1_max=2.0
```

```
z_box1_min=0
z_box1_max=0.3346

#box 2 ref_d
x_box2_min=1.475
x_box2_max=1.625
y_box2_min=-0.05
y_box2_max=0.05
z_box2_min=0.02
z_box2_max=0.2

#box 3 ref_f
x_box3_min=1.4
x_box3_max=2.0
y_box3_min=-0.8
y_box3_max=-0.05
z_box3_min=0.02
z_box3_max=0.2

#box 4 ref_f
x_box4_min=1.4
x_box4_max=2.0
y_box4_min=0.05
y_box4_max=0.8
z_box4_min=0.02
z_box4_max=0.2

#box 5 ref_d
x_box5_min=1.4
x_box5_max=2.0
y_box5_min=-1.4
y_box5_max=-0.8
z_box5_min=0.02
z_box5_max=0.2

#box 6 ref_d
x_box6_min=1.4
x_box6_max=2.0
y_box6_min=0.8
y_box6_max=1.4
z_box6_min=0.02
z_box6_max=0.2

#Calculate y wall using the Numeca based Method
y_wall=6.0*((v/visc)**(-7.0/8.0))*((L/2.0)**(1.0/8.0))*y_plus
y_wall_tunnel=6.0*((v_tunnel/visc)**(-7.0/8.0))*((L_tunnel/2.0)
    **(1.0/8.0))*y_plus #for the tunnel




FM.create_project("S0602A_mesh_a") #create a new project
FM.open_project("S0602A_mesh_a/S0602A_mesh_a.iec") #open this project
FM.switch_to_HEXPRESS() #open Hexpress
```

```
HXP.close_project() #close previousely opened projects in Hexpress
HXP.import_parasolid("S0602A.x_t") #Import a para-solid
HXP.unite_bodies("B1",["B2"])#Unite two bodies
HXP.unite_bodies("B1",["B3"])# Unite two bodies
HXP.create_cube("B4",Point(xmin,ymin,zmin),Point(xmax,ymax,zmax))# Create a cube that will be used as domain
HXP.subtract_bodies("B4",["B1"]) #Subtract the wedge from the box
HXP.create_domain("S0602A_mesh_a/_mesh/S0602A_mesh_a.dom",["B4"],dom1,dom2,dom3,dom4,dom3,dom4)#Create a domain from the box using the settings for the triangulation
HXP.import_domain("S0602A_mesh_a/_mesh/S0602A_mesh_a.dom")#import the domain that was just created
HXP.set_mesh_generation_mode("3D")#Set the mesh generation mode to 3D
HXP.save_project("S0602A_mesh_a/_mesh/S0602A_mesh_a.igg")#Save the project

HXP.split_face(12,0.0,1.4,0.0,0.0,2.0,0.0,0.0001) #split a face

HXP.merge_face_list([14,17,23,24,39,40,41,44,22,21,19,13,42,18,20,43])# Merge faces to get SB tunnel
HXP.merge_face_list([25,27,28,29,30,34,36,15,31,32,37,38,35,33,26,16])# Merge faces to get PS tunnel
HXP.merge_face_list([6,8,9,11])#Merge faces to get one hull

## Boundary condition definition and nameing of solids
# # # # # # # Tunnel thruster definitions
HXP.domain("S0602A_mesh_a").get_face(77).set_name("TT_tunnel_PS_b1")
HXP.domain("S0602A_mesh_a").get_face(77).set_type("SOL",0)
HXP.domain("S0602A_mesh_a").get_face(47).set_name("TT_side_PS_b1")
HXP.domain("S0602A_mesh_a").get_face(47).set_type("SOL",0)
HXP.domain("S0602A_mesh_a").get_face(62).set_name("TT_tunnel_SB_b1")
HXP.domain("S0602A_mesh_a").get_face(62).set_type("SOL",0)
HXP.domain("S0602A_mesh_a").get_face(46).set_name("TT_side_SB_b1")
HXP.domain("S0602A_mesh_a").get_face(46).set_type("SOL",0)

# # # # # Hull and miship definitions
HXP.domain("S0602A_mesh_a").get_face(10).set_name("midship_aft_b1")
HXP.domain("S0602A_mesh_a").get_face(10).set_type("SOL",0)
HXP.domain("S0602A_mesh_a").get_face(7).set_name("midship_front_b1")
HXP.domain("S0602A_mesh_a").get_face(7).set_type("SOL",0)
HXP.domain("S0602A_mesh_a").get_face(80).set_name("hull_b1")
HXP.domain("S0602A_mesh_a").get_face(80).set_type("SOL",0)

# # # # # # Box definition
HXP.domain("S0602A_mesh_a").get_face(0).set_name("Box_Front")
HXP.domain("S0602A_mesh_a").get_face(0).set_type("EXT",0)
HXP.domain_face(0).enable_trimming(False)
HXP.domain("S0602A_mesh_a").get_face(1).set_name("Box_SB")
HXP.domain("S0602A_mesh_a").get_face(1).set_type("EXT",0)
HXP.domain_face(1).enable_trimming(False)
HXP.domain("S0602A_mesh_a").get_face(2).set_name("Box_Back")
HXP.domain("S0602A_mesh_a").get_face(2).set_type("EXT",0)
HXP.domain_face(2).enable_trimming(False)
HXP.domain("S0602A_mesh_a").get_face(4).set_name("Box_PS")
```

```
HXP.domain("S0602A_mesh_a").get_face(4).set_type("EXT",0)
HXP.domain_face(4).enable_trimming(False)
HXP.domain("S0602A_mesh_a").get_face(3).set_name("Box_Bottom")
HXP.domain("S0602A_mesh_a").get_face(3).set_type("EXT",0)
HXP.domain_face(3).enable_trimming(False)
HXP.domain("S0602A_mesh_a").get_face(5).set_name("Box_Top")
HXP.domain("S0602A_mesh_a").get_face(5).set_type("MIR",0)
HXP.domain_face(5).enable_trimming(False)

HXP.save_project()#Save project
HXP.init_cartesian_mesh(xinitial ,yinitial ,zinitial)#Set the settings for the intial mesh
HXP.generate_initial_mesh()#create the initial mesh


#### Mesh Adaption defintion
HXP.set_global_number_of_refinements(Ref_gen)#global refinement settings
#Grouping of different solids
HXP.domain("S0602A_mesh_a").create_adaptation_group("TT",[77,47,62,46])
HXP.domain("S0602A_mesh_a").create_adaptation_group("hull_bottom",[7,10])
######Tunnel thruster refinements
HXP.domain_face(47).enable_adaptation(True)
HXP.domain_face(47).set_number_of_refinements(Ref_d)
HXP.domain_face(47).set_adaptation_criteria(0,0,1)
HXP.domain_face(77).enable_adaptation(True) #tunnel
HXP.domain_face(77).set_number_of_refinements(Ref_d)
HXP.domain_face(77).set_adaptation_criteria(0,1,1)
HXP.domain_face(46).enable_adaptation(True)
HXP.domain_face(46).set_number_of_refinements(Ref_d)
HXP.domain_face(46).set_adaptation_criteria(0,0,1)
HXP.domain_face(62).enable_adaptation(True)#tunnel
HXP.domain_face(62).set_number_of_refinements(Ref_d)
HXP.domain_face(62).set_adaptation_criteria(0,1,1)
### midship refinements
HXP.domain_face(7).enable_adaptation(True)
HXP.domain_face(7).set_number_of_refinements(Ref_b)
HXP.domain_face(7).set_adaptation_criteria(0,0,1)
HXP.domain_face(10).enable_adaptation(True)
HXP.domain_face(10).set_number_of_refinements(Ref_b)
HXP.domain_face(10).set_adaptation_criteria(0,0,1)
#### hull refinements
HXP.domain_face(80).enable_adaptation(True)
HXP.domain_face(80).set_number_of_refinements(Ref_a)
HXP.domain_face(80).set_adaptation_criteria(0,0,1)
### Refinement of edges (Hull-thruster intersections)
HXP.domain_edge(12).enable_adaptation(True)
HXP.domain_edge(12).set_number_of_refinements((Ref_f+1))
HXP.domain_edge(12).set_adaptation_criteria(0,1,1)
HXP.domain_edge(72).enable_adaptation(True)
HXP.domain_edge(72).set_number_of_refinements((Ref_f+1))
HXP.domain_edge(72).set_adaptation_criteria(0,1,1)
HXP.domain_edge(80).enable_adaptation(True)
```

```
HXP.domain_edge(80).set_number_of_refinements((Ref_f+1))
HXP.domain_edge(80).set_adaptation_criteria(0,1,1)
HXP.domain_edge(81).enable_adaptation(True)
HXP.domain_edge(81).set_number_of_refinements((Ref_f+1))
HXP.domain_edge(81).set_adaptation_criteria(0,1,1)
HXP.domain_edge(45).enable_adaptation(True)
HXP.domain_edge(45).set_number_of_refinements((Ref_f+1))
HXP.domain_edge(45).set_adaptation_criteria(0,1,1)
HXP.domain_edge(47).enable_adaptation(True)
HXP.domain_edge(47).set_number_of_refinements((Ref_f+1))
HXP.domain_edge(47).set_adaptation_criteria(0,1,1)
HXP.domain_edge(78).enable_adaptation(True)
HXP.domain_edge(78).set_number_of_refinements((Ref_f+1))
HXP.domain_edge(78).set_adaptation_criteria(0,1,1)
HXP.domain_edge(79).enable_adaptation(True)
HXP.domain_edge(79).set_number_of_refinements((Ref_f+1))
HXP.domain_edge(79).set_adaptation_criteria(0,1,1)

#RefinementBoxes
#Box1
HXP.create_refinement_cube(x_box1_min,y_box1_min,z_box1_min,x_box1_max,
    y_box1_max,z_box1_max)
HXP.refinement_box(0).set_target_size(0,0,0)
HXP.refinement_box(0).set_refinement_level(Ref_b)
#Box2
HXP.create_refinement_cube(x_box2_min,y_box2_min,z_box2_min,x_box2_max,
    y_box2_max,z_box2_max)
HXP.refinement_box(1).set_target_size(0,0,0)
HXP.refinement_box(1).set_refinement_level(Ref_d)
#Box3
HXP.create_refinement_cube(x_box3_min,y_box3_min,z_box3_min,x_box3_max,
    y_box3_max,z_box3_max)
HXP.refinement_box(2).set_target_size(0,0,0)
HXP.refinement_box(2).set_refinement_level(Ref_f)
#Box4
HXP.create_refinement_cube(x_box4_min,y_box4_min,z_box4_min,x_box4_max,
    y_box4_max,z_box4_max)
HXP.refinement_box(3).set_target_size(0,0,0)
HXP.refinement_box(3).set_refinement_level(Ref_f)
#Box5
HXP.create_refinement_cube(x_box5_min,y_box5_min,z_box5_min,x_box5_max,
    y_box5_max,z_box5_max)
HXP.refinement_box(4).set_target_size(0,0,0)
HXP.refinement_box(4).set_refinement_level(Ref_d)
#Box6
HXP.create_refinement_cube(x_box6_min,y_box6_min,z_box6_min,x_box6_max,
    y_box6_max,z_box6_max)
HXP.refinement_box(5).set_target_size(0,0,0)
HXP.refinement_box(5).set_refinement_level(Ref_d)

HXP.adapt_mesh()#Adapt the mesh to the refinements
HXP.snap_mesh() #Snap the mesh step

HXP.regularize_mesh() #Mesh reglularize
```

```
HXP.set_optimization_params(0,4,100,7,3,0,10)  # Mesh optimization with
    the default parameters

#Enter viscouslayers in GUI
#All solids based y_wall
#TT_tunnel based on y_wall_tunnel

#Insert viscouslayers
HXP.save_project() #Save project
#End of mesh generation
```

D

Error propagation

In order to evaluate an error of a quantity, that is a function of multiple variables, methods of error propagation need to be used. A basic paper deriving methods to analyze error propagation was published by Ku in 1966. In the following only the main equation is presented and the equation to calculate basic algebraic operations is shown, for more information please read [32].

The error of a function f which is dependent on the variables $x_1, x_2, ..., x_n$ can be calculated as [32, Eq. 2.10]:

$$\Delta f = \sqrt{\left[\frac{\partial f}{\partial x_1}\right]^2 \Delta x_1^2 + \left[\frac{\partial f}{\partial x_2}\right]^2 \Delta x_2^2 + ... + \left[\frac{\partial f}{\partial x_n}\right]^2 \Delta x_n^2} \tag{D.1}$$

This equation assumes that the random errors of the variables Δx_n are independent and that the function f is differentiable. In the following the solution of Equation D.1 for basic algebraic operations: addition, subtraction, multiplication and division is given. In the derivation it is assumed that the variables a and b are independent and the corresponding errors Δa and Δb as well. In Table D.1 all necessary information is provided.

Table D.1: Basic algebra operators and there corresponding error propagation

Operation	Function	Partial derivatives	Error definition (Eq. D.1)
Addition	$f = a + b$	$\frac{\partial f}{\partial a} = 1, \quad \frac{\partial f}{\partial b} = 1$	$\Delta f = \sqrt{\Delta a^2 + \Delta b^2}$
Subtraction	$f = a - b$	$\frac{\partial f}{\partial a} = 1, \quad \frac{\partial f}{\partial b} = -1$	$\Delta f = \sqrt{\Delta a^2 + \Delta b^2}$
Multiplication	$f = a \cdot b$	$\frac{\partial f}{\partial a} = b, \quad \frac{\partial f}{\partial b} = a$	$\Delta f = \sqrt{(b\Delta a)^2 + (a\Delta b)^2}$
Division	$f = \frac{a}{b}$	$\frac{\partial f}{\partial a} = \frac{1}{b}, \quad \frac{\partial f}{\partial b} = -\frac{a}{b^2}$	$\Delta f = \frac{a}{b}\sqrt{\left(\frac{\Delta a}{a}\right)^2 + \left(\frac{\Delta b}{b}\right)^2}$

List of Figures

List of Tables

Bibliography

[1] U. Nienhuis, *Analysis of thruster effectivity for dynamic positioning and low speed manoeuvring*, Ph.D. thesis, TU Delft, Delft University of Technology (1992).

[2] Maritime Journal, *Boskalis and Van Oord create sand engine to reinforce Dutch coastline,* Website: maritimejournal.com (2011).

[3] T. Schaap, *Changing the cross-sectional geometry of a bow tunnel thruster - Effects on the performance of the thruster at slow forward motion using Computational Fluid Dynamics*, Master Thesis Definition study, Delft University of Technology, Faculty of Mechanical, Maritime and Materials Engineering (2015).

[4] V. Karlikov and G. Sholomovich, *Some features of body-flow interaction in the presence of transverse jets,* Fluid dynamics **33**, 313 (1998).

[5] J. H. Ferziger and M. Perić, *Computational Method for Fluid Dynamics* (3rd Edition, Springer Verlag Berlin Heidelberg New York, ISBN: 3-540-42074-6, 2002).

[6] H. K. Versteeg and W. Malalasekera, *An Introduction to Computational Fluid Dynamics, The Finite Volume Method* (2nd Edition, Pearson Education Limited, ISBN: 978-0-13-127498-3, 2007).

[7] F. Lafeber, *CJK01 dredger (122 M); bow thruster performance computations,* MARIN Report, Confidential report made for IHC **25868-1-POW** (2014).

[8] S. Wolfram, *Some historical notes on the Navier-Stokes Equations, A new kind of science* (Wolfram Media, p.998 ISBN: 978-1-579-55008-0, 2002).

[9] A. Mir, *Introduction to Computational Fluid Dynamics,* Numeca FineMarine 3.1 Training notes (2015).

[10] Equipe Dynamique des Systèmes Propulsifs Marins, *Theoretical Manual ISIS-CFD v3.1* (Laboratoire de recherche en Hydrodynamqie, Ecole Centrale de Nantes, France., 2014).

[11] S. Collie, M. Gerritsen, and P. Jackson, *A Review of Turbulence Modelling for use in Sail Flow Analysis,* University of Auckland, School of Engineering Report No. 603 (2001).

[12] P. J. Roache, *Verification and validation in computational science and engineering* (Hermosa publishers, Albuquerque, New Mexico, ISBN: 0-913478-08-03, 1998).

[13] The American Society of Mechanical Engineers, *Standard for Verification and Validation in Computational FLuid Dynamics and Heat Transfer* (The American Society of Mechanical Engineers, New York, ASME V&V 20-2009, 2009).

[14] D. Rijpkema and G. Vaz, *Viscous Flow Computations On Propulsors: Verification, Validation And Scale Effects,* RINA Developments in Marine CFD (2011).

[15] Numeca, *User Manual, FineMarine 3.1, Flow Integrated Environment for Marine Hydrodynamics,* Numeca FineMarine 3.1 Documentation (2014).

[16] L. Eça and M. Hoekstra, *Verification and validation for marine applications of CFD,* International Shipbuilding Progress **60** (2013).

[17] L. Eça and M. Hoekstra, *A procedure for the estimation of the numerical uncertainty of CFD calculations based on grid refinement studies* , Journal of Computational Physics **262**, 104 (2014).

[18] A. Rohatgi, *WebPlotDigitizer Version 3.8,* (2015).

[19] Numeca, *User Manual, HEXPRESS v3.1, Unstructured Grid Generator,* Numeca Hexpress Documentation v.3.1c (2014).

[20] Numeca, *How to simulate submerged bodies with imposed motions?* Numeca FineMarine 3.1 Documentation (2014).

[21] S. I. Baniela, *The Performance of a Tunnel Bow Thruster with Slow Speed Ahead: A Revisited Issue,* Journal of Navigation **62**, 631 (2009).

[22] J. L. Beveridge, *Design and performance of bow thrusters*, Tech. Rep. (DTIC Document, 1971).

[23] M. S. Chislett and O. Björheden, *Influence of ship speed on the effectiveness of a lateral-thrust unit* (Hydro-and Aerodynamics Laboratory, Hydrodynamic Section No. 8, 1966).

[24] R. Verbeek, *De netto stuwkracht van thrusters (in Dutch),* Lips technical report **5330-8201** (1982).

[25] J. Grevink, *Transverse thrusters,* Delft University of Technology, lecture note OE5663- DP systems by Wärtsilä (2015).

[26] J. W. Slater, *Supersonic Wedge Flow: Study 2,* NASA Glenn Research Centre (2008).

[27] W. B. Coney, *A method for the design of a class of optimum marine propulsors*, Ph.D. thesis, Massachusetts Institute of Technology (1989).

[28] S. Gopalan, B. M. Abraham, and J. Katz, *The structure of a jet in cross flow at low velocity ratios,* Physics of Fluid, American Institue of Physics, doi: 10.1063/1.1697397 **16**, 2067 (2004).

[29] M. L. Albertson, Y. Dai, R. Jensen, and H. Rouse, *Diffusion of submerged jets,* Transactions of the American Society of Civil Engineers **115**, 639 (1950).

[30] MAN, *Basic Principles of Ship Propulsion* (MAN Diesel & Turbo, Denmark, 2011).

[31] E. W. Weisstein, *Secant Method. From MathWorld- A Wolfram Web Resource,* (2015).

[32] H. H. Ku, *Notes on the use of propagation of error formulas,* Journal of Research of the National Bureau of Standards **70** (1966).